UC Davis
UC Davis Electronic Theses and Dissertations

Title

Numerical Model of Cilia-Driven Transport of Inhaled Particles in the Periciliary Layer of the Human Tracheobronchial Tree

Permalink

https://escholarship.org/uc/item/9d63v7h6

Author

Ruvalcaba, Carlos Abraham

Publication Date

2021

Peer reviewed|Thesis/dissertation

eScholarship.org Powered by the California Digital Library
University of California

Numerical Model of Cilia-Driven Transport of Inhaled Particles in the Periciliary Layer of the Human Tracheobronchial Tree

By

CARLOS ABRAHAM RUVALCABA
DISSERTATION

Submitted in partial satisfaction of the requirements for the degree of

DOCTOR OF PHILOSOPHY

in

Mechanical and Aeronautical Engineering

in the

OFFICE OF GRADUATE STUDIES

of the

UNIVERSITY OF CALIFORNIA

DAVIS

Approved:

Jean-Pierre Delplanque, Chair

Jerold Last

Anthony Wexler

Committee in Charge

2022

© Carlos A. Ruvalcaba, 2021. All rights reserved.

Dedicado a mi familia, cuyos sacrificios fueron mayores que los míos
Dedicated to my family, whose sacrifices were greater than mine

Contents

Numerical Model of Cilia-Driven Transport of Inhaled Particles in the Periciliary Layer of the Human Tracheobronchial Tree

Abstract

The human respiratory system has evolved to maintain critical functions for survival despite being vulnerable to threats in the environment that are inhaled as part of the necessary gas exchange process. In the respiratory tract, ciliated cells line the tracheal-bronchial tree where mucus producing cells create a barrier that captures inhaled particles. The ciliated cells have hair like protrusions that beat in complex beat patterns in order to move the mucus towards the throat where it is expectorated or swallowed. The system complexity has made it difficult to properly measure particle clearance *in-vivo*. The subject of this dissertation is to numerically study the interaction of inhaled particles with the ciliated cell population. More specifically, the numerical modeling effort builds on work analyzing mucosal layer clearance by addition of arbitrary shaped finite-sized particles in the mucosal layer. In our work, we show that finite-sized particles compared to massless tracers have non-trivial clearance paths, challenging and enriching previous modeling assumptions that massless tracer particles are sufficient for measuring clearance.

We consider one specific simplified model, a single cilium infinitely repeating, and a more representative model, a cilium patch, to understand the effect that biophysical airway parameters have on particle-cilia interaction. We consider the effects that the configuration parameters have on clearance and, in addition, how the dynamics of a finite-sized particle differ from massless tracers. Second, we broaden our model to consider a patch of cilia that represent a two-dimensional cross section of the upper airway. The effect of multiple cilia structures are studied by varying arrangement and synchrony. Next, we quantify in detail the effect that these parameters have on the transport of any arbitrary shaped particles. This dissertation is concluded with a thorough analysis of the flow dynamics in the periciliary layer by incorporating three distinct measures of mixing.

Acknowledgements

The journey towards this Ph.D. and its completion is one that begins with the care and love of two wonderful human beings, Zenaida and Aurelio Ruvalcaba, my parents. Without their constant support and guidance throughout my life, I would not be who I am today. Without their endless dedication to the growth and maturity of my sister and myself, this work would not have been completed. I am indebted to their teachings, both in and out of the academy, which is all but a part of the generations of lessons received by my ancestors and their ancestors. I looked to my elder sister for the guiding light at every step of the educational ladder. She took the obligatory role of being my elder sister, thus first peer-role model, and proved to be the very best one to have. From guiding me to take (and re-take) the SAT, to paying for my college applications, to taking me on college tours, all the while attending college (and being the first person in our family to do so). She provided the foundation to move towards an education, in the most stylish of ways. To my family, **I thank you**.

The day to day and week to week supervision of this work would not have been possible without the tireless mentorship from Prof. Jean-Pierre Delplanque. His careful guidance and encouraging leadership has made my graduate school experience a most memorable and educational one. Key moments in our discussions driving to visit collaborators at Lawrence Livermore National Laboratory were unlike any I have witnessed. Every single endeavor that I attempted to participate in, his support was there, both encouraging and grounded in realism. His inordinate confidence in all his students is so clearly displayed in actions that are beyond what I ever expected from a supervisor. The lab group that he has assembled through the sheer gravity of his kindness is one that I will forever be in awe and aim to replicate.

The Delplanque Research Group members, you formed the environment for an equitable and open research group. The careful feedback during group meetings and interactions outside of the laboratory made this environment free of competition and envy, much of which plague the academy. I could not have asked for more friendly and brilliant members to share in the graduate school journey. Specifically, Dr. Alex J. Wolfer, has been an academic-brother, turned lifelong friend, to share ideas about research and the world. I look forward to the discussions in life and much more in the days to come. In the days where motivation *ran* dry, Dr. Monica Keiko Lieng gave her friendship and medical expertise not only to keep me going, both in the lab and on the running trails, but provided a much needed space to lean on and hold me accountable. The intense academic discussions with Dr. Brian Weston are unparalleled in curiosity and precision. His attention to novel research has always been a guiding light for me. He identified the great mentorship from Prof. Delplanque and he is the reason I joined the group. Dr. Rebecca Barney's optimism and dedication were a much needed bright light when otherwise seemingly unsolvable problems persisted. Dr. Christopher Nilson's and Dr. Dane Sterbentz's weekly calm demeanor challenged me to overcome many fears and tackle the next problem, whether that be computational or experimental in nature. I have one piece of advice for the students that have yet to graduate from the Delplanque Research Group: you are in good hands. You have already provided me, in a short time, with great questions and proper feedback. Trust in each other, and you will achieve your goals.

I had the privilege of interacting with the many collaborators of Prof. Delplanque's group, specifically, Dr. Jerold Last, Dr. Nicholas Kenyon, Dr. Angela Linderholm, Lisa Franzi, Dr. Jennifer Bratt, and Dr. Lisa Tell. I thank each and everyone of you for the constant encouragement and trust. The experimental escapades that I was able to participate in from working with live tissue cultures to live animals have been some of the most rewarding thus far. It is a rare opportunity that befalls some members of the Delplanque Research Group, and it has been one of the most fruitful experiences for me personally. The collaborators from Lawrence Livermore National Lab, Dr. Rose McAllen and Dr. Willy Moss, allowed me the opportunity to expand my research horizons by sampling the intensity of the research possibilities in their areas. I thank you for the support and willingness to work on mutual interests during the summer of 2019. I would also like to thank Prof. Becca Thomases and Prof. Robert Guy for recently incorporating me into their weekly group meetings, which have proven to be some of the most collaborative and welcoming experiences in my tenure as a student. I have been able to learn a great deal from you both in such a short time.

I would be remiss if I were to not mention the many undergraduate students that I have watched grow into successful and independent scientists. I cannot name all of the students in this short acknowledgement section, but I will thank those that I have personally mentored in research projects. Roger Monroy, Stephanie Ortega, Susana Ramirez-Perez, and Alexandro Lopez all carried forward experimental work that I otherwise could not accomplish. Léa Lurois, Brooke Raabe, Jamiree Harrison, Alexia Portillo Rivera, and Lay Heng Teng chose to indulge in numerical simulations, decoding my often cryptic instructions on using `sbatch` and `bash` commands. Each interaction with every one of you all helped teach me about my own field, and the responsibility of educating the next generation of scientists. The more we delved into complex research questions, the more I learned about myself and my own assumptions on what we all knew. I thank you all for your hard work, dedication to the research, and patience in me.

Along my journey I spent time learning about the academy and the improvements that would benefit tomorrow's graduate students and faculty. Through the mentorship of Dr. Steve P. Lee, I learned of the challenges we face in retaining students such as myself in the so-called "Ivory tower". I thank Dr. Lee for solidifying the drive to complete my degree, for treating me with kindness, and building my strengths in the times that I needed that the most. I was able to share my knowledge with the UC LEADS program, under the mentorship of Lynne Arcangel Bowyer, where I interacted with countless students seeking to accomplish what I was in the process of completing. Mrs. Arcangel Bowyer's unmatched development of young minds gave me the opportunity to teach these students, whose experiences matched my own. I invested heavily in their success, and I thank each person in the program who believed in my own abilities and trusted me with their education. To all the graduate students with whom I had the privilege to work with during my tenure as Graduate Student Association Vice Chair and Chair, our work many times goes unnoticed (e.g. the dreadful process of making the graduate S.P.A. a reality), but know that I noticed and often found myself learning more than contributing to the discussions. You were truly an interdisciplinary group and worked tirelessly beyond your daily research responsibilities. Specifically, Dr. Sarah Messbaur and Dr. Gwen Chodur believed in me, and defended me in situations where words escaped me; I wish you the very best in your amazing futures.

Last, but not least, I must thank the peers that helped me along the way, teaching me to discover new horizons outside of the daily research challenges that we slowly march towards understanding. An integral part of completing this work must be attributed to the love and care from my partner, Jayvani Thakur Garcia. Without her constant encouragement and unwavering commitment, I would not have been able to continue this work. For my friends from the Institute, Dimitri Porcelli, Gonzalo Guajardo, Dr. Michelle Dang, Phillip Mercer, Kim Kaster, Orlando Saldivar, Jarell Spears, and Dr. Rosemary de la Rosa, know that you contributed in countless hours of this dissertation. Specifically, Mr. Porcelli and Mr. Guajardo provided *support* that would not be found elsewhere. For my friends from Davis and the UC community, Dr. Anna M. Naranjo, David Maginnis, Dr. Javier Alexandro Garcia, and Juan Castillo, thank you for the small town memories and for being the support I needed outside of the research environment. Finally, thank you to the midnight lamplight library study group, Dr. Syed Jaan Naqvi, Dr. Carlos Rojas, and Dr. Ernesto Manzo, for showing that the four of us from Ganesha High School in Pomona did indeed make it.

Davis, California, December 2021

Chapter 1

Introduction

1.1 Respiratory Inhalation and Dysfunction

The average human takes 12-20 breaths per minutes while at rest, inhaling the surrounding air that contains the atmospheric oxygen needed for normal human function [1]. At these basal conditions, we exchange about 0.5 liters of air per breath. The respiratory system, central to our daily gas-exchange process, has an important role in assuring that the inhaled air is warmed to body temperature, humidified to prevent alveolar desiccation, and cleared of foreign airborne particulates. The physiological function of particle clearance is the primary focus of this dissertation, and specifically we are interested in studying changes that can come about from diseases or acute exposure to harmful airborne substances in the air.

Deposition of foreign airborne particulate matter in the human lung begins with some particle or aerosol suspended in the surrounding air, followed by a dangerous journey (for the particle). If the human breathes through the nose, the particle must make its way through our first line of defense, the nasal cavity, and avoid both the curvature of the nasal passages and hairs that begin the filtering. As it passes through the upper respiratory tract, it must make a steep turn towards the trachea at the nasopharynx. The upper respiratory tract has accomplished partial filtering of mostly large particles, leaving particles of sizes approximately less that 10 μm in diameter. The successful particles now travel through the tracheobronchial tree, beginning at the trachea and continuing through $\sim$16 bifurcating generations. Most particles end up depositing at the conducting airway bifurcations through inertial impaction, and as the airflow comes to almost a halt, much smaller particles now remain suspended in the inspired, and now acclimated, air. This long path ends when the inspired air reaches such small velocities that the suspended particles now diffuse towards the alveoli and the immune system begins the process to rid our bodies of the intruders. Not all particles diffuse towards the alveoli, or deposit in our airways, but are respired out ($\sim 80\%$ [2]), in the following breath, starting the process over once again.

These intruders, and our inherent inhalation of them, are of exceptional interest to researchers in human health. The classification of these intruders is quite complex, but broadly speaking, one definition from the U.S. Environmental Protection Agency [3] categorizes particles based on their aerodynamic diameter ranges: *coarse particulate matter* (PM_{10}) sizes between 2.5-10 μm and *fine particulate matter* ($PM_{2.5}$) sizes less than 2.5 μm. Additionally, there is new evidence to suggest another classification, *ultra-fine particulate matter* ($PM_{0.1}$), for particles with sizes less than 0.1 μm, which have been shown to also be inhaled at elevated rates [4]. Sources of these particulates range from natural processes in the atmosphere to more human-linked sources. The largest estimated human source is from urban activities that pollute the air from traffic, accounting for around 25% of particulate matter [5]. Conversely, natural processes only account for 18% of particulate matter, implying that between traffic and natural process, the rest of particulate matter is human-made. Consequently, the inhalation of these harmful particulates leads to detrimental health conditions [6]. Health conditions directly linked to particulate matter include increased exacerbation of pulmonary diseases (including asthma, chronic obstructive pulmonary disease (COPD), acute respiratory distress syndrome (ARDS), and others), cancer, and cardiovascular disease. Additionally, children living in areas that have higher concentration of particulate matter in the ambient air are reported to have a higher risk of respiratory disease.

Under normal conditions, the tracheal, bronchial and lung epithelia layers act as mechanical barriers against inhaled toxic compounds and pathogens entering the lung. The World Health Organization (WHO), the American Lung Association (ALA), and the European

Union Statistical Office (Eurostat) all report incidence of respiratory disease. During the Forum of International Respiratory Societies in 2013, chronic obstructive pulmonary disease (COPD) was reported as the 4th leading cause of death worldwide [7]. The ALA reports an estimated prevalence of 2.3 million adults with asthma and 1.2 million cases of COPD in California alone [8]. These reports of high rates of disease, coupled with the ever increasing pollutants from human made sources, necessitates the need for understanding the human respiratory system. In this work, we aim to achieve a better understanding of the human tracheo-bronchial tree at the mucosal layer scale.

1.2 The Mucociliary Escalator

Different flow regimes and their effect on the fate of inhaled particles have been thoroughly studied. Such studies include experimental and simulated inhalation of dispersed particles in the upper respiratory tract [9–11] and surrounding nasal cavity [12] as well as particle transport in the lower respiratory regions [13]. It is generally agreed in the literature that particle retention in the lung, and ultimately toxicity, depends on different time scales: faster cilia clearance for particles that are deposited ($\sim$40+ μm/s mucosal layer velocity), and slower particle clearance by macrophages (mass and van de Waals force-driven particle retention over $\sim$24 hrs.). This research is concerned with the study of the lower respiratory tract at the mucosal layer and the effect its properties as well as key particle parameters have on the mucociliary clearance rate. The sticky mucus layer above the epithelium traps inhaled particles, pathogens, and toxins, transporting them quickly through the upper airways by means of ciliary beating. Each ciliated epithelial cell carries approximately 200 cilia (7–10 μm in length), which move the extracellular mucus by constant synchronous beating. A review of a considerable amount of literature on the structure and functional physiology of the mucociliary escalator is summarized in Table 1.1.

The mucociliary layer complexity makes creating accurate models difficult, which are

cilia	parameter	reported range	References
length	h_c	$7 - 13\ \mu$m	[14, 15]
diameter	d_c	$0.1 - 0.3\ \mu$m	[14, 15]
spacing	l_c	$0.25 - 2.0\ \mu$m	[16, 17]
per cell	n_c	$150 - 300$	[16]
beat frequency	f	$10 - 20$ hz	[14, 18–21]
mucosal layer			
height	h_{ml}	$10 - 250\ \mu$m	[15, 17, 22]
periciliary viscosity	μ_p	1.0×10^{-3} Pa/s	[18, 23]
periciliary height	h_p	$7 - 40\ \mu$m	[18, 23]
periciliary density	ρ_p	1 g/cm^3	[18, 23]
clearance velocity	V_{ml}	$40 - 250\ \mu$m/s	[21, 24]

Table 1.1: Reported values that are useful to consider for the problem definition. Literature cited is not comprehensive, but illustrative of ranges in human upper airways [14–24].

increasingly challenging when considering the range of physiological changes due to diseases. In the case of COPD, mucus production is elevated when compared to healthy individuals, which has been shown to also have increased viscosity [25]. This hypersecretory phenotype has been associated with inhalation of airborne particles, which damages cilia and decreases transport. When considering the autosomal recessive disease cystic fibrosis, genetic disruption of the regulation of cell membrane ion flow, leads to dysfunction across several organs, however, the lung suffers from abnormal mucus production leading to increased bacterial infections and airway dilation [26]. The effects from breakdown of mucus clearance, coupled with the disease prevalence reported by the ALA, WHO, and Eurostat, may lead to increased mortality from the reduced performance of the mucociliary escalator. We cite only a few examples here of diseases that effect the mucosal layer and subsequent clearance of foreign particles to illustrate additionally motivation for modeling mucosal layer clearance.

1.3 Modeling Mucosal Clearance

Specific to the mucociliary escalator, experimental measurements of mucus production as a function of diseased state, oscillating stretch conditions, and flow-mediated stress have been conducted [2, 27]. These studies have used human respiratory tract epithelial cells from the nasal, bronchial, and alveolar regions. Computational fluid dynamics (CFD) models that have robust capability to capture more physical flow phenomena have also paralleled these studies. Using a combination of whole lung particle deposition models, mucosal layer 2-dimensional models, and mass transfer models the fate of inhaled toxins has begun to be clarified. These models have been particularly complicated individually, and only recently have the full-scale lung model and mass transfer model been incorporated. Previous studies focusing on experimentally modeling particle clearance have used excised rat trachea sections [28]. The trachea is then exposed to various types of particles that have different size, morphology, and chemical compositions. The experimental results are then compared to the computational results of a Newtonian fluid in 2-dimensional. The computational results point to little to no particle sedimentation and therefore imply that different sized, density, and shape particles are all cleared by the mucociliary escalator. However, experimental studies have shown that diseased pulmonary epithelial cells change the structure of the mucosal layer and clearance and highly depend on exposure duration. This contradicting evidence showing that particle deposition and subsequent clearance is sensitive to modeling parameters requires further research in order to extrapolate to human subjects in normal and diseased lung conditions.

Mathematical and computational models have been used for predicting deposition characteristics in several areas of the human respiratory tract. Different flow regimes have been studied such as inhalation of dispersed particles in the surrounding 3-dimensional nasal cavity [12] to 2-dimensional studies of fluid transport in mucus [29]. This effort toward a full lung computational model is necessary but is prohibitively expensive with the current computational technology. Therefore, modeling in this field has required researchers to develop multiple levels of complexity for different areas in the respiratory tract along with relevant experimental validation studies. In the following sections, we will discuss the early modeling techniques used by researchers to study the mucosal layer and its function. For a recent and complete review of many of the modeling techniques see [30].

1.3.1 Analytic and Semi-Numerical Methods

Before the advent of modest computational technology, modeling techniques relied on simplifying the governing equations into analytic models. In the literature, models are split into two distinct categories: envelope models or discrete sub-layer models. Envelope models generally treat a time-dependent boundary condition as the primary source of fluid movement in the mucosal layer. This results in usually creating a wave-like boundary condition that travels across the fluid interface. Some of the seminal works in envelope models include work in [31–33]. Discrete sublayer models on the other hand treat individual cilia as the drivers of fluid flow. Many of these models used realistic measurements of excised animal tracheae in order to represent the physiology. The focus of this research builds upon some of the cilia characteristics used in these seminal works by Sleigh et al. [14], Sanderson and Sleigh [21], Fulford and Blake [34].

In the literature, two models are typically used for studying mucus, and the effect rheology has on mucosal clearance rate. The first type uses different viscosities for the periciliary and mucus layers, and the second uses a non-Newtonian mucus layer that is treated as Maxwell or visco-elastic fluid with a Newtonian periciliary layer [35]. The ciliary effect on fluid dynamics of the mucosal layer is studied by either a volume force approach or discrete cilia that impact a force on the fluid. The limitation of these studies on understanding true particle clearance is that two-way coupling between particles and mucus is not often studied. For particle sizes that are comparable to the cilium length ($\sim 10\ \mu$m), these models cannot capture the dynamics that evolves between particles and cilia. As a simplification, 1-dimensional models are then used to track mass conservation of mucus along the tracheobronchial paths with bulk particle concentration equations [36], which show reasonable agreement with experimental measurements.

1.3.2 Numerical Modeling

Numerical models of mucosal clearance have advanced tremendously since the constraints posed by early computational capability. With this increase, however, more physics has been added to the modeling effort. The particle deposition patterns in the lung treat the structure as symmetric, non-compliant, and incorporate multiple airway generations. Nonetheless, the transitional nature of the flow regime makes it extremely difficult to accurately model deposition patterns without properly calibrating models to incorporate realistic inhalation particle distributions from experiments [37–39]. Further, systemic toxicity and particle mass transport into the blood stream have been incorporated into a multicompartmental model [40]. A multicompartmental model requires developing mass transport paths to different compartments (tissues, organ systems, etc.) and developing the mass concentration rates between these compartments. Empirical studies are then used to calibrate and determine the viability of these models. It is understood that some of these models are incorrectly applied to systemic toxicity in humans, which is partly due to the limited availability of human experimental data for calibration and simplicity of the model. Nonetheless, these approaches to predicting particle deposition and clearance in the lung macro to micro environment are necessary first steps. Thus, it is clearly necessary to investigate the interface between a complete lung model and a multicompartmental model: the mucosal layer between air and cell.

Mucosal layer modeling now includes non-Newtonian fluid effects including single and multiple cilia structures [41–43], mucus maturation effects from mixing caused by cilia beating [44–52], cilia power expenditures in healthy and diseased states [53], and cilia kinematics in response to hydrodynamic coupling [54–56]. Most of the experimental validation used by researchers that model the mucosal clearance process require several of the imaging techniques with particle tracing being used as a prominent feature. Further, whole body exposure of particulates as a validation for inhaled particle deposition models would require careful imaging of *in-vivo* subjects. This impressive multidisciplinary effort by countless researchers continues to expand. However, there are still gaps in the knowledge that require continued collaboration.

1.4 Low Reynolds Number Flows

The class of problems of interest in biological fluid dynamics are at very small length scales, as is our case of mucociliary transport. The Reynolds number is helpful in determining the relative importance of inertia in such flows, and it is defined as

$$Re = \frac{VL}{\nu} \tag{1.1}$$

where V and L is are a characteristic velocity and length, respectively, of the system considered with fluid density and viscosity, ρ and μ respectively. For this dissertation, the problem of interest has a length scale in the order of tens of micrometers (10 μm), and a velocity scale in the order of tens to hundreds of micrometers ($10 - 100$ μm/s). For simple biological fluids, the fluid kinematic viscosity could be approximated to that of water, $\mu/\rho \sim 10^{-6}$ m/s leading to Reynolds number on the order of $10^{-4} - 10^{-3}$, which indicates that inertial forces are small and negligible. Additionally, in the context of broader biological flows, micro-organism swimming [57–61] and more recently, microfluidic devices [62, 62–64], also operate at this zero-inertial limit. This fundamental constraint of no inertia poses challenges for processes that occur at these low Reynolds numbers, requiring organisms to evolve asymmetric movement (e.g. cilia beating shapes) in order to move through or propel the fluid where they habituate.

Both the analytic and some full-numerical modeling efforts described above in Section 1.3.1 use this fact to simplify the governing equations by taking the limit $Re \to 0$ in order to make use of the quasi-steady Stokes Equation,

$$\vec{\nabla} p = \vec{\nabla}^2 \vec{v} \tag{1.2}$$

where p and $\vec{v}$ are pressure and velocity respectively (note, Equation 1.2 is the non-dimensional Stokes Equation, where the reference length, velocity, and pressure are L, V, and $\mu V/L$ respectively). For certain micro-flows, this assumption is a valid one, although there exists experimental evidence that inertial effects in confined-channel microfluidic devices play a role in transport [65]. For particle transport in mucociliary clearance, 2-dimensional solutions for Stokes Equation of finite-sized particles at low Reynolds number do not have unique solutions in the Stokes limit due to Stokes Paradox, for which inertia is required to resolve the paradox [66]. Nonetheless, the inclusion of inertia is applicable to a cylinder with length much greater than the cross-sectional diameter. The importance of inertia in the far field for 2-dimensional flows is of particular importance in the work presented in this dissertation, and results presented must be evaluated in this context.

1.5 Research Goals and Dissertation Structure

Specific to this research, computational lung simulations could help understand, diagnose and treat pulmonary diseases such as asthma, COPD, and ARDS. While computation-supported medicine has seen some success in other areas, e.g. the planning of infant cardiovascular surgery with help from computational fluid flow modelers has been successfully shown [67], this capability has not been fully extended to the respiratory system. Of course, building a full lung numerical simulator is a very ambitious goal and achieving it will require the consideration of more focused, smaller subunit problems: from cellular chemical reactions, to the mucociliary system, to turbulent upper airway flow. Additional impetus for addressing such local problems exists. For example, the development of a numerical model of the mucociliary system would provide much needed insight regarding the mechanisms that control the mucociliary escalator and its role in inhaled particle clearance, a critical problem in respiratory medicine.

This dissertation is concerned with understanding how finite-sized particulates interact with the mucociliary system in the respiratory system. The mucociliary escalator is an extremely challenging problem to study, and making experimental measurements *in-vivo* is not possible with current technology. In the context of more fundamental fluid flow phenomena, numerical simulation is the tool that allows such quantification to occur. However, the numerical challenges are also formidable indeed leading to modeling assumptions. In particular, we challenge the Stokesian particle assumptions made when studying the quantification of clearance and fluid pumping. Our modeling effort falls into the discrete sub-layer modeling of individual cilium using fully numerical modeling techniques.

The organization of this work takes a natural and a systematic approach at elucidating the phenomena associated with particle-cilia interaction in the respiratory system.

- Chapter 2 introduces our problem of interest by presenting a simplified model and expanding on assumptions presented in the introduction as it relates to our problem of interest. We then describe the governing equations and numerical methods used the solution process. We present a short verification section of our methodology by comparing to two classical problems with analytical solutions: Stokes' First and Second problem. We close off this section by comparing our numerical simulation results with those available in the literature that closely resemble our simplified model.

- Chapters 3 and 4 detail the full characterization of our two model simplifications: an infinitely repeating single cilium unit and an infinitely repeating cilium patch. These chapter aims to explore the full parameter space involved in the configuration of our model, many of which are physiologically relevant choices. In these two chapters, we detail differences in fluid pumping and particle transport. In particular, we show for the first time differences in trajectories for infinitely small tracer particle when compared to a finite-sized particle.

- Chapter 5 explores the more realistic scenario that occurs during particle inhalation and deposition. We compare particles of different shapes and sizes, focusing on defining accurately differences in particle shape. We utilize the Aerodynamic Resistance Diameter as the sizing parameter for all particle shapes, and compare the results to those with an equivalent cross-sectional diameter. We quantify the arc length trajectories, displacements, and rotation rates to elucidate complex behavior not experienced by simple tracers or circular particles.

- Chapter 6 is concerned with the whole field transport arising from the ciliary beating. Specifically, we review chaotic advection and its connection to mixing in the periciliary layer. Additionally, we present 3 difference methodologies to evaluate the mixed state of our numerical simulations. Specifically, we find by use of the Finite-time Lyapunov Exponents that barriers to transport exist locally near cilia beat paths. We quantify the rate of mixing by the use of two separate metrics, the mixing number and the multiscale mixing norm. With these two metrics, we can show an exponential decrease in the mix-norm and therefore showing that mixing is chaotic indeed.

- Chapter 7 closes this dissertation by highlighting the key contributions of the work, and pays particular attention to the novel findings. We provide additional work that could be considered, and in particular focus on further analyses that would be of physiological relevance.

Chapter 2

Governing Equations and Numerical Methodology

2.1 Problem Formulation

Development of a representative ciliated cell numerical model requires investigating a properly simplified physical configuration, with the appropriate assumptions. Ciliated cell populations are known to be non-uniform in spacial distribution and density. Further, because the mucosal layer is composed of the mucus and periciliary fluids layers, fluid properties are not uniform which complicates the modeling. The compiled measured ranges of the mucosal layer parameters reported in Table 1.1 can show great variability, and this can occur between two distinct individuals and even within a single individual. This complicates our definition for a suitable baseline configuration. However, in defining our problem formulation, we begin by describing the simplified configuration, and then in Chapter 3 and Chapter 4, we expand our model to include the parameters of interest that we will vary.

The structure of this chapter includes first a description of the model problem. This description includes details of the geometry, and governing equations necessary to model the problem, along with appropriate assumptions. We then describe the relevant numerical methodology used to solve the governing equations, as well as a brief overview of the solution methodology. We then turn our attention to verification of the solution process by investigating two mathematical problems: Stokes' First and Second Problems. This allows us to verify that our numerical methodology is sound and that we can be confident in our numerical results. Finally, we close this chapter with a discussion of the validation of our model with comparisons to published numerical and experimental results from the literature.

2.1.1 Model Description and Assumptions

The simplified configuration that we will first describe is an infinite array of equally spaced cilia separated by a distance l_d. The model domain includes only a centrally located single cilium. All cilia are of equal length, l_c, share the same beat frequency f, and have the same beat pattern and phase, implying all cilia are beating in synchrony. A sketch of the physical domain is shown in Fig. 2.1. We remark that the individual cilia can have both a temporal phase shift and a spatial phase shift, however, for the purposes of developing our model, both remain here as equal. Later in Chapter 4, we describe more in detail how we consider a spatial shift in cilia phase. However, for all our work, temporal phase between cilia remains constant. That is to say, no neighboring cilia beat at a *larger* frequency than their neighbor. While our numerical description here allows for a temporal shift, and we certainly can allow for exploring this parameter, our surveying of the literature indicates that temporal phase shifts are difficult to measure accurately.

While the mucosal layer includes a non-Newtonian mucus layer on-top of a Newtonian fluid layer, our model is interested in the interaction between finite-sized particles and the cilium configuration. Therefore, we consider a Newtonian fluid layer that is meant to represent the periciliary fluid only, with a defined fluid layer height h_p. We acknowledge that this assumption does not mimic the *in-vivo* scenario, but also note that some experimental methods to measure cilia transport may include locally removing mucus from the luminal trachea section. Other authors have removed mucus intentionally to track polystyrene beads across cilia to measure disease severity [68, 69]. Additionally, in certain diseased conditions, such as ARDS, increased mucus production could lead to an additional increase in periciliary fluid as well. In some cases, this can lead to cilia not penetrating the mucus layer in their

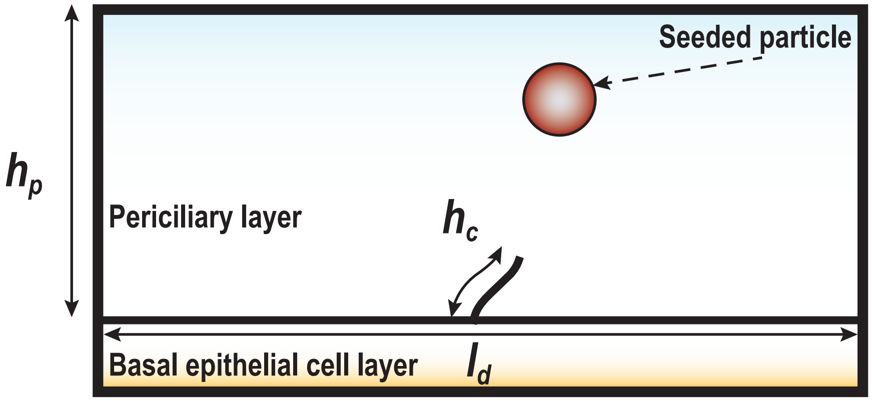

Figure 2.1: Sketch of the single cilium model domain. Not drawn to scale.

beat cycles. This is inline with our investigation of cilia beating in the Newtonian periciliary layer, and is indeed a first step towards developing a more comprehensive cilia model.

The cilia-particle-fluid model occupies a region of space in the Cartesian coordinate frame denoted by $\mathcal{S} \subset \mathbb{R}^d$, for $d = 2$ or 3. For simplicity, our model is 2 dimensional, $d = 2$, and therefore $\vec{x} = (x, y) \in \mathcal{S} | x_l \leq x \leq x_r, y_t < y < y_b$, where x_l, x_r are the left and right boundaries, and y_t, y_b are the top and bottom boundaries. The fluid domain occupies a subregion of space denoted by $\mathcal{F} = \mathcal{F}(t) \subseteq \mathcal{S}$ for all time t, with velocity $\vec{v}(\vec{x}, t) = \langle u, v \rangle$. Then, the governing equations of motion for the periciliary fluid are the incompressible Navier-Stokes equations given by Equations 2.1-2.2.

$$\vec{\nabla} \cdot \vec{v}(\vec{x}, t) = 0 \tag{2.1}$$

$$\rho_p \left(\frac{\partial \vec{v}}{\partial t}(\vec{x}, t) + \vec{\nabla} \cdot (\vec{v}(\vec{x}, t) \otimes \vec{v}(\vec{x}, t)) \right) = -\vec{\nabla} p(\vec{x}, t) + \mu_p \vec{\nabla}^2 \vec{v}(\vec{x}, t) + \vec{f_b}(\vec{x}, t) \tag{2.2}$$

Equation 2.1 is the incompressible mass continuity equation, and Equation 2.2 is the momentum equation, where the parameters ρ_p, μ_p correspond to the density and viscosity of the periciliary layer. The variables $\vec{v}(\vec{x}, t)$, $p(\vec{x}, t)$, and $\vec{f_b}(\vec{x}, t)$ all correspond to the spatial time-varying functions for Eulerian velocity, pressure, and body forces respectively. The

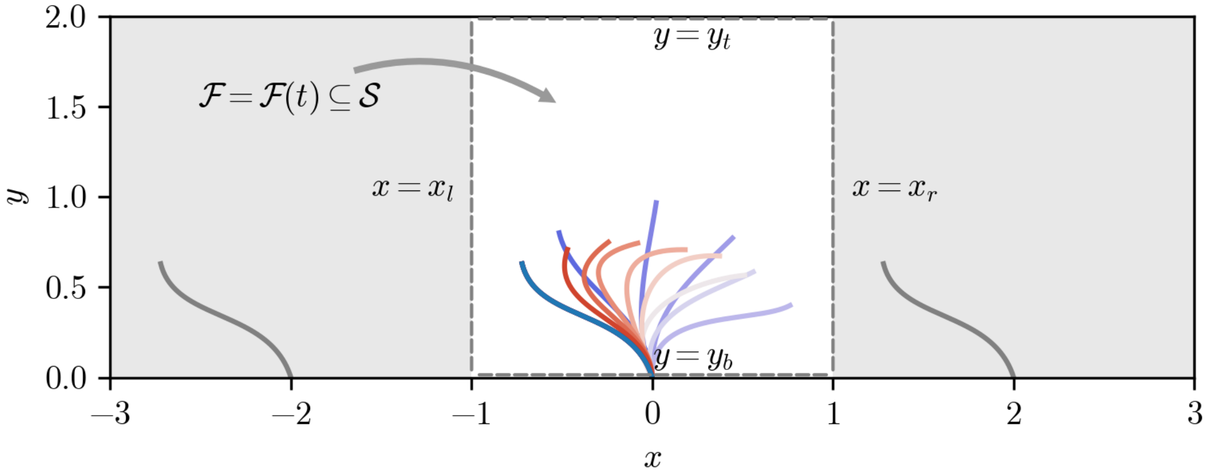

Figure 2.2: Fluid domain for solving the governing equations. The centrally located single cilium is shown with base at $(x, y) = (0, 0)$. The beat cycle is shown at 13 snapshots, where the forward stroke is shown in blue, and the backward stroke is shown in red. The beat shape kinematics is reproduced from Fulford and Blake [34]. The fluid domain, $\mathcal{F}$ has periodic boundary conditions at $x_r = 1$ and $x_l = -1$. The grey repeating units are shown only as a visualization of the periodic nature of the problem formulation.

forcing term in Equation 2.2, $\vec{f_b}(\vec{x}, t)$, corresponds to any body force on the fluid. We impose periodic boundary conditions along $x = x_r$ and $x = x_l$, and require a no-slip velocity boundary condition along $y = y_t$ and $y = y_b$. We initialize the velocity field, $\vec{v}(\vec{x}, t)|_{t=0} = 0$ in the entire domain. In Section 2.2.2, we describe the body force, $\vec{f_b}(\vec{x}, t)$ details as it pertains to the immersed boundary method coupling between the Eulerian fluid domain and the Lagrangian rigid or deforming structure domain.

We have not specified the use of dimensions thus far, and our equations are valid for any choice of units, but now we non-dimesionalization of our problem formulation, by the use of appropriate scale units. Our choice of dimensionless quantities are: length $l^* = \frac{l}{l_c}$; $l_c = 10\mu\text{m}$ where l_c is cilium length; time, $t^* = \frac{t}{T}$; $T = \frac{1}{f}$ where f is cilia beat frequency; velocity, $u^* = \frac{u}{f l_c}$; and pressure $p^* = p\frac{l^2}{\mu f}$. With these choices of non-dimensionalization, we introduce Reynolds number, the non-dimensional parameter, as:

$$Re = \frac{\rho l^2 f}{\mu} \tag{2.3}$$

Our choice of Reynolds numbers follows from choosing the frequency of oscillation times the length scale as our characteristic "velocity", and the length of the cilium as our characteristic length. For all our simulations we solve the non-dimensional equations, and report dimensional results in post-processing. Additionally, we keep the Reynolds number constant in our simulations.

The motion of the cilium used is reproduced from the canonical beat pattern of rabbit trachea [34], which was generalized to model the human beat pattern. Recent experimental studies have measured cilia beat characteristics between several species systematically and have found that the beat frequency is highly conserved between species [70]. The arc length of the beat pattern was reconstructed by as parametrized vector equation, $\vec{\xi}$, which is decomposed using a Fourier sum in Equation 2.4,

$$\vec{\xi}(s,t) = \frac{1}{2}\vec{a}_0(s) + \sum_{n=1}^{N_0}\Big(\vec{a}_n(s)\cos(\sigma t) + \vec{b}_n(s)\sin(\sigma t)\Big) \tag{2.4}$$

with the following Fourier coefficients:

$$\vec{a}_n(s) = \sum_{m=1}^{M_0}\vec{A}_{mn}s^m \tag{2.5}$$

$$\vec{b}_n(s) = \sum_{m=1}^{M_0}\vec{B}_{mn}s^m \tag{2.6}$$

The frequency of the beat, f, is defined by the relation $\sigma = f/2\pi$. The parametrized vector equations, $\vec{\xi}$, describe the motion along the cilium curve length $0 < s < l_c$, with the base at $s = 0$, and beat cycle beginning at $t = 0$ and ending at $t = T$. The fluid domain and its boundaries, along with the specified beat kinematics shape is shown in Figure 2.2. We will note here that the beat shape is described in terms of a non-dimensional length.

We now summarize our modeling assumptions as they pertain to the cilium geometry, fluid layer properties, and cilia beat kinematics:

- The single cilium repeating unit, is a [20 × 20μm] square, with a centrally located cilium with base at $(x, y) = (0, 0)$, with a cilium length of 10 μm. Figure 2.1 depicts the model domain.

- This model problem is an infinite array of cilia that are all equally spaced, 20μm apart, beating in phase, both temporally and spatially.
- The beat kinematics are prescribed as the motion of a rigid structure with shape given by Equation 2.4.
- The fluid layer is a Newtonian fluid with viscosity μ_p and density ρ_p, whose evolution is described with the incompressible Navier-Stokes equations (Eq. 2.1 and 2.2)
- The total elapsed time is 12 beat periods, $T_{\max} = 12T$, unless otherwise noted.
- The Reynolds number is defined by Equation 5.1, and is kept at a constant value of $Re = 1.0$, and is modified where noted for specific problem comparisons.

2.2 Numerical Modeling

Realistic physical phenomena that involve interactions between fluids and solids are categorized as fluid-structure interaction (FSI) problems, which are encountered in many areas of engineering and physics. Several methodologies exist to solve FSI problems, and their broad categories can be generalized as weakly-coupling and strongly coupling [71]. The specific governing equations of each category directly influences the numerical implementation, where weakly-coupled methods involve iterative schemes that solve the fluid and structural equations until a solution is found, while the strongly coupled methods solve the equations simultaneously. We note that strongly-coupled methods sometimes require additional complexity in the description of the discrete fluid-structure equations, which usually results in solving the equations on a body-fitted mesh requiring frequent remeshing.

The immersed boundary method is a popular method used for solving FSI problems, where the description of the fluid equations are on a regular grid, and the structural equations are defined in an embedded Lagrangian grid [72]. This makes implementation very attractive for the class of problems where large deformations exist, thereby completely eliminating the regrid operations that body-fitted mesh methods require. However, as described in Section 1.3.2, the low Reynolds number flows we are interested in studying, lend to other methodologies that do not require solving the full incompressible Navier-Stokes equations, as we have presented in Equations 2.1 and 2.2. The method of Regularized Stokeslets [73] and more recently coupled with boundary integral methods [74] have been used to explore phenomena associated with cilium-mediated transport, and additionally several others exist (e.g. [44, 75, 76]). However, we chose the immersed boundary method due to its ability to model arbitrary shapes with rigid body motion, as is done for finite-sized particle transport. In this section, we describe the immersed boundary method, and the governing equations followed by a brief description of the solution methodology.

2.2.1 The Immersed Boundary Method

The numerical algorithm used is the immersed boundary method, which was developed originally for coupling of a viscous incompressible fluid domain to that of an elastic structure domain [77, 78]. Peskin originally developed the method in the 1970's for applications to the cardiovascular system (recent work includes heart valves, deformation of arteries, and full heart structure), and it has been used for a wide range of biomechanical modeling efforts in aquatic locomotion [79], microswimmer motion [80, 81], insect flight [82, 83], and respiratory flows.

At the center of the immersed boundary method is the coupling between the body force, $\vec{f_b}(\vec{x}, t)$, and the fluid through Equations 2.7-2.9. As described earlier, the Eulerian description of the fluid is defined in Cartesian coordinates on the physical space, $\mathcal{F} \subset \mathcal{S}$. Each immersed body occupies a subregion of $\mathcal{S}$, and is denoted as $\mathcal{B} = \mathcal{B}(t) \in \mathcal{S}$, where the union of all immersed bodies and fluid domain $\mathcal{F} \cup \mathcal{B}_1 \cup \mathcal{B}_2 \cup ... \cup \mathcal{B}_i$ form a non-overlapping set. Here we define the mapping between the material points s and the Cartesian coordinates, $\vec{X}(s,t)$. The spreading of the body force is accomplished by the integral relation shown in Equation 2.7,

$$\vec{f_b}(\vec{x},t) = \int_{\mathcal{B}} \vec{F}(\vec{X},t)\delta(\vec{x} - \vec{X}(s,t))\mathrm{d}s \tag{2.7}$$

$$\frac{\partial \vec{X}(s,t)}{\partial t} = \vec{U}(s,t) \tag{2.8}$$

by picking an appropriate Dirac delta function, $\delta(\vec{x})$. The interpolation of the immersed structure Lagrangian velocity, $\vec{U}(s,t)$, to the local fluid velocity, $\vec{v}(\vec{x},t)$ is accomplished similarly in Equation 2.9.

$$\vec{U}(s,t) = \int_{\mathcal{F}} \vec{v}(\vec{x},t)\delta(\vec{x} - \vec{X}(s,t))\mathrm{d}\vec{x} \tag{2.9}$$

The specific version and implementation of the immersed boundary method used was developed by Bhalla et al. and it is a distributed Lagrange multiplier formulation for the kinematic and rigidity constraints [85]. This formulation is an extension of the method developed by Shirgaonkar et al. and follows the fictitious domain method created for particulate flows by Glowinski et al. and Patankar [86–88]. Two-way coupling between a solid rigid body and the fluid is accomplished from the implicit coupling of the fluid equations of motion inside and on the surface any arbitrary shaped defined as an immersed boundary without the need for any drag model. This is used for embedded particles that fully respond to the fluid motion created by the beating cilia, thereby requiring no additional fluid- structure interaction model for the specific particle dynamics. This constraint based formulation makes no distinction between the type of immersed bodies, thereby allowing elastic structures, prescribed motion bodies, and rigid bodies to coexist and interact. Thus, the cilium kinematics is prescribed in a one-way coupling between the structure and the fluid.

This dual implementation used is found in the open-source library: Immersed Boundary

Adaptive Mesh Refinement (IBAMR) [89]. IBAMR is an immersed boundary method C++ library with support for distributed-memory parallelization. The library supports a structured Cartesian grid with optional adaptive mesh refinement. We utilize this capability to reduce the numerical computation time in order to run all our simulations.

2.2.2 Solution Methodology

The immersed boundary method is an attractive method for the type of problem considered here due to its ability to solve the equations of motion on a rectangular grid, and simultaneously allowing the immersed boundary to be discretized in the Lagrangian reference frame where it is not required to conform to the underlying rectangular grid. The communication is done through the discrete interpolation operators. In this section, we briefly describe numerical methodology used in the open-source code: IBAMR. For a complete description see [90–92]. The specific implementation of the constraint immersed boundary method is described in detail in [85].

First, the discrete fluid velocity is defined at the cell centers and faces, where the cell face velocities are the standard MAC (marker and cell) velocity. The divergence and gradient operators, which are denoted $\vec{D}$ and $\vec{G}$ respectively, are discretized using second-order finite differences on underlying Cartesian grid. The non-linear advective term, $\nabla(\vec{v} \otimes \vec{v})$, in the Navier-Stokes equation is discretized using a second-order piece-wise parabolic method (PPM) [93], denoted by $\vec{N}(\vec{v})$, which is a version of the Godunov scheme used in compressible flow simulations [94]. The resulting equations of motion on the Eulerian grid are evolved in time, where the time discretization is treated using the implicit midpoint rule for linear terms, while the non-linear terms are treated explicitly. The velocity at the half time steps is $\vec{v}^{n+\frac{1}{2}} = \frac{1}{2}(\vec{v}^{n+1} + \vec{v}^{n})$. The governing discrete fluid flow equations are represented with discrete operators in equations (2.10) and (2.11).

$$\vec{D} \cdot \vec{v}^{n+1} = 0 \tag{2.10}$$

$$\rho_p \left(\frac{\vec{v}^{n+1} - \vec{v}^{n}}{\Delta t} + N(\vec{v}^{n+\frac{1}{2}}) \right) = -\vec{G} p^{n+\frac{1}{2}} + \mu_p \vec{L} \vec{v}^{n+\frac{1}{2}} + \vec{f}^{n+\frac{1}{2}} \tag{2.11}$$

This is a coupled non-linear system of equations, which is linearized using fixed-point iteration with a set number of sub-cycles, $k = 0, 1, ..., n_{\text{cycles}}$. At each sub-cycle, the linearized system (2.12)

$$\begin{bmatrix} \frac{\rho_p}{\Delta t} I - \frac{\mu_p}{2} L_x & 0 & G_x \\ 0 & \frac{\rho_p}{\Delta t} I - \frac{\mu_p}{2} L_y & G_y \\ -D_x & -D_y & 0 \end{bmatrix} \begin{bmatrix} u^{n+1,k+1} \\ v^{n+1,k+1} \\ p^{n+1,k+1} \end{bmatrix} = \begin{bmatrix} (\frac{\rho_p}{\Delta t} I - \frac{\mu_p}{2} L_x) u^n - \rho N_x^{n+\frac{1}{2},k} + f_y^{n+\frac{1}{2}} \\ (\frac{\rho_p}{\Delta t} I - \frac{\mu_p}{2} L_y) v^n - \rho N_y^{n+\frac{1}{2},k} + f_y^{n+\frac{1}{2}} \\ 0 \end{bmatrix} \tag{2.12}$$

is solved by using using a flexible GMRES algorithm with a preconditioner based off of the projection method. The implementation is only first-order accurate both temporally and spatially, however, second-order accuracy is achieved spatially when the problem considered is sufficiently smooth [90].

2.3 Verification

The open-sourced IBAMR code has the capability to simulate a variety of fluid-structure interaction problems ranging from heart valve simulations [95], free-body swimming [79], interfacial rigid-body flows [85], and multiphase simulations of suspended structures [96, 97]. We conduct verification of the code for problems in the regime of interest, however, extensive verification and validation of cases published by the developers of IBAMR will not be revisited, except in cases that capture the fluid dynamical behavior similar to that of beating cilia. In our verification process, we first compare results from Stokes' First and Second Problems in a full refined mesh. For Stokes' First Problem, we evaluate the convergence properties for an indiscriminate change in the temporal and spatial resolutions. For Stokes' Second Problem, we aim to solve an oscillatory problem with a well described solution. Then we turn our attention to the simplified model problem and perform a mesh convergence study, with a fully dense mesh and utilize IBAMR's adaptive mesh refinement capabilities to show more than reasonable agreement in the results.

The incompressible Navier-Stokes solver used in the Constraint-IB version [85, 90] is a time-splitting technique and is subject to the traditional CFL condition,

$$\|\vec{u}_{\infty}\|\frac{\Delta t}{\Delta x} \leq C \tag{2.13}$$

which in practice is used as a time step controlling parameter. At moderate and high Reynolds number, the time step restriction is dominated by the convective term, however, at low, but finite Reynolds number, $\mathcal{O}(10^{-1}, ..., 10^{-4})$, the viscous terms in the Navier-Stokes equations dominate the time step restriction, so following Taira and Colonius [98], we adopt a viscous CFL condition,

$$\beta \leq \nu \Delta t / \Delta x^2 \tag{2.14}$$

We present results for a variety of mesh resolutions and time-steps, in addition to results with constant values of β.

Finally, we remark that much of the verification, validation, and the presentation of bulk fluid parameters, we utilize the cross-sectional velocity or cross-sectional flow rate as our quantity of interest. Specifically, our cross-sectional velocity along the x-direction is defined as:

$$u(y,t) \text{ at } x = 0 \tag{2.15}$$

and the cross-sectional flow rate

$$Q(t) = \int_0^y u dy \tag{2.16}$$

where y is taken to mean the vertical distance in the y-direction of the simulation domain, and is problem domain dependent.

2.3.1 Comparison to Analytical Solutions

We validate our results by considering the following problem: impulsively start an infinitely long plate from rest in a quiescent viscous fluid, known as Stokes' First and Second Problem. These classical problems allow us to compare a numerical solution to the analytical function describing the velocity field. We begin by assuming that velocity varies only in one direction and is only a function of the vertical distance from the plate's surface,

$$u = u(y, t) \tag{2.17}$$

$$v = 0 \tag{2.18}$$

which satisfies the conservation of mass equation immediately. Additionally, when considering the momentum equation in $y-$direction and the conservation of mass equation, we can show that pressure is only dependent on the hydrostatic pressure, and varies only as a function of the vertical distance,

$$0 = \frac{\partial p}{\partial y} - \rho g \tag{2.19}$$

Finally, we can reduce the full Navier-Stokes Equations to only the momentum in $x-$direction:

$$\frac{\partial u}{\partial t} = \nu \frac{\partial^2 u}{\partial y^2} \tag{2.20}$$

where $\nu = \frac{\mu}{\rho}$ is the fluid kinematic viscosity, the initial conditions are,

$$u(y, t = 0) = 0 \tag{2.21}$$

and the appropriate boundary conditions at the plate and infinity:

$$u(y = 0, t) \;\; = u(t), \tag{2.22}$$

$$u(\infty, t > 0) = 0 \tag{2.23}$$

For Stokes' First problem, the plate velocity is constant, $u(t) = u_{\text{plate}}$, which results to an infinitely growing boundary layer of thickness, $\delta \sim \sqrt{\nu t}$. The solution to Equation 2.20 is given in terms of the complementary error function,

$$u(y, t) = u_{\text{plate}} \operatorname{ercf}\left(\frac{y}{\sqrt{4\nu t}}\right) \tag{2.24}$$

For Stokes' Second problem, the plate oscillates between u_{plate} and $-u_{\text{plate}}$ at an angular frequency of ω, $u(t) = u_{\text{plate}} \cos(\omega t)$. Similarly, the boundary layer penetration length in this case is proportional to the inverse square root frequency of oscillation times the kinematic viscosity $\delta \sim \sqrt{2\nu/\omega}$. Similarly, the solution in this case is given by,

$$u(y, t) = u_{\text{plate}} e^{\left(-\sqrt{\frac{\omega}{2\nu}} y\right)} \cos\left(\omega t - \sqrt{\frac{\omega}{2\nu}} y\right) \tag{2.25}$$

We use the boundary layer penetration length to select the time at which to compare solutions of varying Reynolds number, however, those results are not presented in these sections. The problem domain is shown in Figure 2.3.

For Stokes' First Problem, we define Reynolds number using the plate velocity, u_{plate}, as the characteristic velocity,

$$Re = \frac{u_{\text{plate}} L}{\nu} \tag{2.26}$$

but note that this definition is different than defined in Section 2.1.1. However, for Stokes' Second Problem, we use the angular frequency times the characteristic length as the char-

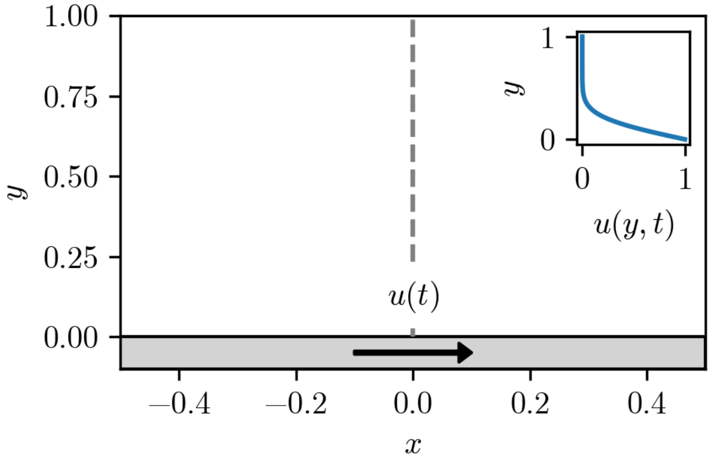

Figure 2.3: The simulation domain for Stokes' First and Second Problem. The inset shows the analytical solution for Stokes First Problem at the $x = 0$ cross-section.

acteristic velocity, leading to Reynolds number defined as,

$$Re = \frac{L^2\omega}{\nu} \tag{2.27}$$

In order to evaluate the difference between the analytical (u) and numerical ($\hat{u}$) solutions, we calculate the difference between the two quantities computed at each discrete point along the vertical distance, y_i for $i \in 1, ..., N$, where N is the total number of grid points,

$$e_i = u_i - \hat{u}_i \tag{2.28}$$

Then, we report the L^2-norm, $\|e\|_2$, and the root mean-squared error, $RMSE$, (or discrete L^2-norm) of the error between the analytical (u) and numerical ($\hat{u}$) velocity in the direction of the moving plate,

$$\|e\|_2 = \left(\sum_{i=1}^{N} |e_i|^2 \right)^{1/2} \tag{2.29}$$

$$RMSE = \left(\frac{1}{N} \sum_{i=1}^{N} |e_i|^2 \right)^{1/2} \tag{2.30}$$

$$\tag{2.31}$$

.

Stokes' First Problem

We set $u_{\text{plate}} = 1.0$, pick characteristic length $L = 1.0$, and allow the kinematic viscosity to be set by the specified definition of the Reynolds number, i.e. $\nu = u_{\text{plate}} L/Re$. We run various values of Reynolds number ($Re = 0.1, ..., 500$), but only report convergence results for the more viscous regime, at $Re = 0.1$ to test the limits of convergence for our regime of interest.

The numerical simulation domain is a square of equal length and height, $L = H = 2$, with an immersed boundary structure that is discretized by a ratio of 1:1 Lagrange point density to mesh resolution density. At time $t = 0$, the immersed structure is started from rest, and pulled in the positive $x-$direction with velocity $u_{\text{plate}} = 1.0$.

In Figure 2.4, we reported the errors for constant values of Δx and Δt (Fig. 2.4a and Fig.2.4b respectively). In Figure 2.4a, we keep the value of Δt constant, and show that simply decreasing the mesh resolution, does not indicate convergence, and in fact the error grows. Further, in Figure 2.4b, we show that reducing the time-step arbitrarily, while keeping Δx constant, also does not show a decrease in error. For any given mesh resolution density, we must be careful in not reducing the value of Δt arbitrarily or else we will increase the error once again. This increase in error is attributed to the approximate projection step used to calculate the intermediate pressure from a solution to the discrete Poisson problem, which

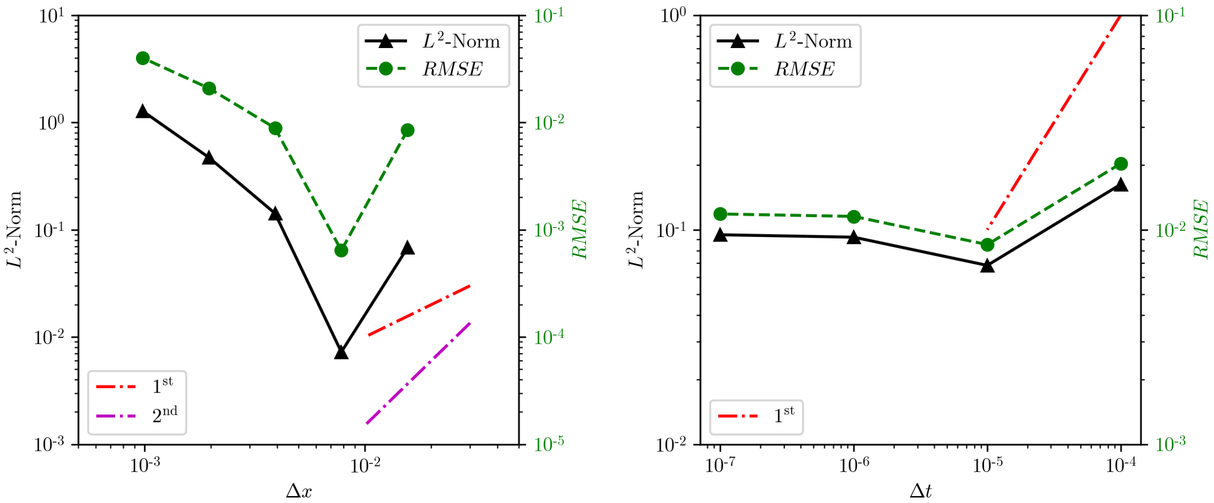

(a) Error at constant value of $\Delta t = 1 \times 10^{-5}$. First order and second order convergence rate shown in red and purple dashed-dotted lines, respectively.

(b) Error at constant value of $\Delta x = \frac{1}{nx}$ where $nx = 128$. First order convergence rate shown in red dashed-dotted line.

Figure 2.4: Error between analytical solution and numerical solution for Stokes' First Problem. The solid black lines correspond to the L^2-norm between the analytical solution and the numerical solution. The dashed green lines correspond to the RMS-error between the analytical solution and numerical solution.

is a known stability problem with time-splitting methods (see [99–101]). For low Reynolds number flows, this projection step requires stricter tolerances and a higher number iterations which makes it difficult to achieve convergence.

As in Taira and Colonius [98], we report the error for varying values of viscous CFL, $\beta = \frac{\nu \Delta t}{\Delta x^2}$. In Figure 2.5, we show that for a fixed mesh resolution of $\Delta x = \Delta y = \frac{1}{128}$, the error can be decreased in a controllable fashion, but once again rises after some minimum value of β. While we are not formally assessing convergence of IBAMR, these empirical results show that there is an optimum value of β beyond which decreasing Δt is no longer valuable, and indeed can be detrimental to the solution. The discrete Poisson problem used as a preconditioner would require higher tolerances, which would take higher iterations at these smaller time-steps.

Finally, to show mesh convergence, we run a series of simulations that hold β constant by decreasing the value of Δx and Δt in a controllable fashion (i.e. $\Delta t = \frac{\beta \Delta x^2}{\nu}$). We select

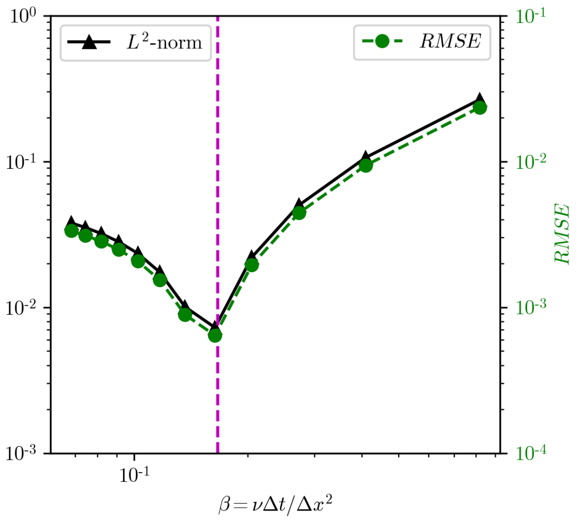

Figure 2.5: Error between analytical and numerical simulation for Stokes' First Problem. Here we fix the mesh resolution at $\Delta x = \Delta y = \frac{1}{128}$, and vary the time resolution.

the baseline viscous CFL $\beta_1 = 0.1024$, and show convergence for values above and below the local minimum shown in Figure 2.5, $\beta \approx 0.163$ (purple dashed-line). In Figure 2.6, we show the first order decrease in the L^2-norm that is expected (red dash-dotted line for reference). However, we note that a lower value of $\beta = 0.05\beta_1$ (Fig. 2.6a) does not have an actual lower error than the higher $\beta = 0.2\beta_1$, indicating that a reduction in time resolution does not indicate a lower error.

Stokes' Second Problem

Next, we look at a more transient problem akin to our oscillatory cilia beat problem. The same plate is impulsively started from rest in an doubly periodic domain, but oscillates with velocity $u(t) = u_{\text{plate}} \cos(\omega t)$, with $u_{\text{plate}} = 1$, and frequency $\omega = 2\pi$. We once again use the Reynolds number, as defined in Equation 2.27, as the controlling parameter in our simulations. By setting our characteristic length scale to $L = 1$, we require that the ratio between the oscillation frequency, ω and the kinematic viscosity, ν, remain constant. As for Stokes' first problem, we also report the errors between the analytical and numerical velocity in the positive x-direction. The numerical simulation domain is a square of equal length and

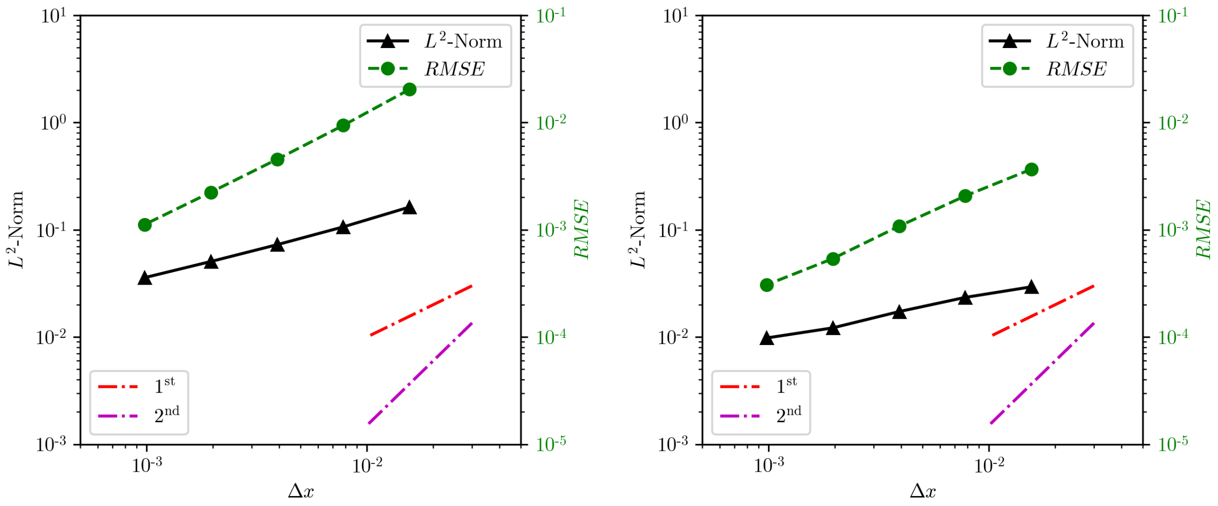

(a) $\beta = 0.05\beta_1$

(b) $\beta = 0.20\beta_1$

Figure 2.6: Mesh convergence for two separate values of viscous CFL, $\beta = \varrho\beta_1$ for $\varrho = 0.05, 0.20$.

height, $L = H = 2$, with an immersed boundary structure that is discretized by a ratio of 1:1 Lagrange point density to mesh resolution density. At time $t = 0$, the immersed structure is started from rest, and oscillates initially toward in the positive $x-$direction with velocity $u(t) = u_{\text{plate}} \cos(\omega t)$.

As in our results from Stokes' first problem, we find similar behavior in error reduction between the analytical solution and numerical solution for an indiscriminate decrease in Δt. In Figure 2.7, the mesh resolution is held constant at $\Delta x = \frac{1}{128}$, and we see a sharp decrease in error up until about $\beta = 0.1$, then an increase once again. These results are consistent with [98], and for all proceeding simulations, we utilize this viscous CFL condition of $\beta \leq \frac{\nu \Delta t}{\Delta x}$, and set $\beta = 0.4096$ to validate our cilia driven flow results. In the next section, we validate our numerical simulations with experimental measurements and comparisons to other similar numerical simulations.

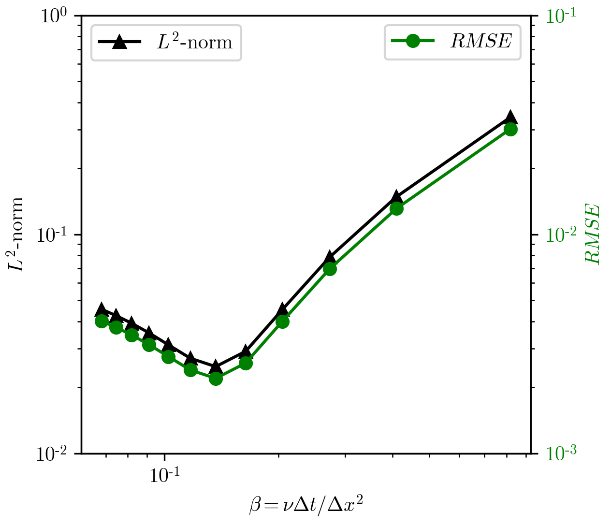

Figure 2.7: Error between analytical and numerical simulation for Stokes' Second Problem. Here we fix the mesh resolution at $\Delta x = \Delta y = \frac{1}{128}$, and vary the time resolution.

2.3.2 Mesh Convergence

As described previously, our need to carefully show that convergence has been achieved for our test problems (Stokes' first and second problems), we can now show convergence for the problems of interest of cilia-particle transport. We aim to show that our numerical simulation converges as we increase mesh resolution while satisfying the viscous CFL condition $\beta \leq \frac{\nu\Delta t}{\Delta x^2}$. Additionally, our choice of using the IBAMR numerical simulation software library as our tool was motivated by the ability to utilize adaptive mesh refinement (AMR). Thus in our mesh convergence, we also compare fully dense simulations to those with AMR. The refinement strategy comes from the SAMRAI library [102], which has a large variety of options for accomplishing AMR across different grids. In the case of IBAMR, the AMR strategy allows the users to refine a regularly-space coarse Cartesian grid in the following manner. First, lets assume that the 2-dimensional mesh, $L_x \times L_y$ in length and height, is uniformly spaced, that is $\Delta x = \Delta y = \frac{L_x}{n_x} = \frac{L_y}{n_y}$, where n_x and n_y correspond to the number of grid points along the x and y axes. The grid resolution at a particular refinement level, l, is denoted by a superscript corresponding to the refinement level, n^l, where n_x^0, n_y^0, correspond to the coarsest level. By selecting the coarse mesh grid points, (n_x^0, n_y^0), the number of refinement levels (l), and refinement ratio (r), the successive grid points are calculated from the following:

$$\Delta x_l = \frac{L_x}{n_x^0 r^l} \tag{2.32}$$

The set of numerical simulations for mesh convergence use the 2D square domain previously describe in Section 2.1.1. We selected 5 mesh densities by setting the number of points per unit of non-dimensional length L_{nx}, which, in our problem domain corresponds to half the full computational domain $2L_{nx} = L_x = L_y = 2$. Our choices of problem parameters are shown below in Table 2.1. We remark here the challenge with using the time-splitting techniques at lower Reynolds number, as the calculated values of Δt scale with the inverse of ν, indicating an increase in the condition number when solving the Navier-Stokes equations.

Nonetheless, when controlling the viscous CFL parameter, we can indeed reduce the numerical error between subsequently refined mesh resolutions. In Figure 2.8, we plot the cross-sectional flow rate, $Q(t) = \int_0^{y_t} u_x dy$, after one complete beat cycle. For both values of β, we see that the solution approaches a true solution, indicating that mesh convergence has been achieved, which we later show a more quantitative comparison by calculating the normalized RMS-error. In the absence of using a controlled value of β, results show a diverging flow rate profile when reducing the time step far too low (results not shown).

nx	Δx	Δt for $\beta = 0.4096$	Δt for $\beta = 0.1024$
8	0.125	6.40E-04	1.60E-04
16	0.0625	1.60E-04	4.00E-05
32	0.03125	4.00E-05	1.00E-05
64	0.015625	1.00E-05	2.50E-06
128	0.0078125	2.50E-06	6.25E-07

Table 2.1: Values chosen for mesh resolution refinement study and calculated time-stepping values from keeping a constant β value.

Additionally, for our AMR simulations, we select the 3 finest mesh resolutions (which also encapsulate the 3 coarsest mesh resolutions). Specifically, we select 2 refinement levels ($l = 0, 1, 2$), at a ratio of refinement of 2 (r=2), which, for example, would give a coarse level

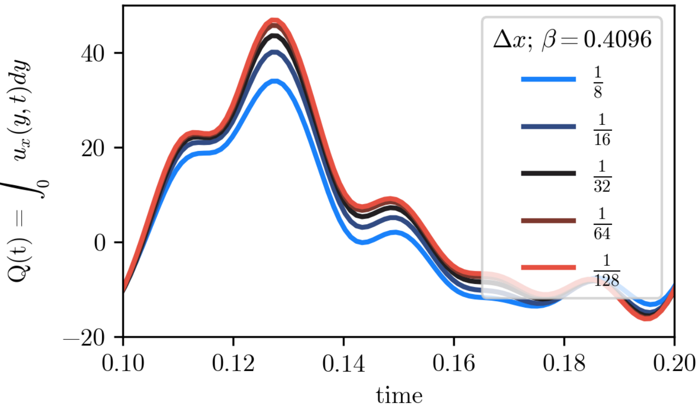

(a) Cross-sectional flow rate for various increasing spatial resolutions for a fully dense mesh. Viscous CFL condition $\beta = 0.1024$.

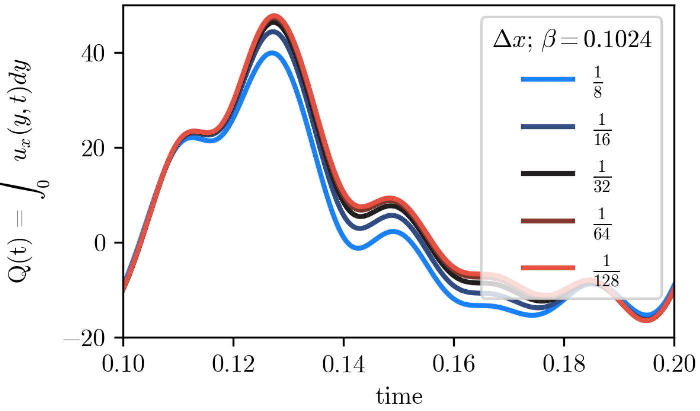

(b) Cross-sectional flow rate for various increasing spatial resolutions for a fully dense mesh. Viscous CFL condition $\beta = 0.4096$.

Figure 2.8: Mesh refinement study for fully dense mesh at different viscous CFL conditions, and AMR configuration. In Figure 2.8a and 2.8b we plot cross sectional flow rate $Q(t)$ at $x = 0$, for various spatial resolutions. The viscous CFL condition, $\beta =\leq \nu\frac{\Delta t}{\Delta x^2}$, varies between Figure 2.8a and 2.8b, at $\beta = 0.1024$ and 0.4096 respectively.

mesh resolution of $\Delta x_0 = \frac{1}{32}$, and the finest level mesh resolution would have 2^l as many cells, namely $\Delta x_{l=2} = \frac{1}{32(2^l)} = \frac{1}{128}$. We calculate the corresponding time step from the finest mesh level we utilize, since that will give the more restrictive condition on the viscous CFL. We then extract the flow rate profile along the y-direction and plot this value a function of time. In Figure 2.9 we see that our flow rate profiles indeed collapse onto the finest mesh, and the difference is more than acceptable.

Unlike our mesh refinement of the analytical problems in section 2.3.1, we do not have a *true* solution to compare our numerical results. Thus, we pick the finest mesh resolution as the reference solution ($\hat{u}^{128}$) as is customary in mesh convergence studies, $\Delta x = \frac{1}{128}$, and calculate the error between the finest mesh and subsequent coarse mesh resolutions,

$$e_i = \hat{u}_i^{128} - \hat{u}_i \tag{2.33}$$

then we computer the normalized root-mean squared error,

$$NRMSE = \frac{1}{u_{\max} - u_{\min}} \left(\frac{1}{N} \sum_{i=1}^{N} |e_i|^2 \right)^{1/2} \tag{2.34}$$

However, we must note that for the AMR results, we do compare all AMR resolutions to the fully dense finest resolution, and not between successive refinements. We plot these results in Figure 2.10, which show less than a 1% difference between the two finest mesh resolutions. For our AMR mesh comparison, we see a similar set of results, when comparing the two finest AMR meshes,there is a difference of about 0.4%. When comparing the results of the next finest mesh, $\Delta x = \frac{1}{64}$, we see a difference of less than 2%, which we find acceptable for all future simulations. These two pairs of results show that for our choice of viscous CFL, and mesh resolution, we have numerical convergence.

2.4 Validation

Direct validation of numerical simulations with experimental data across various low Reynolds number applications is difficult due to the microscale nature of the flow conditions. In some work, researchers take primary human bronchial epithelial cells, culture them to confluency and subsequent differentiation that mimic the *in-vivo* conditions inside of a human. In other work, researchers directly excise tracheae from human organ donors, cut along the sagittal plane, and unfold the trachea to perform experiments on cilia characterization. Conversely,

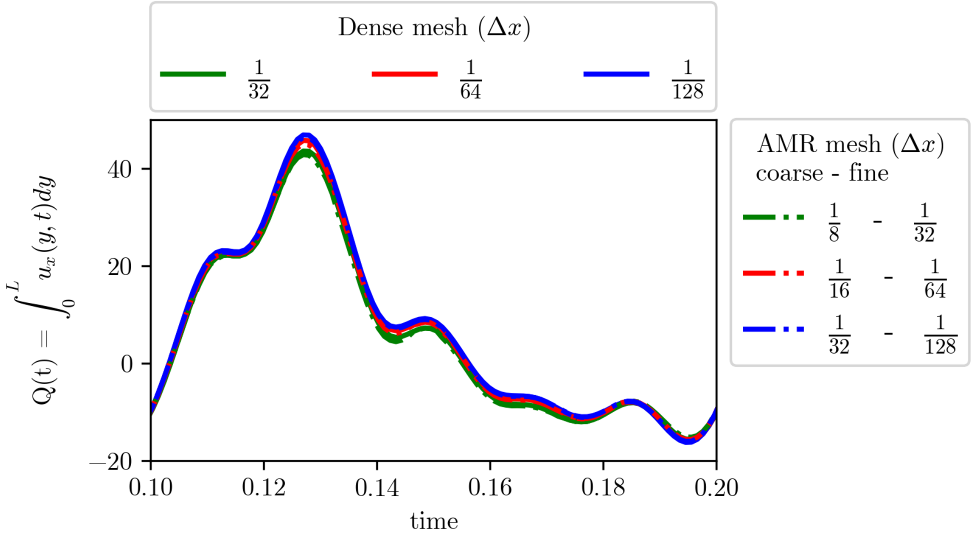

Figure 2.9: Mesh refinement comparison between AMR mesh, and fully dense mesh at various spatial resolutions; $\beta = 0.4096$.

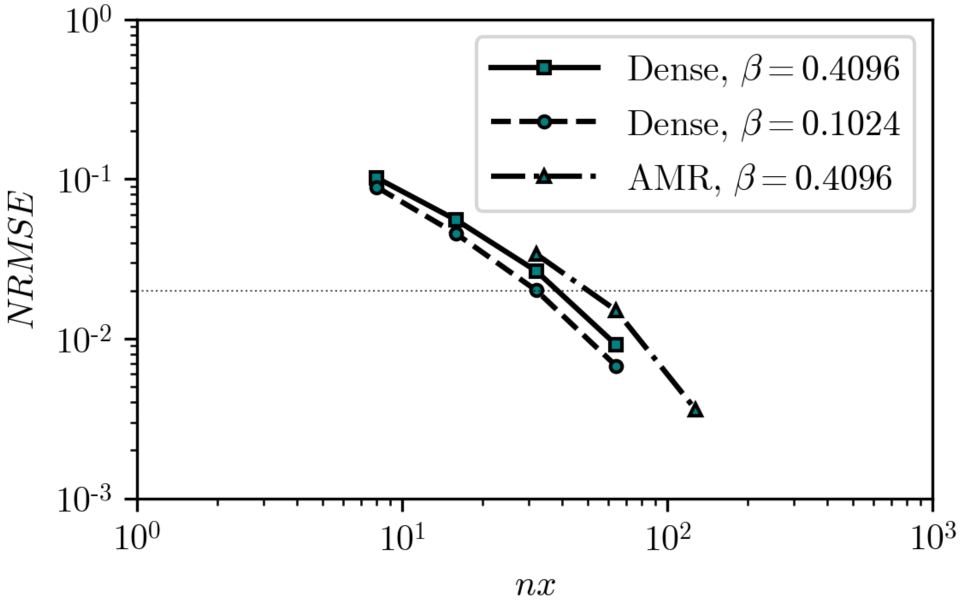

Figure 2.10: Normalized root-mean squared error between successive mesh refinements. Each dense mesh is compared to a mesh density of $nx = 128$ points per unit length. Additionally, all AMR meshes are compared to this density. The horizontal fine-dotted line corresponds to a difference of 2%.

numerical modeling efforts by various researchers make assumptions that narrow down the complexity, but keep some of the underlying flow physics that they wish to explore. When studying the internal cilia mechanics and hydrodynamic coupling, assumptions about the cilium functional groups and their interaction are made in order to predict the beating shape. In our work, we have *prescribed* the shape, and thus kept the focus of our work to the effect that a single repeating cilium unit beating synchronously with its neighbor has on the flow physics, and not the emergence of cilia beat shape from hydrodynamic coupling. This assumption has been made in variety works by researchers studying 2D and 3D ensembles of cilia [29, 43, 46, 103, 104]. Since we use an immersed boundary framework to do a one-way coupling of the cilia structural deformation to the fluid equations, and so we compare our simulation results with that of the closest immersed boundary method results in the literature to show consistency [49, 105].

The flow domain for comparison is 2-dimensional as described in the problem formulation with the following specific geometry: domain height and length is equal to 20 μm, cilia length is 10 μm, periodic boundary conditions in direction of cilium beating (inlet and outlet of the repeating domain), and no-slip boundary conditions on the top and bottom surfaces. In [105], the authors provide numerical simulation results of non-Newtonian behavior of cilia-driven fluid in both normal and diseased conditions, with the numerical simulation domain just described (square-like domain of infinitely repeating single cilium units). While our fluid is Newtonian and we are not recreating the non-Newtonian flow behavior we achieve a similar flow profile shown in Figure 2.11. We must note that the data is recreated by using an open-source data digitization program Engauge Digitizer Software [106]. Additionally, the differences in flow rates can be attributed to the elastic energy stored in the fluid from the non-Newtonian fluid model used in their work. The authors reported higher flow rates in their baseline configuration with a non-Newtonian model compared to the control case, which is most similar to our present test configuration.

It is difficult to compare numerical simulation results with quantitative experiments at

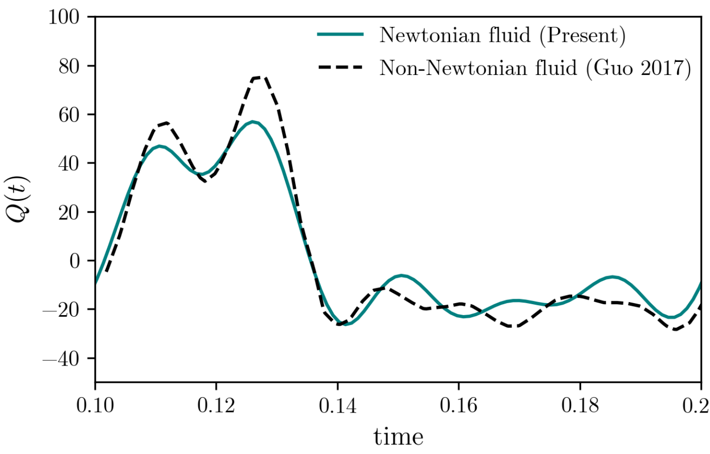

Figure 2.11: Comparison of published results from [105] in a square domain (H×W $= 20 \times 20\mu$m). Note: results are in dimensional values, converted from original non-dimensionalization

comparable configurations, but nevertheless, we surveyed the literature for transport rates induced by cilia, and some have been estimated for similar configurations. We have summarized some of the effective mucosal clearances rates in Table 1.1, with ranges in the low 40 μm/s to higher 200 μm/s. In the work by Ling et al. [24], human live tracheae were excised from deceased organ donors, but presented otherwise healthy lung tissues, and mucus transport was subsequently measured using seeded particles. The transport rates reported greatly varied between individuals, and thus the authors reported variation among a single sample for all the seeded particles. The transport ranges went as high as 100 μm/s, with an average of 54.9 μm/s ($\pm 12.3SD$). Older studies have reported similar ranges, from 39.2 to 50 μm/s [20, 70], and so the goal of our initial validation effort is to see if we can achieve a similar range for transport. In order to compare our results, we take the average flow rate for the test case across the $x = 0$ plane, and then integrate the flow rate during each period to attain the average flow rate per period. This steady-state average flow rate is plotted in Figure 2.12, which give us a transport rate range between 22.3 to 115.3 μm/s, falling squarely between reported rates in the literature.

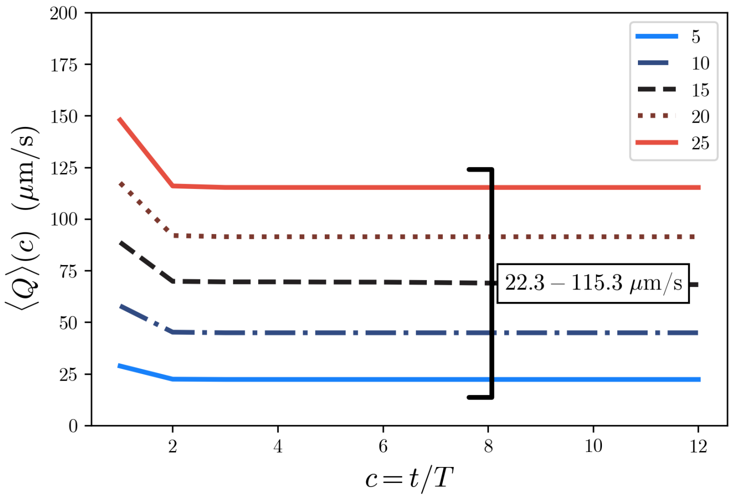

Figure 2.12: Average flow rate per cycle, giving a mean transport rate for the fluid (in μm/s). The flow rates presented are for varying frequencies. The indicated range shown by the bracket, corresponds to the calculated average flow rates per cycle for the lowest and highest frequencies.

Chapter 3

Finite-sized Particle Transport by a Single Cilium

3.1 Methodology

This chapter explores the interaction that finite-sized particles have with a single infinitely repeating cilium by exploring parameters that are not always possible to modify easily *in-vivo*. We use the immersed boundary method to capture the kinematic movement of beating cilia, and additionally use this framework to embed particles of various sizes with arbitrary shape in the fluid layer. However, we will only explore the differences between finite-sized circular particle and tracers, and will revisit particle shape differences in Chapter 5. First, we describe single cilium repeating unit, which is different than our previously describe model problem used for verification. Next, we describe our modeling framework for an embedded finite-sized particle, and the relevant assumptions. Then, we quantify the effects of each parameter we vary, and give the details of the particle dynamics we quantify. Finally, we close off this chapter by discussing our findings and motivating the more complex and interesting phenomena we explore in the rest of the dissertation.

3.1.1 Single Cilium Configuration

The biophysical parameter space we explore in our study is shown in Table 3.1, and it should be noted that the parameter space corresponds to realistic parameter ranges in hu-

parameter	symbol	baseline	range
frequency	f	10 hz	$5-25$ hz
domain length	l_d	40 μm	$16-80$ μm
periciliary height	h_p	20 μm	$20-40$ μm
cilia length	l_c	10 μm	$**$

Table 3.1: Study parameters used in this chapter. Ranges include the baseline value case. It should be noted that domain length corresponds to the total distance between cilium. **Cilia length is a fixed parameter in our study.

man tracheobronchial tree. In Table 1.1, we report some representative mucociliary escalator parameter ranges for individual subcomponents, such as cilia beat frequency or total mucosal layer height versus periciliary layer height. While the literature reported is not comprehensive, the values are illustrative of the wide range of values that may exist in a particular measurement. These wide parameter ranges motivate our selected parameter ranges for our parametric study shown in Table 3.1. Our problem definition remains the same as in Chapter 2, the only notable difference is that our parameter range for the geometric configuration changes the domain length and height previously described (see Figure 2.2 for the problem domain definition.)

3.1.2 Embedded Particles

The deposition of particles in the airways is affected by their size, morphology, and composition. In our numerical simulation framework, we can chose any particle of arbitrary shape and size and seed it the fluid domain. However, for these simulations we begin by simply comparing the trajectories of circular particles with that of tracers. As we will revisit in Chapter 5, the dynamics for particles with non-circular shapes can be much more complicated.

Our simulations are 2-dimensional and periodic along the x direction, implying that we seed multiple particles at the same location along the flow domain. However, at any particular time, only one particle exists in this periodic domain, indicating that our particles are separated by physical space equal to the domain size. Additionally, our simulation can

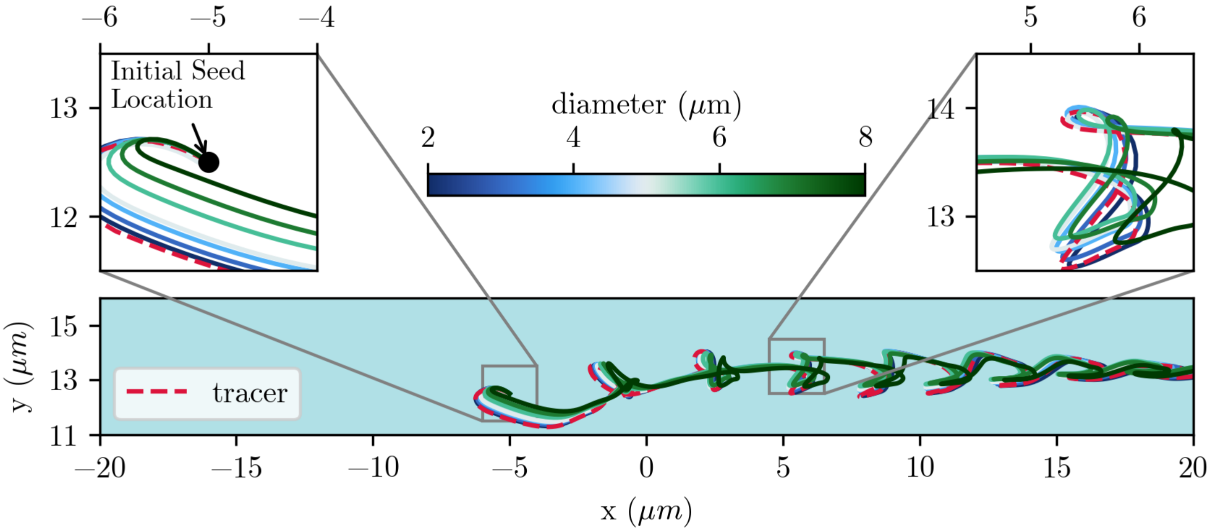

Figure 3.1: Particle trajectories for varying diameter, $D = 2, ..., 8$ μm, where the color bar corresponds to the line color. A tracer particle is shown as a red dashed line. The inset on the upper left depicts the seed location and differences in the initial particle trajectory. The inset on the upper right shows the complex trajectories for different particle sizes.

be viewed as a stack of infinitely close cilia in the direction normal to the flow domain. This implies that our particles are circular in *cross section*, and describe an infinite cylinder normal to this cross section. In Figure 3.1, we vary particle size to show the complexity that arises with particle trajectories. For this chapter, we focus on a particle that has size comparable to the cilium length, more specifically $D = h_c/2$, where h_c corresponds to the cilium height. This defines the particle of diameter 5μm, which corresponds to a particle designated as coarse particulate matter.

3.2 Results

In this section, we present various quantities that help describe the transport of fluid and particles in our model. We quantify the flow rate by taking the cross-sectional velocity and calculating the flow rate in the direction of ciliary beating (see Section 2.3). The cross sectional velocity here is defined as

$$u(x, y, t) \tag{3.1}$$

for values of $y = 0$, the base of the domain, to $y = h_p$, the top of the periciliary height. The cross sectional flow rate is then defined as

$$Q(x,t) = \int_0^{h_p} u(x,y,t)dy \tag{3.2}$$

where we have integrated the velocity normal to the direction of fluid motion along the periciliary layer height. For all calculations, we use the plane $x = 0$ to calculate the cross-sectional flow rate. Further, we average this quantity per period to attain a steady state value for the transport rate, namely we calculate

$$\langle Q \rangle = \frac{1}{T} \int_0^T Q(\tau)d\tau \tag{3.3}$$

where T is the length of one beat cycle. We note that the average flow rate per cycle is calculated at each period, $T_i = T_1, ..., T_c, ..., T_{\max}$ and for all our simulations, at steady state value has been achieved at $T_{\max}$.

Additionally, we also present some quantities for tracking the seeded particle motion. However, as we described in Section 1.4, finite inertial effects are introduced with a low finite Reynolds number from our 2-dimensional assumption. First, we define the Lagrangian position at the center of each particle as $s(x,y,t)$, and $s_k(x_k, y_k, t_k)$ denotes the discrete position of the particle at any time, $t_k = t_0, ..., t_N$, where the initial seed location is at time $t = 0$ and $k = 0$, and the final position is at $t = T_{\max}$ and $k = N$. We calculate the discrete arc-length, L, as

$$L = \int_{s_0}^{s(x,y,t)} \mathrm{d}s \approx \sum_{k=1}^{N} \Delta s_k = \sum_{k=1}^{N} \sqrt{(\Delta x_k)^2 + (\Delta y_k)^2} \tag{3.4}$$

where $\Delta x_k = x_k - x_{k-1}$ and $\Delta y_k = y_k - y_{k-1}$, and the net-displacement in the x-direction

$$\Delta L = x_0 - x_{\max} \tag{3.5}$$

We note that for all our calculations, frequency inherently changes the time scale, and the Reynold's number. We present results for constant Reynolds number and compare the results at a *per cycle* rate. Obviously, if we were to integrate per unit of time, instead of per beat cycle, the results would point to faster transport by faster beating cilia. Nonetheless, when considering these results, the reader is encouraged to interpret change in a quantity over the same *number of periods* elapsed, and not the same *length of time* elapsed.

3.2.1 Cilia-driven fluid motion

To gain some preliminary insight into the flow dynamics in the periciliary layer, the quantities described above were calculated, namely, flow rate over time and average flow rate per cycle. In quantifying the flow rate, we see a few interesting results. In Figures 3.2-3.4, we show the effects that each parameter has on flow rate in one beat cycle, and also report the flow rate at the 10th beat period, as by then any initial transient has leveled off. Additionally, these Figures also include the corresponding average flow rate per cycle. Of interest is the trend the beat frequency has on the magnitude of fluid transport. Specifically, the frequency increased the peak flow rate by 5.1 fold (Figure 3.2a). We then consider changes in the height of the periciliary layer which shows a smaller increase in the peak flow rate (Figure 3.3a). However, as indicated by the blue shaded area, there is less flow reversal globally. This is is highlighted by Figure 3.3b, where we see that a height of 40 μm corresponds to a larger net transport. Finally, when considering domain length, we see a increase in the average flow rate per cycle, and in Figure 3.4a, we see a sharp increase as cilium inter-spacing decreases.

3.2.2 Transport of Finite-Sized Particles

In this section, we compare a single finite-sized circular particle that is transported by the beating cilium to that of a passive tracer particle. In Figure 3.5, several typical trajectories are shown, where we plot the circular particle path in green and the trajectory of a tracer particle in black. It is important to note two features of these trajectories 1) both the finite

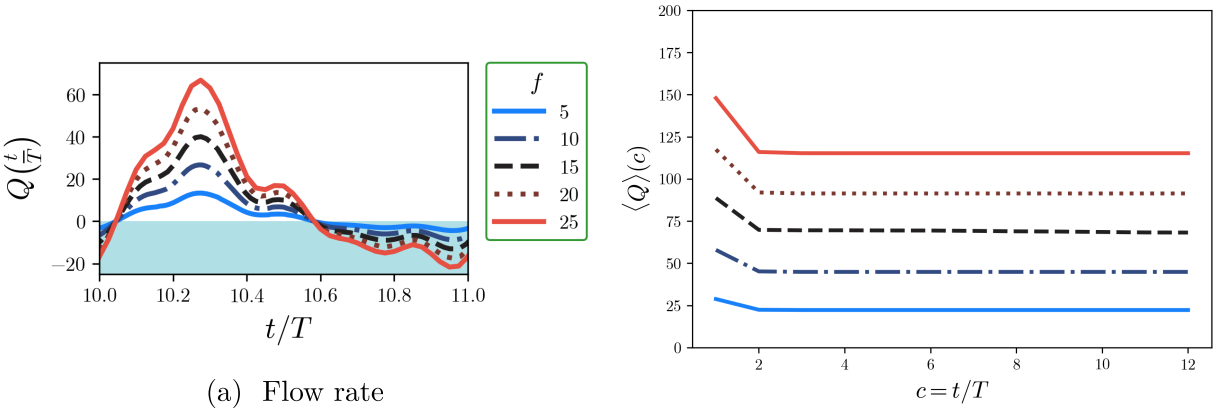

(a) Flow rate

(b) Average flow rate per cycle

Figure 3.2: The flow rate changes in response increasing frequency for a single cilium. In Figure 3.2a, we plot the flow rate in one cycle and in Figure 3.2b we plot the average flow rate per cycle for the entire simulation time.

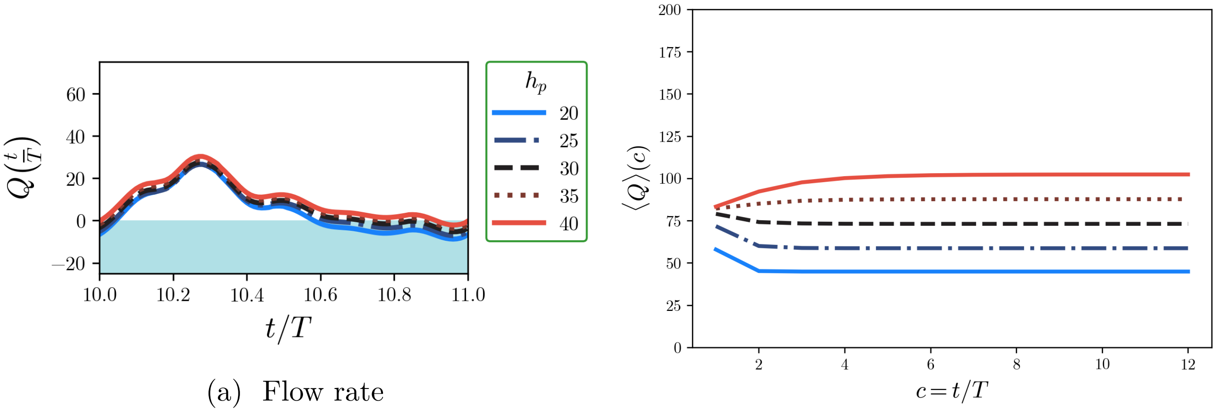

(a) Flow rate

(b) Average flow rate per cycle

Figure 3.3: The flow rate changes in response increasing periciliary height for a single cilium. In Figure 3.3a, we plot the flow rate in one cycle and in Figure 3.3b we plot the average flow rate per cycle for the entire simulation time.

sized particle and tracer particles follow a qualitatively similar trajectories for all cases; and 2) minor modifications from the baseline case change significantly the overall trajectory shape of the particles.

In order to quantify the differences between these two trajectories (the finite sized particle and the infinitely small tracer particle), we track the particle trajectory and the tracer particle and measure the arc length of the distance traveled by evaluating Equation 3.4. We must

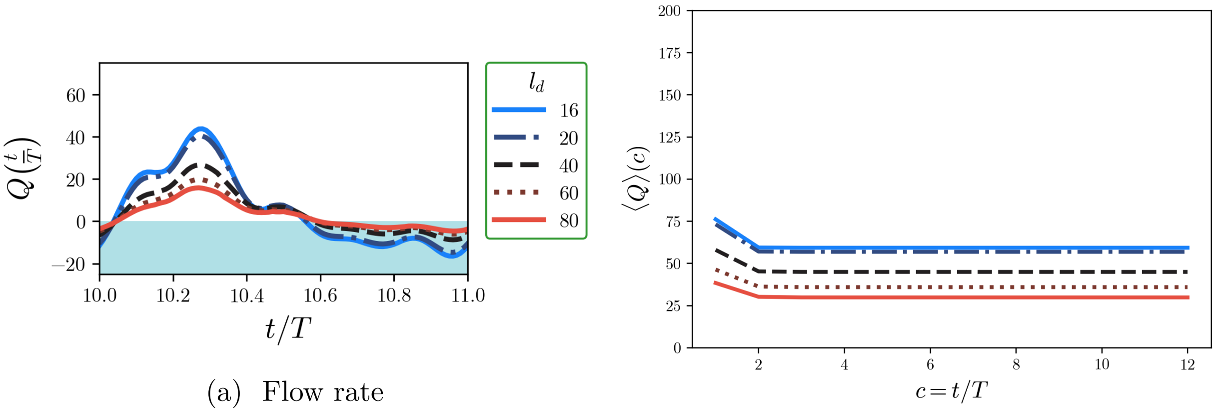

(a) Flow rate

(b) Average flow rate per cycle

Figure 3.4: The flow rate changes in response increasing domain length for a single cilium. In Figure 3.4a, we plot the flow rate in one cycle and in Figure 3.4b we plot the average flow rate per cycle for the entire simulation time.

note that both particles are seeded in the same location and are tracked in two separate simulations. Our findings show that, overall, a finite-sized particle travels less distance when compared to a tracer particle, which is shown in Figure 3.6. Additionally, we see that the differences between a tracer particle and a finite-sized particle are not always constant, as is indicated by the differences in 3.6c, where a smaller domain indicated less of a difference and a larger domain indicated a larger difference.

When considering each parameter individually, we see that while frequency did increase fluid pumping (Figure 3.2a), the actual trajectory for each particle remained essentially unchanged (Figure 3.6a). As the periciliary height was varied, we see an increase in particle trajectory with increasing periciliary height, which appears to asymptote (Figure 3.6b), but additional larger periciliary height simulations must be computed to confirm this. The domain length shows interesting behavior, as closer cilia transport particles very similar lengths, while the stratification is still present at larger separation distances (Figure 3.6c). Additionally, there seems to be a local minimum when considering the length of the domain. This is attributed to differences in the particle paths shown in Figure 3.5. When looking at the baseline configuration where the domain length $l_d = 40$ μm (Fig. 3.5a), we see a less stretched path compared to an increase in length, $l_d = 60$ μm (Fig. 3.5c).

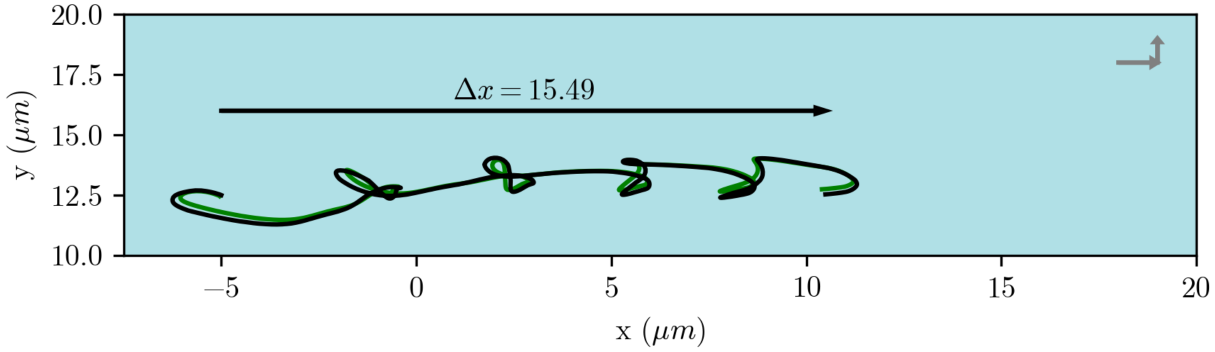

(a) Baseline parameters: f=10 hz; $h_p = 20$ μm; $l_d = 40$ μm

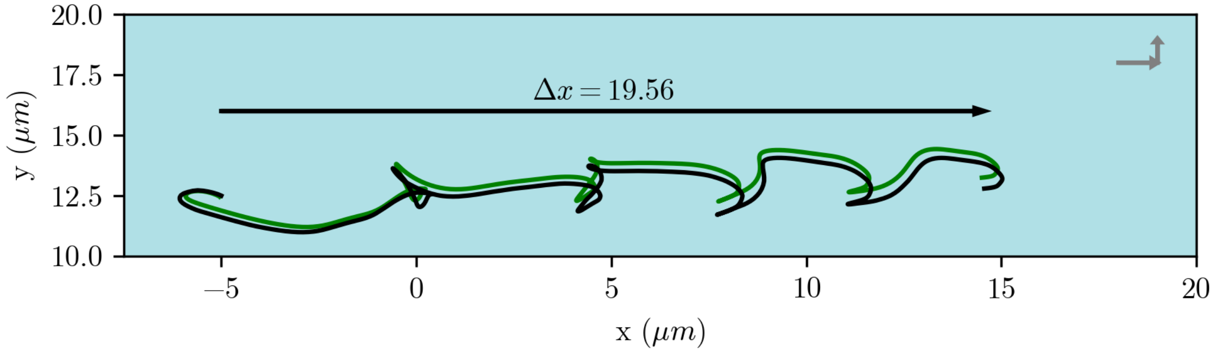

(b) Height variation study parameters: $f = 10$ hz; $h_p = 25$ μm; $l_d = 40$ μm

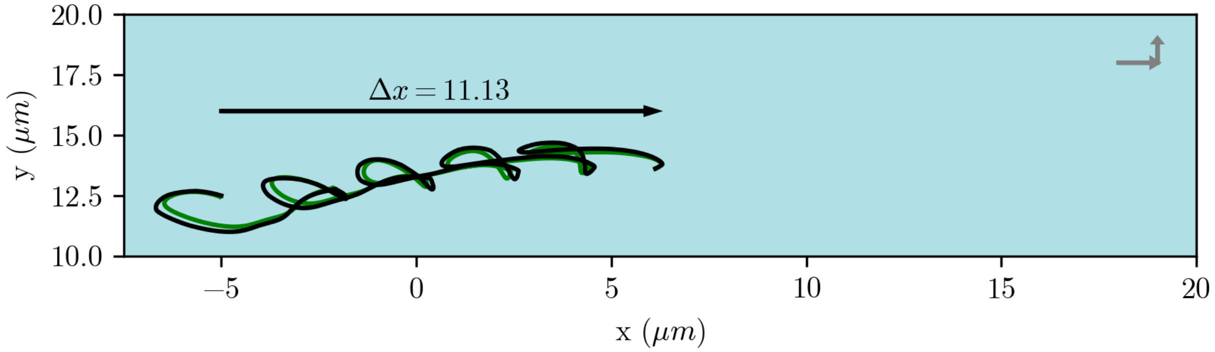

(c) Length variation study parameters: $f = 10$ hz; $h_p = 20$ μm; $l_d = 60$ μm

Figure 3.5: Trajectory comparisons between tracer (solid black line) and circular particle (green line). All seed locations are the same $x = 5$ μm and $y = 12.5$ μm; top panel is the baseline configuration, while the middle panel shows changes in periciliary height, and the bottom panel shows changes in domain length. Note that the x and y axes are not equal, and the unit vectors are shown in the top right corner as grey arrows.

However, although particles are tumbling through the domain as the beating cilium drives fluid through the channel, it is important to note that the final and initial positions

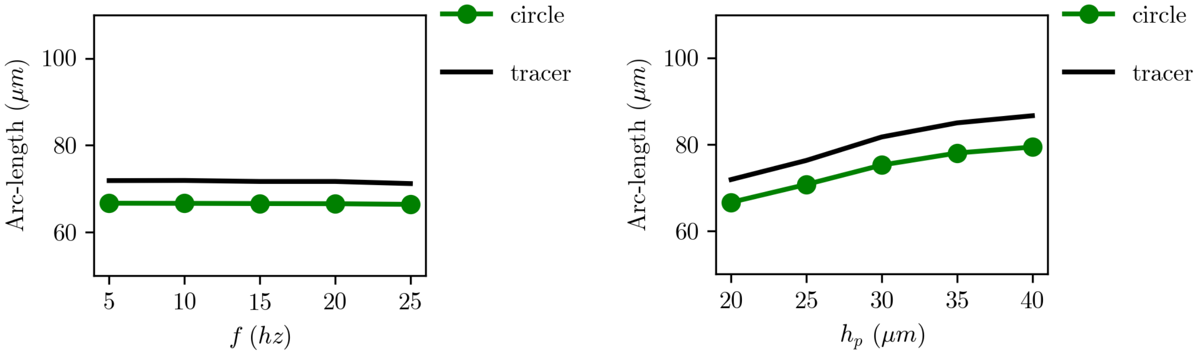

(a) Total arc-length trajectory for frequency range $f = 5 - 25$ hz

(b) Total arc-length trajectory for periciliary height range $h_p = 20 - 40$ μm

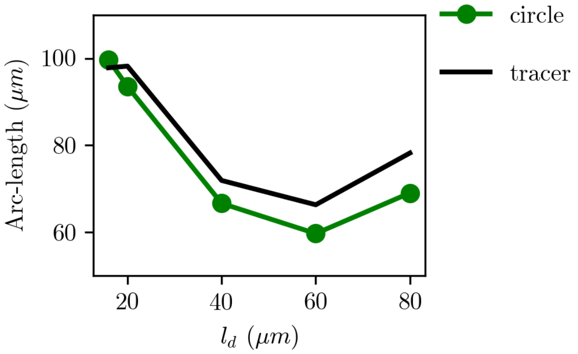

(c) Total arc-length trajectory for domain length range $l_d = 16 - 80$ μm

Figure 3.6: Total arc-length trajectory comparisons between an embedded circular particle and tracer for each parameter that is varied.

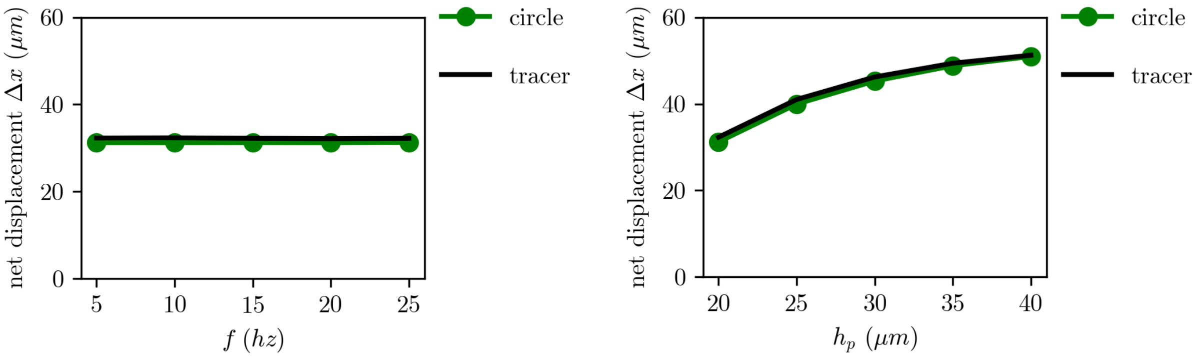

(a) Net displacement along the $x-$direction for frequency range $f = 5 - 25$ hz

(b) Net displacement along the $x-$direction for periciliary height range $h_p = 20 - 40$ μm

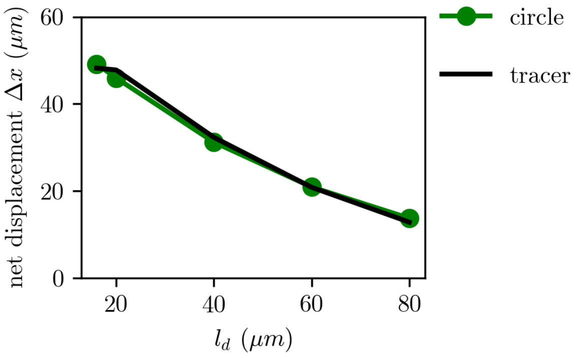

(c) Net displacement along the $x-$direction for domain length range $l_d = 16 - 80$ μm

Figure 3.7: Total net displacements comparisons between an embedded circular particle and tracer for each parameter that is varied.

of particle dictate how much remains in the system. We then calculate the net displacement for each individual particle. While the trends remain relatively unchanged, we see in Figure 3.7 that the finite sized particles and tracers are equally transported, as all curves collapse onto one curve. The effect of frequency remains unchanged, as increased beat frequency does not increase net displacement over one period (Fig. 3.7a). The same effect is seen with periciliary height, similar trend as before, with a higher periciliary height indicating increased transport. Finally, we see that for an increased domain length, the local minimum does not exist, implying that regardless of the increased tumbling seen before, net transport is still reduced with longer domain lengths.

3.3 Discussion and Conclusions

The interaction of finite-sized particles in the upper airways is important for two reasons: 1) clinical applications of targeted drug delivery can aid in therapeutic effects for patients and 2) inhalation of toxic chemicals are adverse during acute exposures and even more harmful for diseased individuals. However, once deposited, these particles interact with the mucosal layer, albeit at small scales, and most research usually focuses on the inhalation and transport of *bulk* particle deposition. Additionally, most of the experimental validation used by researchers that model the mucosal clearance process require several of the imaging techniques, with particle tracing being used as prominent feature. Further, whole body exposure of particles as a validation for inhaled particle deposition models would require careful imaging of *in-vivo* subjects. This impressive multidisciplinary effort by countless researchers continues to expand. However, there are still gaps in the knowledge that require continued collaboration.

This work has shown, to our knowledge, the first attempt at modeling finite size particle-cilia interaction, where a single cilium transported the lubricant periciliary layer embedded with finite-sized and shaped particles. Our model systematically varied important biophysical parameters inherent to basic understanding of the clearance mechanism in the human airways. We assessed the performance of the single cilium by varying the beat frequency, periciliary layer height, and domain length. In this chapter, we compared the effects that each parameter had on fluid pumping, particle trajectory and displacement, and fluid layer mixing.

The results of simulation show a striking efficiency of the prescribed cilia beat shape in clearance of particles, as net particle displacement between a finite sized particle and tracer particles do not have a major difference. However, when considering the actual particle trajectory shapes (Fig. 3.5, via the measure of arc-length trajectory Fig. 3.6), we paint a complex picture of particle traveling. The trajectories are twisting and folding, and for certain parameters, the trajectory forms circular arcs repeating in time. Additionally, we show that tracer particles and finite-size particles have the same net displacement, however, their arc-length trajectory do vary, implicating the role of small finite inertia on transport. Of course, we must remark that our simulations are a single repeating unit and we are not feeding hydrodynamic feedback to the cilia beat shape, as other researchers have done in previous works ([54, 107]). But nonetheless, this research gives valuable insight into the interaction of finite-sized particles with that of the single cilium unit.

The simulation domain assumes that both the top and bottom layers are no-slip boundaries, and while the *in-vivo* system includes a dual mucus-periciliary layer, we are investigating the sub-mucosal periciliary only, which in the context of acute respiratory distress syndrome is a valid assumption. Increased fluid volumes on the luminal side of the trachea would reduce the clearance of mucus, and thereby the cilia would beat in the periciliary layer only. While a case could be made that less rigid interface between the mucus and periciliary exists, we believe our work shows the limit as the mucus layer becomes immovable and stagnant, while the periciliary layer continue to flow. Additionally, our work elucidates how particle transport occurs in the layer between the cell wall and the mucus layer, with particles continuing to traverse even in the absence of patches.

An important assumption that has been made with our work is the repeating single cilium unit. While this assumption was made to simplify the model, it is an appropriate constraint in order to set up a correct baseline configuration for simulations of cilia-particle interaction. A majority of other works tends to begin with exploration of the cooperative nature of adjacent cilia, and the emergence of metachronism. We note that while our assumption ignores the metachronal behavior, our simulation work still provides insight into particle movement when cilia are performing without metachronism. Future work showed undoubtedly allow for varying the cooperative nature of multiple cilia and how these parameters influence particle clearance. Additionally, no interaction model has been implemented with several particles or for direct cilia-particle-wall interaction. This is left for future work as the focus of this chapter was the implementation of finite-sized particles in the periciliary layer and that of the cilia driven fluid, however, it would be a value area of exploration to study.

Chapter 4

Cilia patch fraction and optimal particle clearance

4.1 Methodology

In the previous chapter, we've developed a baseline and simplified configuration for cilia-particle interaction and the transport of fluid in the periciliary layer. This chapter expands this model and explores the interaction that finite-sized particles have with a single infinitely repeating cilium *patch* by creating a more accurate description of the cilium configuration. We modify our problem configuration by making full use of the description of a cilia metachronal wave provided by Fulford and Blake [34]. First, we critically evaluate the authors' original description of a cilium patch, the definition provided of the metachronal wave, and the dependence on configuration parameters. Next, we describe our configuration single cilium patch repeating unit. Then, we quantify the effects of each parameter we vary, and give the details of the particle dynamics we quantify. Finally, we close off this chapter by discussing our findings as they pertain to the expanded definition of cilium patches.

4.1.1 Cilium Patch Fraction

In order to recreate a more realistic model of the upper airway, we set out to recreate patches of cilia similar to the *in-vivo* conditions. This requires us to get an accurate picture of some acceptable baseline parameters for the geometry of a single cilium, shape and frequency of the beat, and some mucosal layer properties. We refer to the parameter ranges in Chapter 2, Table 1.1 to note the variety in mucosal layer structure from extensive experimental measures. As we have done before, we set the cilia beat frequency and shape kinematics, $\vec{\xi}$, using one of the original beat patterns from Fulford and Blake [34]. In this seminal work, the cilia shape is recreated from high-speed images to form a Fourier series recreation of the beat shape kinematics:

$$\vec{\xi}(s,t) = \frac{1}{2}\vec{a}_0(s) + \sum_{n=1}^{N_0} \Big(\vec{a}_n(s)\cos(\sigma t) + \vec{b}_n(s)\sin(\sigma t) \Big) \tag{4.1}$$

This shape kinematics is widely used, and has been the basis for several studies that explore metachronism, ciliary fluid pumping, and fluid mixing. In the original paper, Fulford and Blake set out to not only study a single cilium, but also the effects of the the wave form arising from densely packed cilia. The beat shape is assumed as planar, beating only in the x_1 and x_3 plane, whereas the actual beat experienced in the lung epithelium can very well be 3-dimensional. They modeled the cilia patch as a doubly periodic 3-dimensional domain, with equal spacing between neighboring cilia:

$$\vec{\xi}^*(s,t) = (na\hat{i} + mb\hat{j}) + \vec{\xi}(s,\tau) \tag{4.2}$$

$$\tau = kna + \sigma t \tag{4.3}$$

Ultimately, this description of an infinite densely packed array can be described with 1 temporal parameter, beat frequency $f = \sigma/2\pi$, and 2 spatial parameters, wavelength, $\lambda = 2\pi/k$, and spacing, a and b along the the x_1 and x_2 directions respectively. Since it is not always possible to have such control in parameters with *in-vitro* experiments, most modeling efforts have allowed variation of both spatial and temporal configurations of doubly periodic domains, focusing on arrays of cilia that are infinite.

In our numerical modeling work, we seek to explore the effects that patches of cilia have on fluid and particle transport. Since the variation in coverage of cilia in the upper airways can range from 60% in the upper airways to 20% in the lower airways, we defined the parameter *cilium patch density*, ρ_c, as a non-dimensional area coverage fraction (Eqn. 4.4).

$$\rho_c = A_{\text{patch}}/A_{\text{ref}} = nA_{\text{c}}/A_{\text{ref}} \tag{4.4}$$

We assume a single cilium patch area of $A_{\text{c}} = ab$ which specifies the distance between two neighboring cilia in a single patch, and thus the total patch area, A_{patch}, is the number of cilia in a patch, n, multiplied by the single cilium patch area, A_c. The reference area, A_{ref}, corresponds to the specific area in the tracheobronchial tree that we are investigating, and can include a single cell or multiple cells. An illustration of this is shown in 4.1a, where we show a random arrangement that is closer to *in-vivo* conditions than is usually modeled. In Figure 4.1b (not drawn to scale), we show the model configuration in 3-dimensions, and in Figure 4.1c we show the 2-dimensional equivalent for our numerical model.

As shown in Figure 4.1c, the arrangement for our numerical model, however, is not truly random, but a repeating 2-dimensional domain, with a fixed number of cilia in a patch that neighbor another patch. In order to narrow down the simulation parameters, we first look at the shape described by Equation 4.2. In the airways, the cilia beat is 3-dimensional and experimental results have shown that the beat shape is mostly planar in nature ([18, 108]), and Equation 4.2 assumes only a planar beat shape. However, the challenging nature of imaging this perfectly, and being able to conclude that hydrodynamic interactions do not influence the neighboring cilia planar beat is still being investigated. Thus several authors using numerical simulation have dealt with this limitation of planar beating in different ways. Ding et al. used the same beat shape from Fulford and Blake and set the distance between cilia large enough to prevent overlapping. Chateau et al. included a hydrodynamic couple parameter to describe their beat shape and verified that in their numerical simulations that overlapping Lagrange points did not contribute to the velocity field significantly. In our simulations, since we are reducing our model to a 2-dimensional domain, we take a different approach, we define the acceptable distance between neighboring cilia that still allows us to

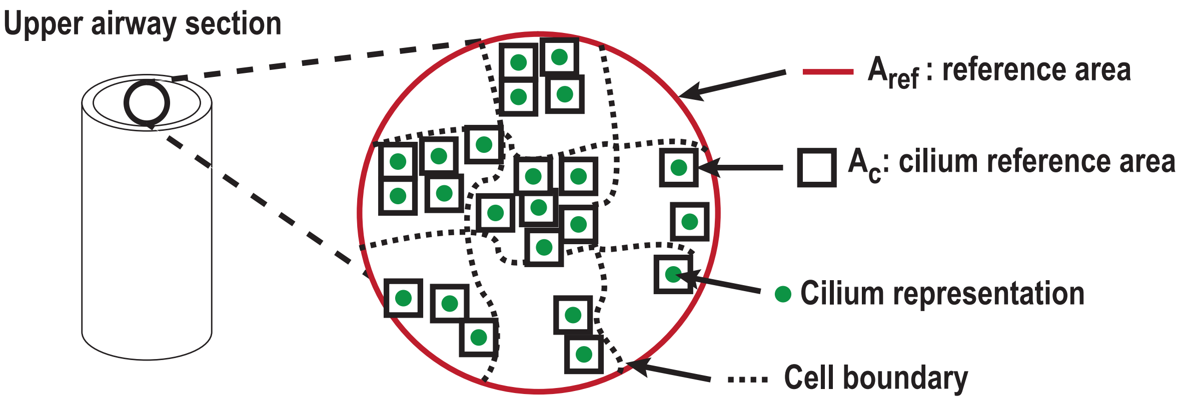

(a) Sketch of a representative area from the luminal side of the upper airway. The reference area, A_{ref}, is represented by the red solid-line boundary. Individual cilium reference areas, A_c, are represented by black solid square boxes. The base of the cilium is indicated by a solid green dot. Inter-cellular boundaries are denoted by a fine dotted line. Note: not drawn to scale.

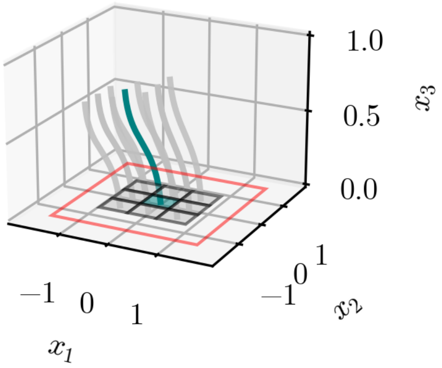

(b) 3-dimensional representation of the cilium patch fraction.

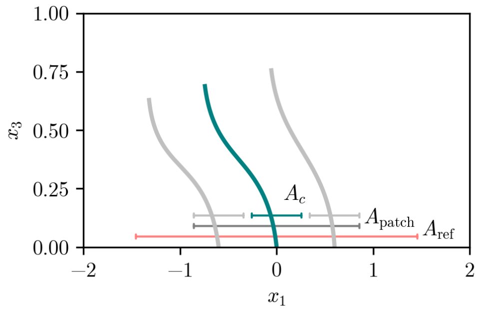

(c) 2-dimensional representation of the cilium patch fraction.

Figure 4.1: The arrangement for the original model from Fulford and Blake [34] is organized regularly in the x_1 and x_2 directions, with cilia extending out in the x_3 direction, and beating in the $x_1 \perp x_3$ plane (Figure 4.1b). In our simulations, we have the 2-dimensional equivalent shown in Figure 4.1c.

make modification to the spatial arrangement via the wavelength and spacing (λ, a).

In Figure 4.2a, we plot the dependence between wavelength and neighboring cilia spatial phase (in non-dimension units). The original parameters used by Fulford and Blake are shown in the dashed grey line, with the red square indicating their baseline wavelength of 30 μm with 100 cilia per wavelength and spacing of 0.3 μm. It must be noted that we have converted their values to non-dimensional units using their baseline cilium length of 6 μm, thus the grey dashed line is equal to a spacing of 0.05 and a wavelength of 5. Now, we find the maximum wavelength allowed and corresponding phase between neighboring cilia without overlapping. That is to say, for a cilium of radius 0.1 μm, we do not allow for the phase to become large enough such that the any point on a cilium overlaps an adjacent cilium's radius at any point along the centerline. As we vary cilia spacing, we find this maximum wavelength, which are plotted as grey open circles in Figure 4.2a. Additionally, in Figure 4.2b and 4.2c, we show two samples of overlapping cilia that may occur, and are highlighted in 4.2a with arrows corresponding to the spacing and wavelength combination of $a = 1.00,\ \lambda = 2.4$ and $a = 0.20,\ \lambda = 19.1$. With these limits on neighboring cilia overlapping to our spatial orientation, we set our baseline values for our initial run as $a = 0.3,\ \lambda = 20$, or equal to a inter-cilium spacing of 3 μm and a wavelength of 200 μm.

4.1.2 Patch Configuration

We complete our problem definition by incorporating the cilium patch density, periciliary height, and metachronal wavelength variation to our parameter ranges. In Figure 4.3, we show all spatial parameters, and note that we use the inter-cilium spacing, l_c, as the reference cilium area per unit length. Our reference patch area, A_{ref}, is similarly defined by the domain length, l_d, which corresponds to a reference patch area per unit length. Additionally, for our simulations, we fix the number of cilia in a single domain as $n = 5$. With these 3 parameters, we can control the cilium patch density by variation of the reference area $A_{\text{ref}} = l_d$ or neighboring cilia spacing, $A_c = l_c$. Thus, ρ_c varies from 0.10-0.75 and 0.25-0.50

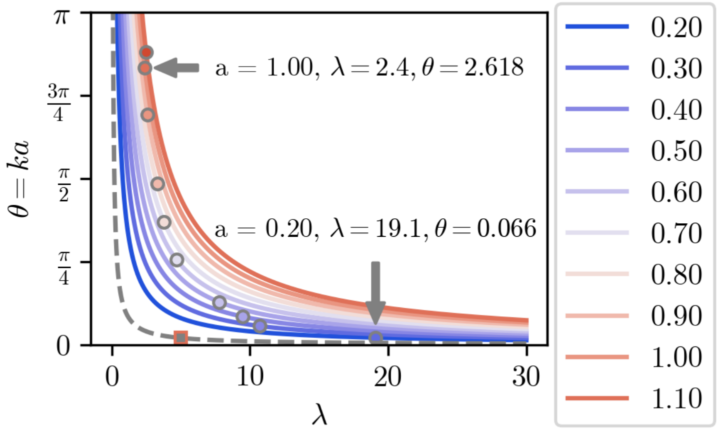

(a) Functional dependence of neighboring cilia phase on metachronal wavelength ($\theta(\lambda)$, for a variety of inter-cilium spacing a. Open grey circles indicate the minimum wavelength for a specific spacing that does not allow overlapping

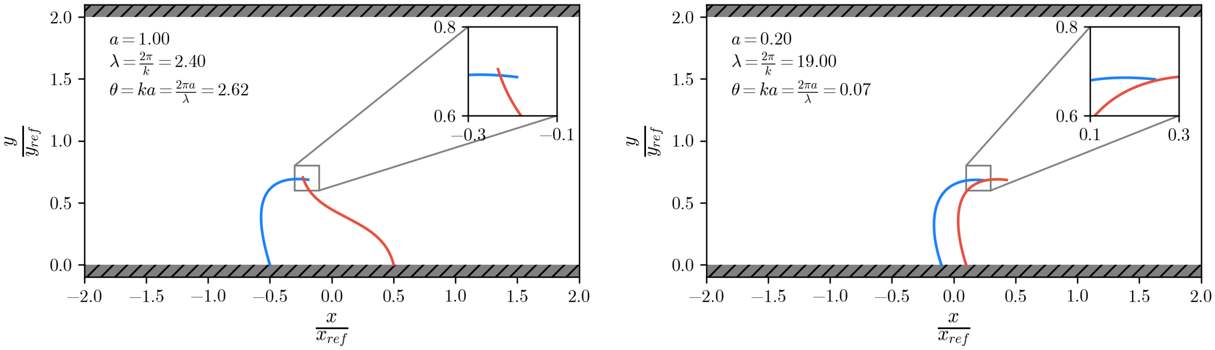

(b) Two neighboring cilia that overlap with a high phase difference ($\theta = 2.62$), but small metachronal wavelength ($\lambda = 2.4$). Cilium spacing, a=1.00

(c) Two neighboring cilia that overlap with a high phase difference ($\theta = 0.07$), but small metachronal wavelength ($\lambda = 19$). Cilium spacing, a=1.00

Figure 4.2: As wavelength increases, the neighboring cilia phase approaches zero, implying cilia beating all in sync. Conversely, the smaller the wavelength, the more out of phase neighboring cilia beat

Baseline Parameter	Symbol	Value	Variable Parameter	Symbol	Range [Baseline*]
Frequency	f	10 (hz)	Cilia Spacing	l_c	1-6 (μm) [3]
Periciliary Height	h_p	20 (μm)	→ Patch Fraction	ρ_c	0.125-0.75
Wavelength	λ	200 (μm)	Reference Area	A_{ref}	30-60 (μm) [40]
Number of Cilia	n_c	5	→ Patch Fraction	ρ_c	0.5-0.25

Table 4.1: Parameter space for numerical model configuration. *Fixed baseline parameter value shown in brackets [·]

parameter	symbol	baseline	range
frequency	f	10 hz	$5 - 25$ hz
periciliary height	h_p	20 μm	$20 - 40$ μm
wavelength	λ	200 μm	$200 - 1000$ μm

Table 4.2: Study parameters used in this paper. Ranges include the baseline value case. It should be noted that domain length corresponds to the total distance between cilium. **Cilia length is a fixed parameter in our study.

when varying l_c and l_d respectively. In Table 4.1, we summarize the baseline configuration and the variation of cilium patch fraction. We also conduct additional simulations when varying the frequency, periciliary height, and wavelength. Those parameter ranges are shown in Table 4.2.

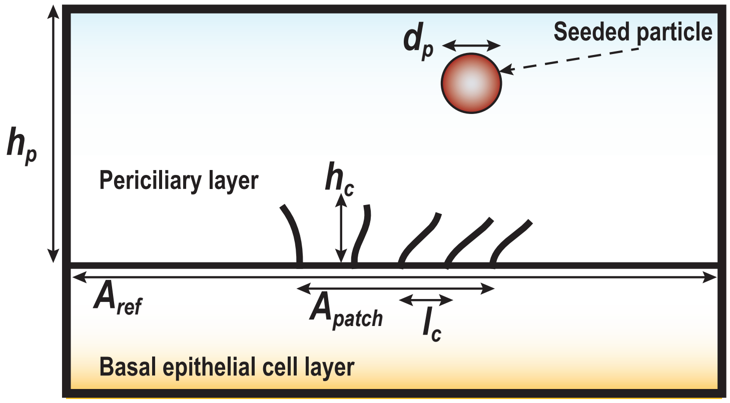

Figure 4.3: Sketch of the cilium patch model domain. Geometric parameters are the periciliary height, h_p, reference area per unit length, $A_{\text{ref}} = l_d$, and inter-cilium spacing, l_c. The seeded particle diameter is d_p, and the cilium height is h_c. Not drawn to scale.

The numerical simulation framework allows us to specify the kinematics of the beat shape, and each cilium can be independent from each other. However, for the purposes our this dissertation, we keep all cilia temporal frequencies equal. It would be trivial in our framework to consider *rogue* cilia into a patch, and see the effects of one or more cilia that are beating counter to the rest of the patch.

4.2 Results

In this section, we present similar metrics as provided in Chapter 3, Section 3.2, but focus on the cooperative nature of a cilium patch as opposed to the individual cilium. In particular, we aim to show that cilia patch fraction has a non-trivial effect on the transport rate and particle clearance.

4.2.1 Cilia-driven fluid Motion

We begin by returning to our analysis of cilia beat frequency, and once again, we show that there is a marked increase in flow transport at higher beat frequencies. The flow rate is increased approximately 5 times from the lowest beat frequency value to the highest ($\approx$ 22-112 μm^2/s), which is plotted in Figure 4.4a. We see that our flow rate per cycle falls within the ranges reported from experimental results that we summarized in Table 1.1.

Next we analyze the difference that increasing periciliary height had on the bulk flow. Specifically, we find similar trends to that in the single cilium case, in that increasing the periciliary height increased average flow rate per cycle, but not necessarily the magnitude of the *flow rate*. In Figure 4.5a, we see that the magnitude of the flow rate only changes from $\approx$ 45.1-to 51.3 μm^2/s which is a very modest increase. However, as we noted in the single cilium case, the flow reversal zone, which is indicated by the blue shaded area in the graph, was reduced. The true result of such little flow reversal is shown in Figure 4.5b, which indicates a much higher flow transport. In what amounts to a 12% increase in the maximum flow rate in the flow domain, less flow reversal per period doubles the average flow rate per cycle (increase $\approx$ 73-175μm/s).

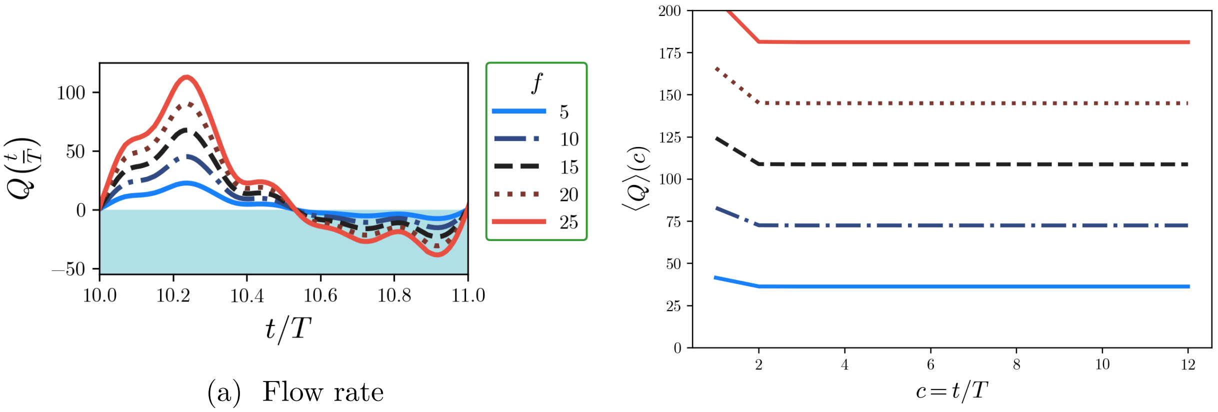

(a) Flow rate

(b) Flow rate per cycle

Figure 4.4: The flow rate changes in response increasing frequency for an cilium patch. In Figure 4.4a, we plot the flow rate in one cycle and in Figure 4.4b we plot the average flow rate per cycle for the entire simulation time.

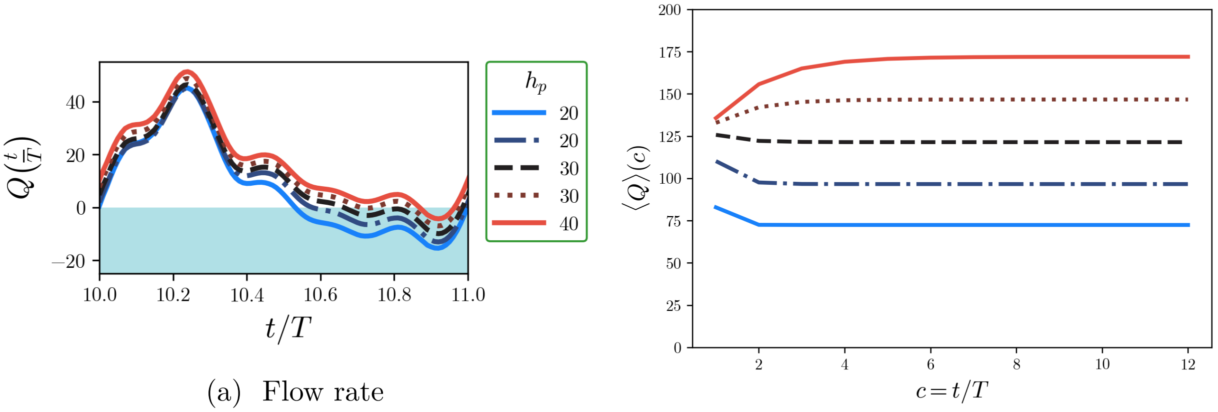

(a) Flow rate

(b) Flow rate per cycle

Figure 4.5: The flow rate changes in response increasing periciliary height h_p for an cilium patch. In Figure 4.5a, we plot the flow rate in one cycle and in Figure 4.5b we plot the average flow rate per cycle for the entire simulation time.

We now turn our attention to the cooperative nature of the cilium patch and focus on the parameters that affect the definition of the cilium patch. For our configuration, inter-cilium spacing (l_c), domain length (l_d), and wavelength (λ) are all parameters that when considered together affect a neighboring cilium's (or patch) phase lag (i.e. the phase lag between neighboring cilia on a single patch, or neighboring metachronal phase lag between patches). In our case, we focus on a single patch that is infinitely repeating, thus there is no phase lag between neighboring patches. However, we do incorporate neighboring cilia phase lag via modifications to the wavelength.

We begin by analyzing the wavelength and its effect on flow transport. As a reminder, for our 2-dimensional simulation, we picked the lowest wavelength that could still capture all the cilium inter-spacing considered while still making sure that none of the cilia overlapped. In other works [49, 109], spacing was increased to ignore this issue, and the focus of those studies were in precisely changing the phase lag in the full range from completely synchronous ($\lambda \to \infty$) to completely out of phase ($\lambda \to 0$). Nonetheless, in Figure 4.6, we see that indeed increasing the metachronal wavelength (or equivalently making all cilia beat in synchrony), reduces the flow rate and average flow rate per cycle. Conversely, if there is a decrease in the metachronal wavelength, we see a non-linear increase in the average flow rate per cycle. This is in line with what was found in the work by Ding et al. [109]. Additionally, we must note that increasing the wavelength is analogous to reaching a single infinitely repeating cilium unit, as was simulated in Chapter 3 albeit one would be required to match the inter-cilium spacing and make the total domain length equivalent as well.

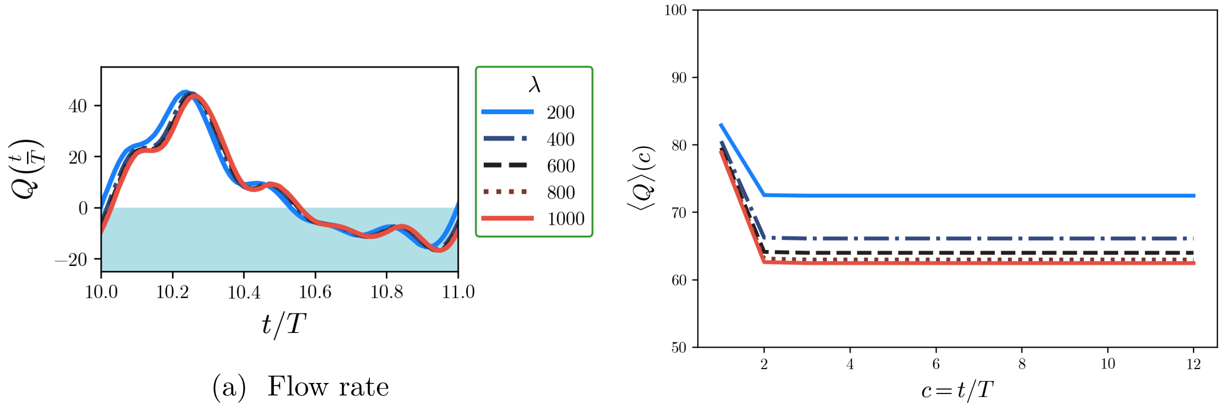

(a) Flow rate

(b) Flow rate per cycle

Figure 4.6: The flow rate changes in response increasing wavelength λ for an cilium patch. In Figure 4.6a, we plot the flow rate in one cycle and in Figure 4.6b we plot the average flow rate per cycle for the entire simulation time.

Finally, we report the results from analysis of the parameters that govern our definition of cilium patch fraction, namely domain length (l_d) and cilium spacing (l_c). In Figure 4.7a, we see that decreasing the length of the domain increases the flow rate, while increasing the domain length results in a decrease in the flow rate. The effect of decreasing the domain is evident from our definition of cilium patch density, which is inversely proportional to the domain length, $\rho_c \sim \frac{1}{l_d}$. Next, we analyze the effect that increasing the inter-cilium spacing has on the flow transport. In Figure 4.8a, we see a departure from previous graphs of flow rate, whereby the increased phase lag between cilia due to the wavelength dependence on spacing change the functional form. Additionally, we see a non-monotonic behavior in the average flow rate per cycle (Figure 4.8b). An increase in the inter-cilium spacing indicates an increase in the cilium patch density, and for the first time here we see that there is a local optimum. The highest flow rate is produced by a spacing of 5μm, whereas the lowest flow rate is produced by a tightly packed cilium patch (admittingly also at a low cilium patch density). We recall that in our problem definition, that both cilium spacing and wavelength control the cooperative nature of neighboring cilia in a single patch. In this case, we have kept the metachronal wavelength constant as we increase the spacing. This, however, has the consequence of increasing the phase between cilia above the baseline case. When performing the same simulations when varying the cilium spacing, but this time keeping the phase constant (stretching out the cilium thereby increasing the metachronal wavelength), we see an almost identical result (not shown).

To summarize our results when quantifying the flow transport in response to the various parameters, we find that frequency continues to be the most impactful when considering an increase or decrease to flow parameters. However, decoupling the effects of certain cilium patch configuration parameters can be more troublesome as they are not completely independent from one another. Importantly, we see that periciliary height contributes extensively to the amount of flow reversal, a topic of great interest when considering inter-cilium phase. These parametric studies motivate our more detailed analysis of single tracer and finite-sized circular particles in the next section.

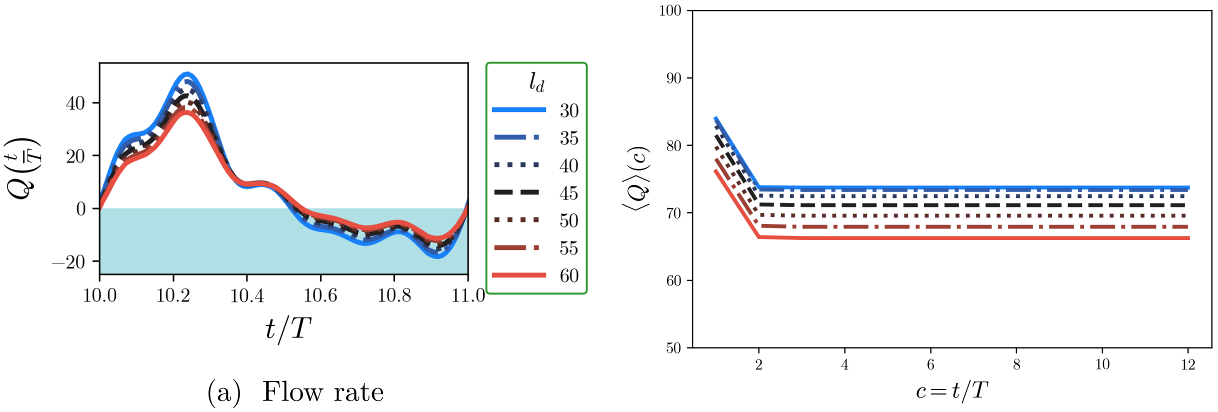

(a) Flow rate

(b) Flow rate per cycle

Figure 4.7: The flow rate changes in response increasing domain length l_d for an cilium patch. In Figure 4.7a, we plot the flow rate in one cycle and in Figure 4.7b we plot the average flow rate per cycle for the entire simulation time.

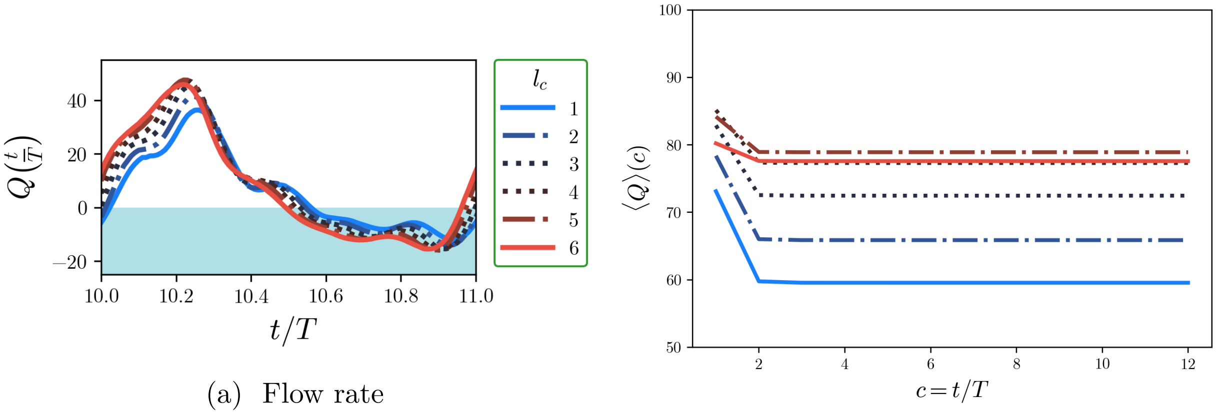

(a) Flow rate

(b) Flow rate per cycle

Figure 4.8: The flow rate changes in response increasing inter-cilium spacing l_c for an cilium patch. In Figure 4.8a, we plot the flow rate in one cycle and in Figure 4.8b we plot the average flow rate per cycle for the entire simulation time.

4.2.2 Finite-sized Particle Transport

As we have seen in Chapter 3, bulk flow parameters do not always correlate to increased particle transport. Thus in this section, we continue our quantification of particle-cilium interaction by tracking the quantities defined in Section 3.2, arc-length trajectory and net particle displacement. We begin our discussion by framing a simple comparison between the two baseline configurations of our single cilium and single patch models. In Figure 4.9, we plot the trajectories of finite-sized particle and of a tracer particle. The top panel corresponds to the single cilium while the bottom panel corresponds to the single cilium patch, but both are at the same baseline configurations (domain length, height, and beat frequency remain the same). The effect of additional cilia introduced into the flow domain not only changed the net displacement (which is expected, increasing the cilium patch fraction by adding more energy into the system per unit area), but it tremendously affected the trajectory paths. With these two images in mind, we proceed to compare the effects that each configuration has on the transport of particles.

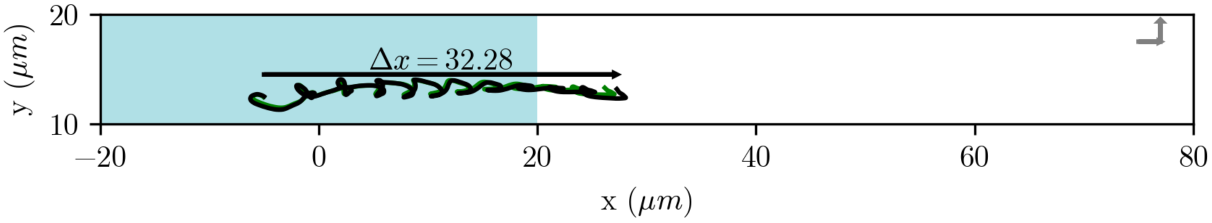

(a) Baseline parameters: $f = 10$ hz; $h_p = 20$ μm; $l_d = 40$ μm

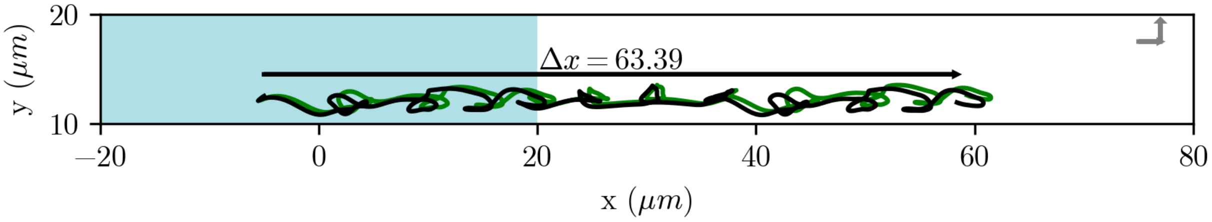

(b) Baseline parameters: $f = 10$ hz; $h_p = 20$ μm; $l_d = 40$ μm; $l_c = 3$ μm; $\lambda = 200$ μm

Figure 4.9: Trajectory comparisons between tracer (solid black line) and circular particle (green line). All seed locations are the same $x = 5\mu$m and $y = 12.5\mu$m; top panel is the baseline single cilium configuration, while the bottom panel shows the baseline cilium patch configuration. Note that the x and y axes are not equal, and the unit vectors are shown in the top right corner as grey arrows. Additionally, the area of the flow domain is shaded blue (i.e. the spanwise extent of the repeating single cilium or cilium patch unit)

In line with observations with a repeating single cilium unit, frequency affects the flow rate significantly, but does not result in any increased particle clearance. In Figure 4.10, we see a constancy in both the arc-length trajectories and a tracer particle. However, as was described previously, these metrics are to be viewed *per cycle*, but in this case, we can make another distinction, *duration of all cycles*. In this particular case, we see that particle trajectories are constant for all frequencies, but of course, a cilium at a frequency of 10 hz beats twice as slow compared to 20 hz. This implies that fast beating cilia clear particles at the rate of which they are beating, which is rather trivial, and of course observed experimentally.

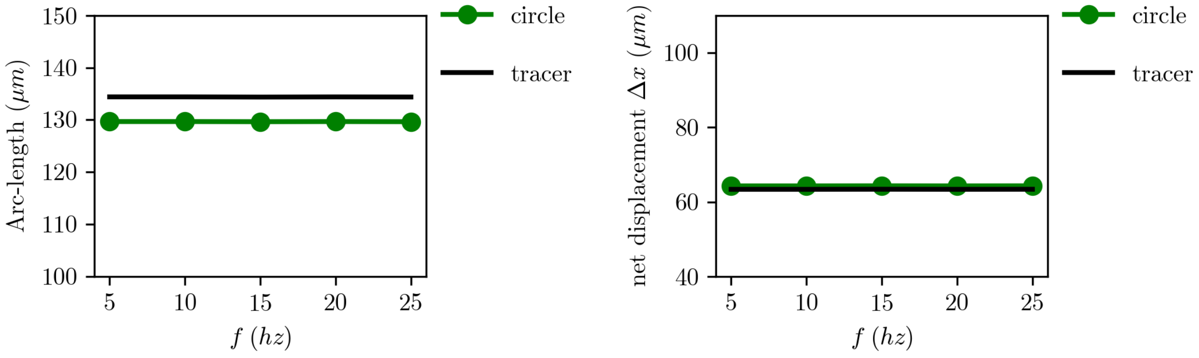

(a) Arc-length trajectory (b) Displacement

Figure 4.10: Total arc length (left) and net displacements (right) for frequency range $f = 5 - 25$ hz

Now, turning our attention to periciliary height, in Figure 4.11, we see that only the net displacement follows a monotonic increase when increasing periciliary height. Conversely, the arc length trajectories are evidently more complex as shown in Figure 4.9. These differences account for the increased arc lengths as an increase in the periciliary height allows more room for the particle to tumble and translate. In Chapter 5, we introduce more quantitative metrics to describe this phenomena.

As we described earlier, the parameter range for metachronal wavelength comparisons was calculated by not allowing inter-cilium spacing to overlap. Thus, our parameter range for wavelength was more restrictive, and as such we did not expect to see much difference. For wavelengths that approach synchrony (in our simulations $> 600\mu$m), we see little change in both the arc length and displacement as shown in Figure 4.12. However, there seems to be a loss of the cooperative effect when considering the smaller wavelengths, and indeed a wavelength of 400μm out performs the smaller wavelength in producing longer trajectories. This is not to say, though, that the net displacements are larger, as indicated by Figure

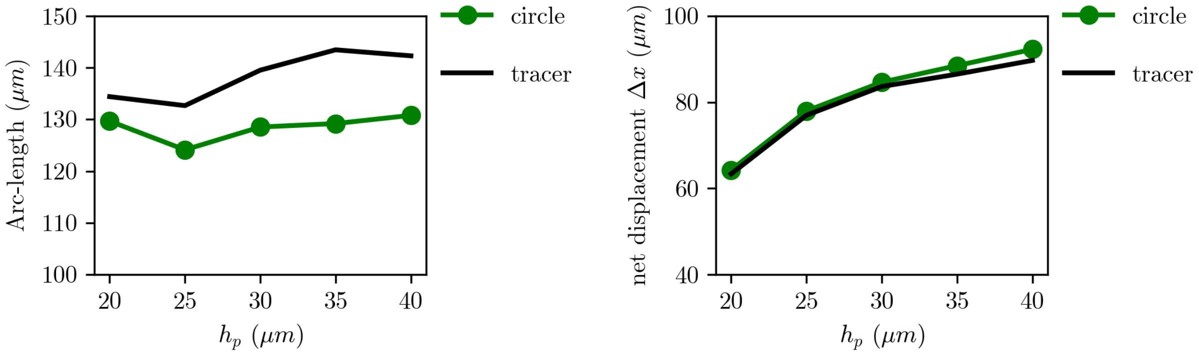

(a) Arc-length trajectory (b) Displacement

Figure 4.11: Total arc length (left) and net displacements (right) for periciliary height range $h_p = 20 - 40$ μm

4.12b, which shows larger net displacements as we increase the wavelength.

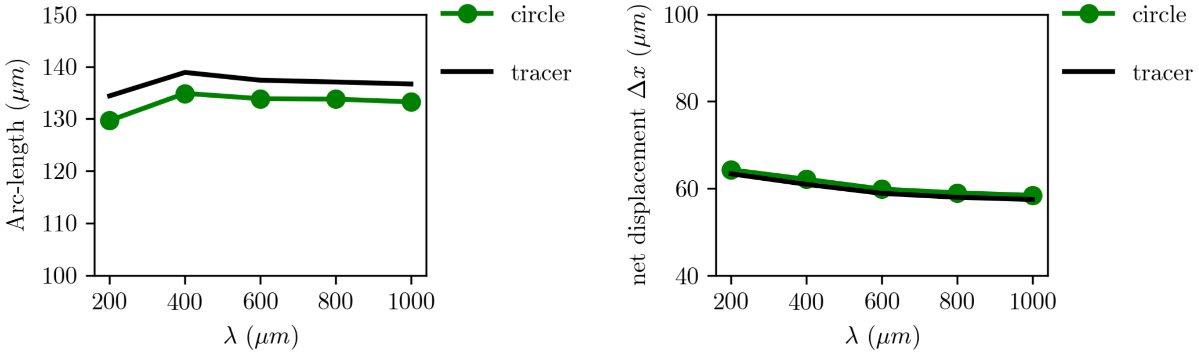

(a) Arc-length trajectory (b) Displacement

Figure 4.12: Total arc length (left) and net displacements (right) for metachronal wavelength range $\lambda = 200 - 1000$ μm

Finally, we now describe particle clearance as a function of the cilium patch density. We begin first by describing features of particle transport in response to changes in domain length (Figure 4.13), and then consider changes to inter-cilium spacing (Figure 4.14). In Figure 4.13a, we see the largest effect in particle arc-length trajectories is indeed, changes in the domain length. Additionally, the particle net displacement also sees a large net displacement, however, much less than changes in periciliary height (Figure 4.11). The effect of decreasing domain length is effectively increasing cooperation between neighboring cilium patches, by increasing patch fraction. Now the opposite is true when increasing neighboring cilium spacing, i.e smaller spacing decrease cooperation and decrease patch fraction. This is highlighted by the trends in Figure 4.14, whereby increases in the inter-cilium spacing show an increase in particle transport. This is effectively increasing the patch density, spreading the cilia across the domain.

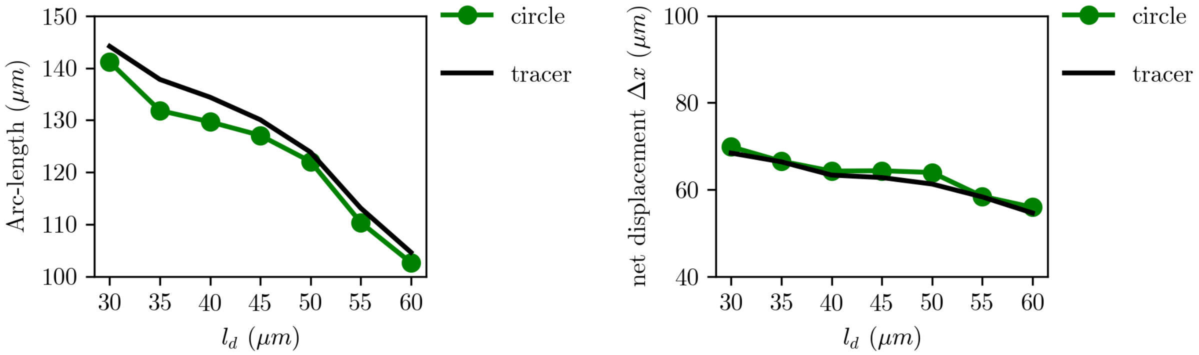

(a) Arc-length trajectory

(b) Displacement

Figure 4.13: Total arc length (left) and net displacements (right) domain length range $l_d = 30 - 60$ μm

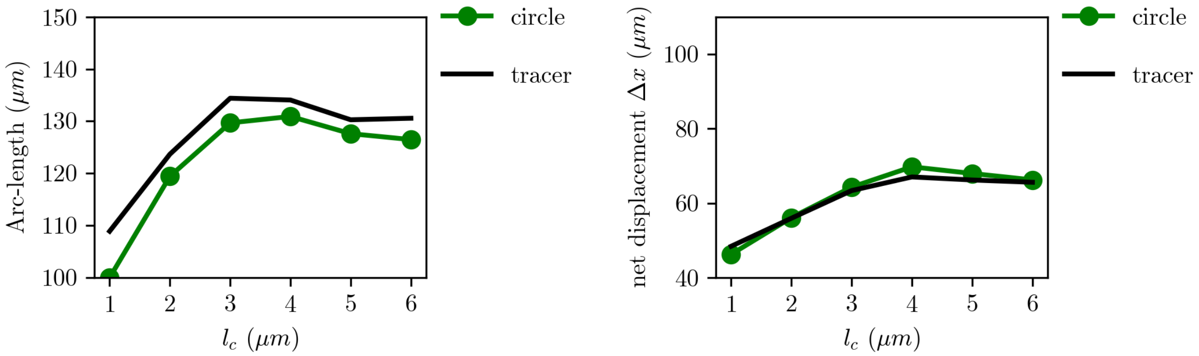

(a) Arc-length trajectory

(b) Displacement

Figure 4.14: Total arc length (left) and net displacements (right) inter-cilium spacing $l_c = 1 - 6$ μm

4.3 Discussion and Conclusions

Modeling mucosal region inherently carries some level of simulation sub-unit repeatability and inter-cilium repeatability due to the periodic boundary conditions. In our modeling effort, we have defined a cilium patch, and the fraction it occupies as a way to reduce the typical infinitely repeating cilium assumption, where cilia are inter-spaced at equal intervals for all of the flow domain. Several numerical simulations were carried in order to quantify the effect that this cilium patch fraction had on the transport of fluid and particle dynamics. First, simulations were run with a) only cilia beating, and then b) with an embedded circular particle. Additionally we set some limitations on our definition of the cilia beat kinematics, in order to not introduce spurious numerical results.

We evaluated the bulk clearance rates and found that periciliary height along with frequency increased fluid pumping the most. In one case, frequency, increases were attributed to larger maximal flow rates which is expected. However, in the case of periciliary height, flow reversal was reduced, and the increase was attributed to less "back flow" over time. This result was indeed surprising and to our knowledge, this effect from changes in the periciliary height, has not been documented before. The implication of this result challenges simplified modeling assumptions that treat the flow domain as infinite in the y-direction, such as in the use of regularized Stokeslets[49, 52, 73, 109]. To date, several numerical studies have used this method, and in our work, the numerical methodology employed allows for the existence of a finite boundary. There are methods, such as the boundary integral method, that allow for the use of regularized Stokeslets with a moving or stationary wall, which was most recently used by Guo et al. [74] to model cilia transport in a non-uniform *bounded* and *periodic* domain. While our work here does not include an arbitrary wall shape, it can most certainly be employed to do so. We additionally mention that our goal in modeling cilium patch fraction was for the introduction of some variability to periodicity, which the case of regularly spaced cilia, does not have.

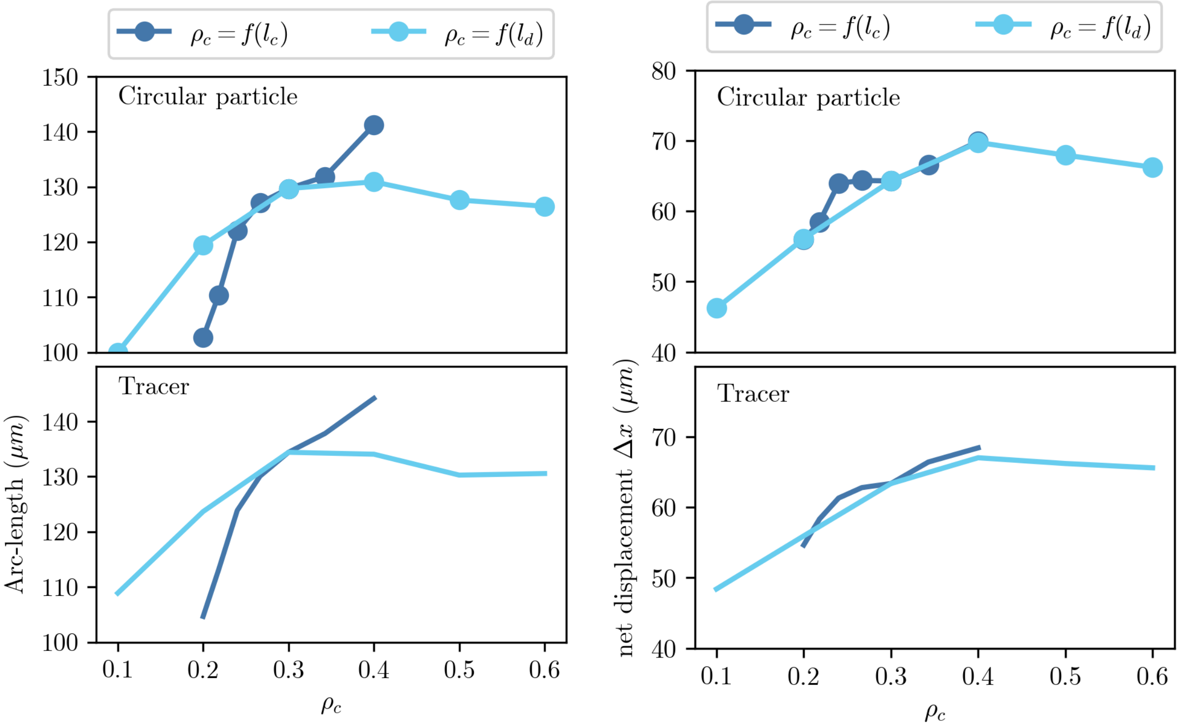

(a) Total arc-length trajectories as a function of cilium patch fraction

(b) Net $x-$axis displacement as a function of cilium patch fraction

Figure 4.15: Comparisons between changing cilium patch fraction using two geometrical parameters, cilium spacing (l_c) and cilium patch distance (l_d). Top panels in each Figure correspond to the finite-sized particles, while the bottom panels correspond to the tracer particles.

—*Optimal Patch Particle Clearance:* By varying the cilium patch fraction with two parameters, cilium spacing and domain length, we sought to compare the effects that these two parameters had on particle transport. In Figure 4.15, we combine these results to describe more in detail the implications of irregular spaced cilium patches. First, we note that finite-sized particles and tracers follow similar trends as described in Section 4.2. Here they are reproduced, but now as a function of cilium patch density ρ_c. We then look to compare the arc length trajectories that are produced (in both finite-sized particles and tracers), which correspond to the left hand-side panels. Here we see that there is a local maximum in particle trajectory as we increase the cilium patch fraction as a function of domain length. Conversely, we see that the change in arc-length trajectories per percent increase in cilium patch fraction are not equivalent. This is due to our model requirement that metachronal wavelength is influenced by cilium spacing, thus by keeping wavelength constant, the “rate” by which particle trajectories change, changes due to the phase lag between cilia. Nonetheless, our results show that there is a local maximum when considering cilium patch fraction, which is equivalent to percent cilia coverage. In our parameter selection, cilia patch fraction ranges from 10% to 60%, which encapsulates the range observed in real human lungs. When the patch fraction is smaller ($\rho_c \sim 0.1$), arc-length trajectories are about 27.4% less than when considering larger patch fractions ($\rho_c \sim 0.6$). This effect is also seen when considering differences in the net-displacements, where the smallest patch fraction is 20.2% less effective compared to the largest patch fraction. Thus, our results show that particle clearance in the lower tracheobronchial tree is not as effective when compared to clearance in trachea and first generations. These measurements further down the tracheobronchial tree would be quite difficult to assess *in-vivo*.

Chapter 5

Effect of particle shape on clearance

5.1 Methodology

Particles that are inhaled vary widely in shape, size, and composition [5]. For the purposes of our study, we focus on regular-shaped particles, that are easily defined from mathematical relations. The three particle shapes we consider in 2 dimensions are shown in Table 5.1: circular, square, and elliptical cross sections. For the elliptical cross section, we keep the major to minor axis ratio 2:1. Initially, we set the particle diameter in relation to the length of a single cilium as 5 μm (ratio of 1:2). This serves as an initial experiment to see the affect that particle projected cross-sectional shape has on the transport. However, in the literature, comparison between particle shapes is often a geometrical and theoretical question. For an excellent and recent review on particle shape comparisons, see [111] and an application of particle shape effects, see [112]. Following the recommendations in [111], we consider the aerodynamic resistance diameter (ARD), which is a form of volume and drag force matching for particles of distinct shapes.

To determine the ARD, we run a series of simulations to calculate the drag force for a variety of particles shapes which then allows us to calculate an equivalent ARD between different shapes in comparison to a circular particle (in 2 dimensions). Since we are performing numerical simulations, it can be tempting to run a series of simulations over a range of Reynolds numbers while varying particle shape and calculate the coefficient of drag, and then match each ARD appropriately. But a few questions stand to be asked: How does one control Reynolds number in the simulation framework? How can one calculate drag per unit length accurately over a cylinder when using a first order accurate method like the immersed boundary method? Do our results approach the Stokes limit for a linear drag coefficient as Reynolds number approaches zero? All of these questions must be carefully analyzed and, luckily, this classical academic fluid dynamics problem is still an active area of research.

Much of the envelopment of numerical methods that attempt to solve the infinitely long cylinder in 2 dimensions have been aimed at solving the Navier-Stokes, and the Stokes equation in the limit as Reynolds number approaches zero, but inconsistencies plague accurate drag calculations [66]. However, as we get closer to zero Reynolds number, numerical errors creep in, and in the case of this classic Stokes' Paradoxical problem, a careful determination of the appropriate simulation conditions is favored. In fact, Gholami Korzani et al. [113] most recently attempted to solve this problem using an accurate smoothed-particle-hydrodynamics method to calculate drag over a 2D cylinder at creeping flow Reynolds number ($Re = 3\times10^{-5}, ..., 1$). Much like experimental results, they found that the computational domain size was an important parameter affecting the accuracy of the drag calculations. This topic is reviewed in the work by Khalili and Liu [114] more recently, pointing to both experimental as well as numerical issues with a simple problem definition that can have such a degree of uncertainty in the calculation of the drag coefficient. In the following determination of ARD, we proceed cautiously in our problem definition, in order to minimize numerical errors in calculating the drag coefficient.

The problem considered is flow over a cylinder of diameter D, where the incoming velocity is U_∞, and the domain is length is L and the domain height is H, We select the diameter at the characteristic length, and the inflow velocity as the characteristic velocity. We initially set these values as $D = 1$, $H = 16$, and $L = 2H = 32$, all centered at $(x, y) = (0, 0)$. A depiction of the numerical domain is shown in Figure 5.1, where the inflow boundary condition is at the $x = -16$ plane and all other boundaries are outflow boundary conditions.

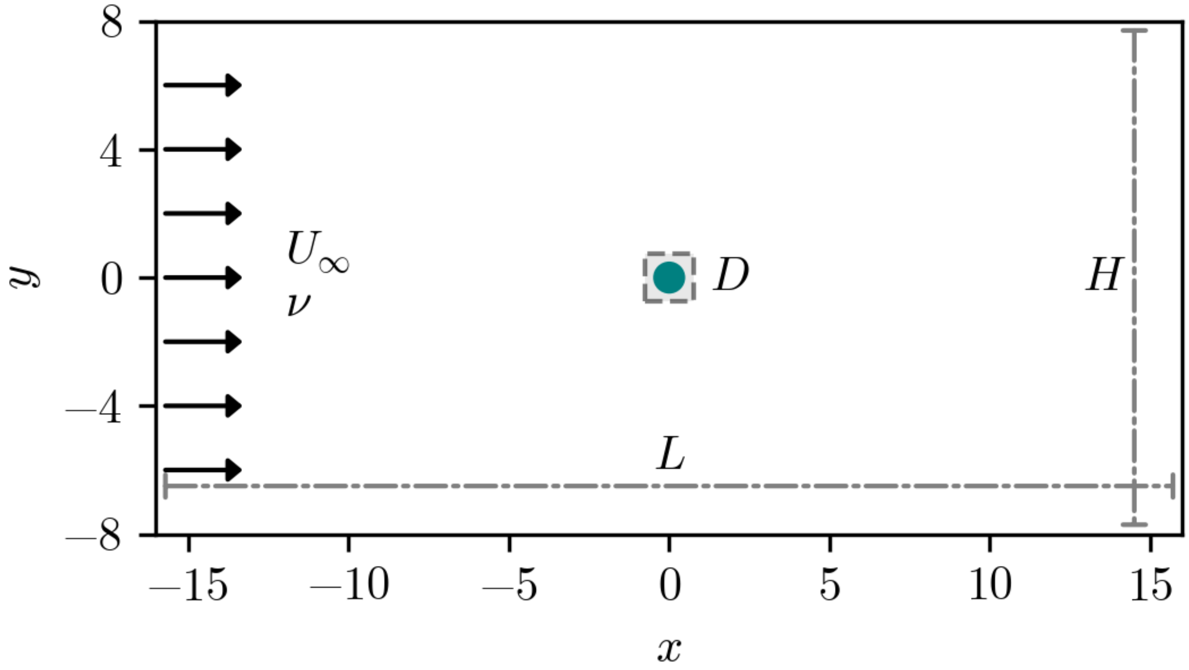

Figure 5.1: Simulation domain with a cylinder of diameter, D, centrally located in the domain $(x, y) = (0, 0)$. Uniform inflow boundary conditions are at $x = -16$. Domain dimensions are $W \times H$

We define the Reynolds number as,

$$Re = \frac{U_\infty D}{\nu} \tag{5.1}$$

and the 2-dimensional drag coefficient as the force per unit length divided by the dynamic pressure as

$$C_d = \frac{F_d}{\frac{1}{2}\rho U_\infty^2 D} \tag{5.2}$$

We make use of the IBAMR's implementation of the moving control volume approach to calculating the drag force, F_d, [115], which in this problem is not necessary since the cylinder is held stationary relative to the incoming flow field, but can be useful in the calculation of hydrodynamic forces when the immersed boundary advects with the fluid or is coupled to the flow equations.

5.1.1 Aerodynamic Resistance Diameter

The aerodynamic resistance diameter (ARD variable henceforth denoted as D_a) is defined as the diameter of a sphere with a standard reference density (ρ_0) that settles to a terminal velocity (U_t) which is equal to that of some other particle (typically non-spherical or aggregates) of interest. The working fluid is typically air, with kinematic viscosity of $\nu_f = \frac{\mu_f}{\rho_f}$. In order to calculate D_a, we begin by equating the force of gravity to drag force for both a (Stokesian) spherical particle (Eq. 5.3), and that of an arbitrary shape (Eq. 5.4).

$$F_g = \frac{\rho_0 \pi D_a^3 g}{6} \tag{5.3}$$

$$F_g^{ve} = \frac{\rho_p \pi D_{ve}^3 g}{6} \tag{5.4}$$

The standard reference spherical particle has density and diameter of ρ_0, D_a and the arbitrary shaped particle has a density and volume equivalent diameter ρ_p, D_{ve}. For the spherical particle, the drag force is equal to the Stokes drag,

$$F_d = 3\pi \nu_f U_t D_a \tag{5.5}$$

However, for an arbitrary shaped particle, a correction to the Stokes drag can be made to find the drag force. We have adopted the earliest correction for volume equivalent shapes, the dynamic shape factor from Fuchs [116],

$$\chi = \frac{F_d^{ve}}{F_d} \rightarrow F_d^{ve} = \chi 3\pi \nu_f U_t D_{ve} \tag{5.6}$$

where F_d is the drag force of a spherical particle, and F_d^{ve} is the drag force of a volume equivalent arbitrary shaped particle.

In Equation 5.5 and 5.6, the terminal velocity U_t, and both particle diameters, D_a and D_{ve}, are unknown quantities. By setting Equations 5.3 and 5.5 equal for the sphere, and

Equations 5.4 and 5.6 equal for the arbitrary particle, we can rearrange each equation for terminal velocity. This allows use to solve for the aerodynamic resistance diameter as a function of the volume equivalent diameter and the Fuchs correction factor, which must be calculated from experiments (ratio of drag forces),

$$D_a = D_{ve}\sqrt{\frac{\rho_p}{\chi\rho_0}} \tag{5.7}$$

Since our simulations are in 2-dimensions, all our particles are cylindrical in nature, so we use the circular cross section as our standard reference particle, and use the cross-sectional area as the equivalent volume scale. We set all particles to be equally dense, and they are neutrally buoyant ($\rho_0 = \rho_p = \rho_f$) since many inhaled particles have densities similar to that of water, allowing us to then calculate our aerodynamic resistance diameter, $D_a = D_{ve}\sqrt{\frac{1}{\chi}}$.

In order to calculate an equivalent aerodynamic resistance diameter, we run simulations using the particle cross-sectional diameter as the independent variable. In all our simulations, we hold the particle diameter to free-stream domain height and length constant. That is to say, the particle diameter to domain height (or length) is constant: $\frac{D}{H} = 1/16$ and $\frac{D}{L} = 1/32$. We also verify this result by running a series of simulations at different Reynolds number ($Re = 0.1, ..., 200$) when varying both μ and U_∞, while keeping the other variables constant (results not shown) to show the drag force is consistent. We vary the particle diameter from $D = 0.5, ..., 1.5$ for 5 distinct sizes, while keeping all other variables constant, $\mu = 1.0$, $\rho = 1.0$, $U_\infty = 1.0$. From here, we calculate the area equivalent diameter for an ellipse and square cross section, and use an exponential fit between the 5 particle diameters for the results of each cross section. We evaluate the exponential fit at the equivalent area diameter and calculate the drag force from the coefficient of drag. From these evaluated forces, we can calculate χ, and the corresponding ARD, D_a. We show the tabulated ARD values in Table 5.1, which are $D_a = 0.427$ and $D_a = 0.709$ for a square-like and elliptical particle respectively. The process to calculate the ARD is shown visually in Figure 5.2, which is

	Circular*	Square	Elliptical
Shape equation	$x^2+y^2=\left(\frac{D}{2}\right)^2$	$x=y=D$	$\left(\frac{D}{2}\right)^2+\left(\frac{D}{4}\right)^2=1$
area equivalent diameter - D_{ae}	0.5	0443	0.707
aerodynamic diameter - $D_a=D_{ae}\sqrt{\frac{1}{\chi}}$	0.5	0.427	0.709

Table 5.1: Particle shape functions and cross section diameter. *Circular particle is the standard reference.

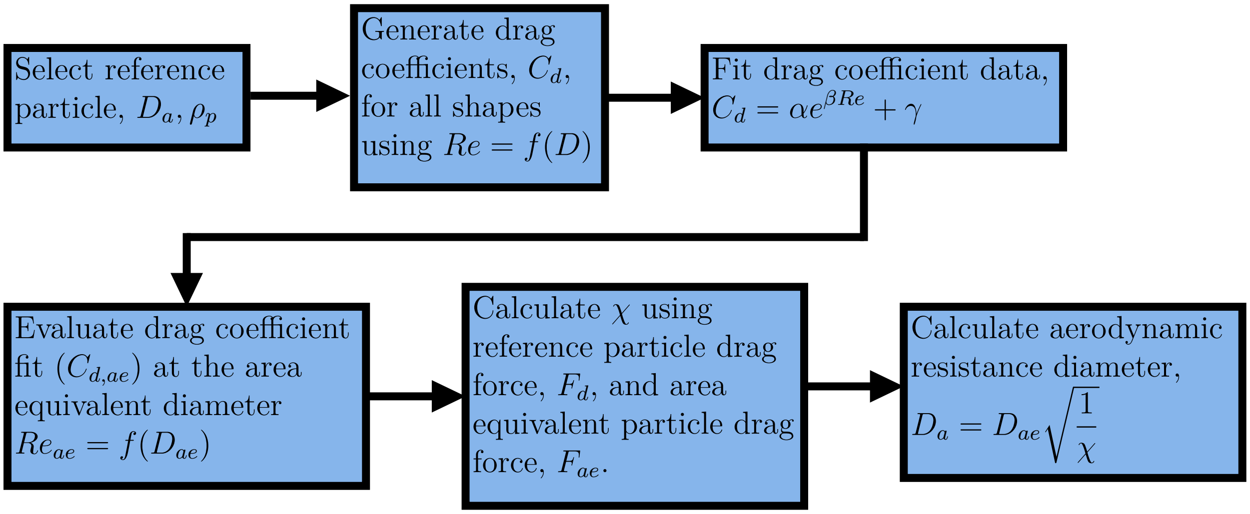

Figure 5.2: The process to calculate the aerodynamic resistance diameter, D_a, for an arbitrary shaped particle with area equivalent diameter, D_{ae}.

done for each particle shape. The exponential fits are shown in Figure 5.3 which show the calculated drag coefficients from the results of the simulations.

We note the challenges of matching the hydrodynamic drag with real coarse particulate matter in 3D since particle imaging at such fine scales is usually done from 2D images, which may distort the 3rd-axis dimension. However, our simulations are 2D and can be considered infinite in the normal planar direction. For future 3D simulations, we could calculate a more appropriate metric such as sphericity or Fernet diameter as is used in both experimental and numerical simulation research of suspended particles.

For cilia-particle simulations, we seed these finite-sized shaped particles in the flow domain at the same constant location as in previous chapters, $(x, y) = (-5, 12.5)$ μm, which is directly left of center in the domain. Square particles are seeded in the flow initially with their planar face perpendicular to the x-direction. Elliptical particles are seeded with their

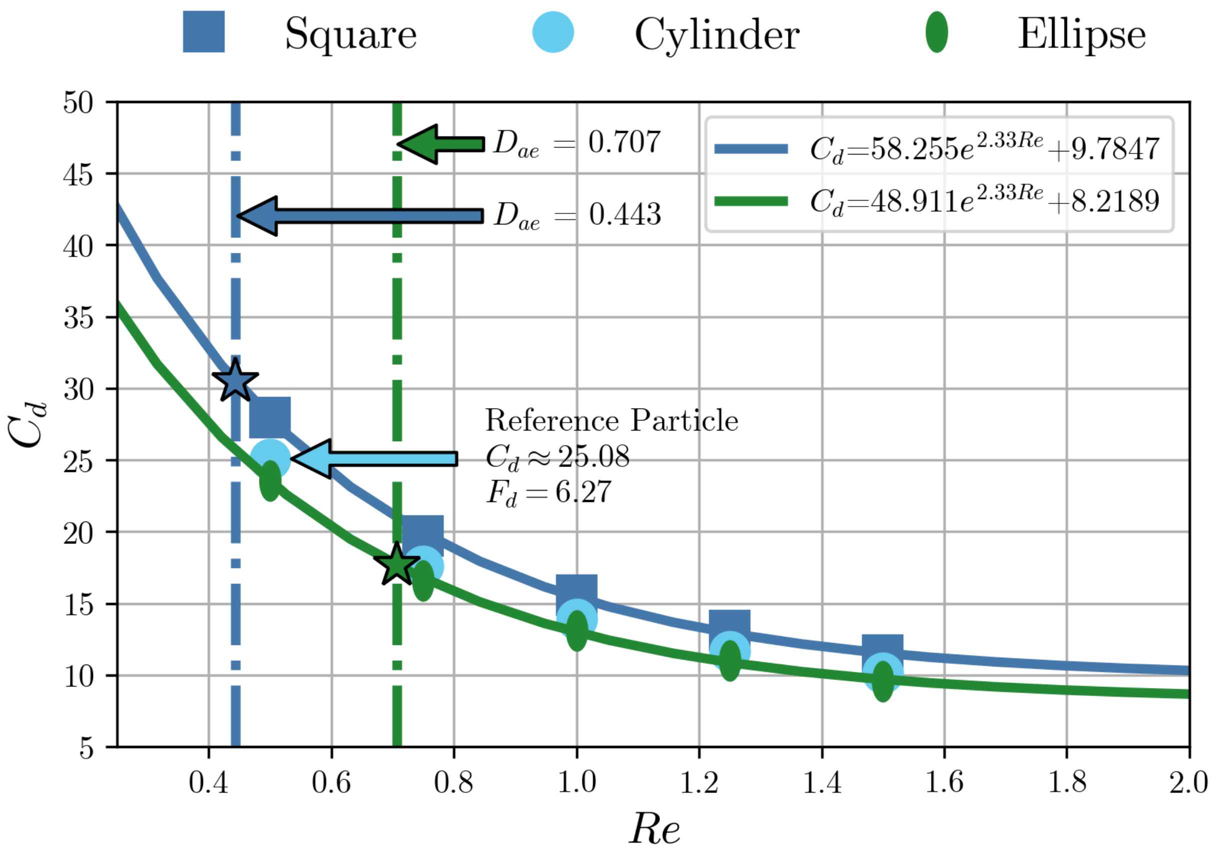

Figure 5.3: Aerodynamic diameter matching for distinct particle shapes. The standard reference circular particle is highlighted with a cyan arrow, along with the corresponding drag coefficient value and calculated drag force from the simulations. All solid markers correspond to the steady-state values of C_d from the simulation results. The solid lines correspond to the exponential fit of the drag coefficient data values, $C_d = f\,(Re)$ from simulation results for both elliptical and circular particle shapes. The area equivalent diameters are denoted using a vertical dash-dotted line, which are used to evaluate the drag coefficient values. The evaluated drag coefficient values are shown as stars outlined in black, with coloring corresponding to either the square-like or elliptical particle. R^2 values for both square-like and elliptical particle shapes are 0.9993 and 0.9993, respectively.

major axis both parallel and perpendicular to the x-direction. Additionally, we do not prescribe a particle-cilium contact model, thus no overlap or contact is experienced with the particles.

We close this section by marking some important features about the problem configuration we described in Chapter 3 and Chapter 4. In our simulations, we have allowed a finite particle to be coupled to the flow completely, implying that the particle exerts some force on the fluid, and the fluid exerts some force on the particle. Unlike the cilium, which only exerts force on the fluid, these particles have feedback back from the fluid in the form of drag and lift force as well as torque. Thus in our definition of particle shape and subsequent calculation of the ARD, we note that particle drag is calculated from a stationary configuration, which holds the particle in place, disallowing rotation and translation. In our simulations (and results that follow), we see that this is not entirely the case. Particles exhibit much more complex motion than was previously analyzed by simply looking at trajectory paths. It is the intention of our simulations to capture this complex behavior to give insight into how finite-sized arbitrary shaped particle dynamics evolves over time.

5.2 Results

Having defined more precisely a fair comparison between particles of different shapes via the aerodynamic resistance diameter, we now consider the effect that particle shape has on clearance. More specifically, we aim to show that unless particles have equivalent ARDs, their trajectories greatly vary. Moreover, we show that particles which have an aspect ratio not equal to 1 have far more complex dynamics than those that are isometric. Finally, we quantify differences between a tracer particle, an isometric particle, and a non-isometric particle by studying their dynamic evolution in the flow.

5.2.1 Finite-sized Particle Trajectories

Effects of Aerodynamic Resistance Diameter

We begin our discussion by comparing results from particle transport of equivalent cross-sectional particle diameters (CPD), and equivalent aerodynamic resistance diameters (ARD). Additionally, to get a baseline comparison, we only seek to compare these results in the single infinitely repeating cilium unit, as the parametric space is smaller. First, in Figure 5.4, we clearly see that for equivalent CPDs, the total arc length trajectory varies between particles as compared to those with equivalent ARD. In fact, we arrive at the following conclusion, when matching ARD, particles exhibit no change in their arc length trajectories. This is more evident when considering the net displacement. In Figure 5.5, we see that both equivalent CPD and ARD have almost equivalent transport. Of importance, however, is that tracer particles have theoretically infinite drag, and thus always travel further than finite-sized particles.

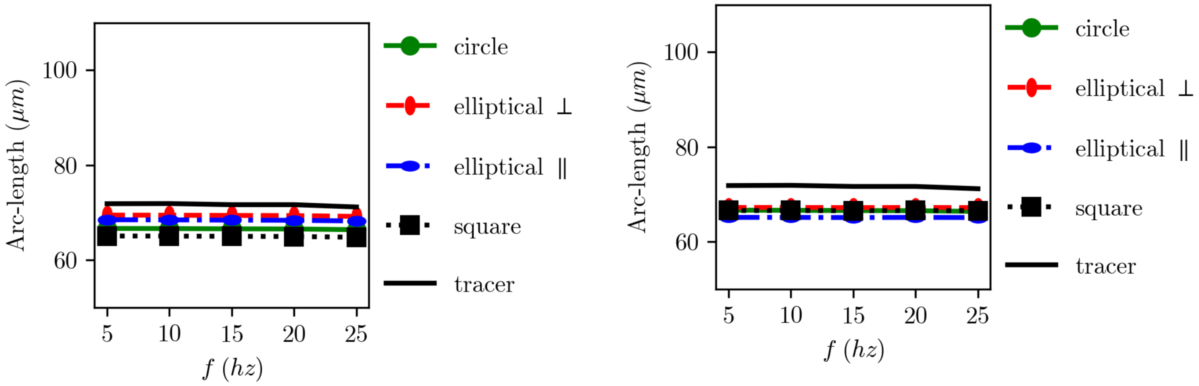

(a) Equivalent cross-sectional diameters

(b) Equivalent aerodynamic resistance diameters

Figure 5.4: Comparison of arc-length trajectory between CPD (left) and ARD (right) for changes in cilium beat frequency $f = 5 - 25$hz

These results on changing frequency and their effect on different shaped particle transport seem very straight-forward, however, when introducing changes to the configuration via the geometric parameters, more complex behavior is exhibited. While changes to periciliary

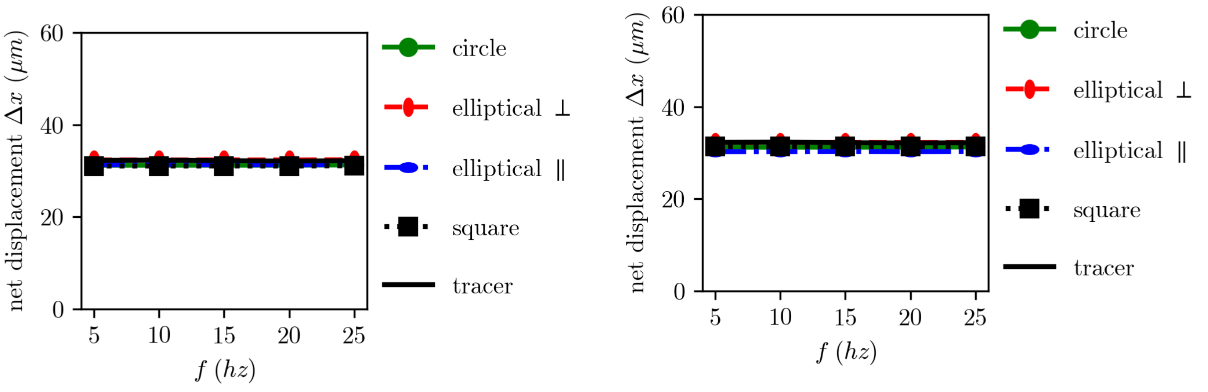

(a) Equivalent cross-sectional diameters

(b) Equivalent aerodynamic resistance diameters

Figure 5.5: Comparison of net particle displacement between CPD (left) and ARD (right) for changes in cilium beat frequency $f = 5 - 25$hz

height do not change among particle shapes, these trends do differ *across* particle shapes. In Figure 5.6, we see evidence that particle shape affects the arc-trajectories, and indeed, in Figure 5.6a, elliptical particles exhibit less transport than the other shapes. However, when matching the ARD, we see that circular particles exhibit less transport. All the particles in Figure 5.6b have been matched via their (stationary) drag coefficients. It is clear that isometry and the degree of *roundness* affects the trajectories. Additionally, we can see the effect be more pronounced in Figure 5.7, where we see that for an equivalent CPD, particle displacements are virtually identical across the increase in periciliary height. However, we see more clearly in Figure 5.7b, that a circular particle and a tracer particle exhibit virtually indistinguishable trends, whereas the other particle shapes clearly have less net displacement.

Finally, we turn to analyzing changes in domain length, which is equivalent to add or reducing the spacing between a single repeating cilium unit. Again, we note that the *overall* trends are unchanged from our circular particle trajectories and net displacements seen in Chapter 3, however, as we introduce particle shape, we do see some differences in the trends between shapes. In Figure 5.8a, we see that increased stratification across particles occurs at larger domain lengths, while less differences are seen at smaller domain lengths (or closer spacing). This is not conserved when matching ARD as is seen in Figure 5.8b, where

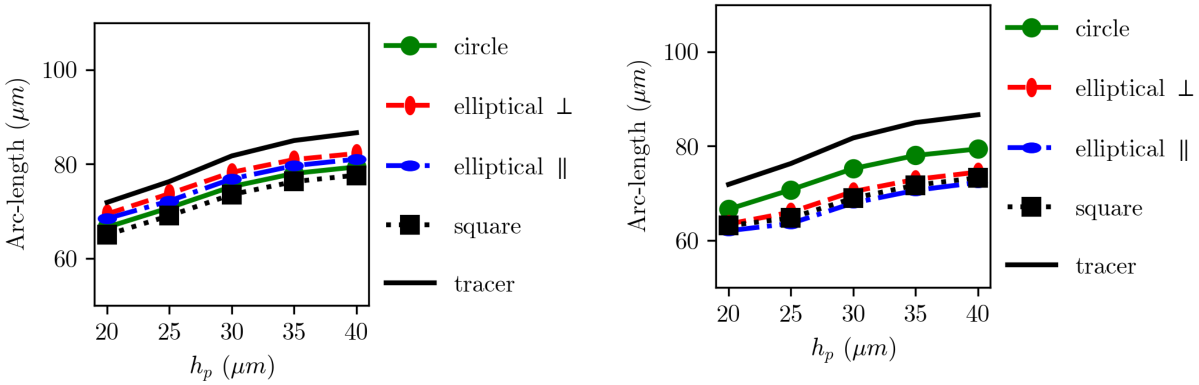

(a) Equivalent cross-sectional diameters

(b) Equivalent aerodynamic resistance diameters

Figure 5.6: Comparison of arc-length trajectory between CPD (left) and ARD (right) for changes in periciliary height $h_p = 20 - 40$ μm

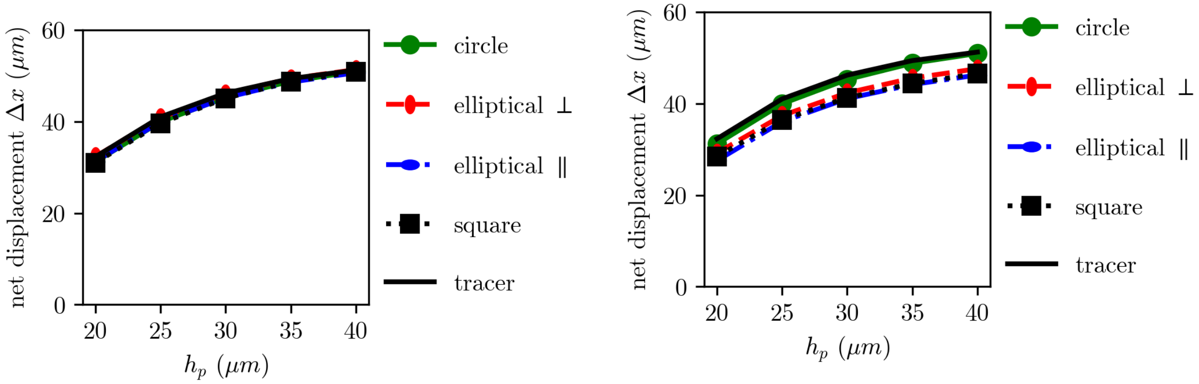

(a) Equivalent cross-sectional diameters

(b) Equivalent aerodynamic resistance diameters

Figure 5.7: Comparison of net particle displacements between CPD (left) and ARD (right) for changes in periciliary height $h_p = 20 - 40$ μm

the differences in arc-length trajectory between particle shapes at larger domain lengths is reduced. Nonetheless, the cilium beat shape is still very effective at clearing and transporting these particles, as is evident in the net-displacement over the entire domain length parameter range. In Figure 5.9b, net displacements are very consistent among particle shapes regardless of matching CPD with ARD. In all these trends, we point out again that behavior of particles in response to domain length changes fundamentally changes their trajectories as is displayed by measuring the arc length trajectory. The trends shown in Figure 5.8, are clearly non-monotonic, and the local minimum at $l_d = 60\mu$m when compared to a longer domain length ($l_d = 80$), produces drastically different behavior.

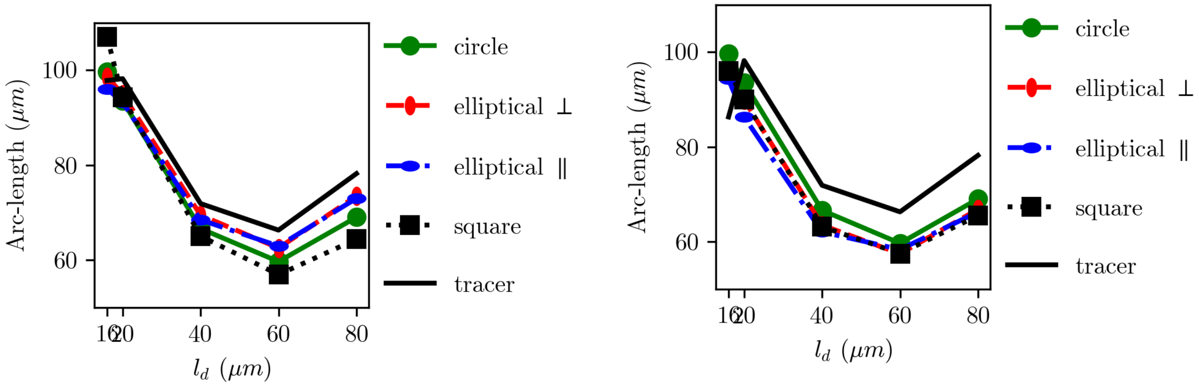

(a) Equivalent cross-sectional diameters

(b) Equivalent aerodynamic resistance diameters

Figure 5.8: Comparison of arc-length trajectory between CPD (left) and ARD (right) for changes in domain length $h_p = 16 - 80$ μm

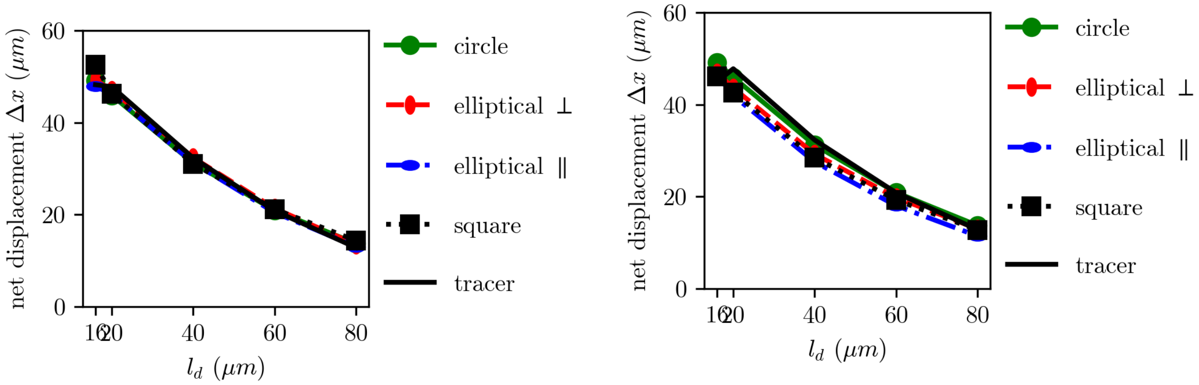

(a) Equivalent cross-sectional diameters

(b) Equivalent aerodynamic resistance diameters

Figure 5.9: Comparison of net particle displacements between CPD (left) and ARD (right) for changes in domain length $l_d = 16 - 80$ μm

Cilium Patch Transport of Arbitrary Shaped Particles

In this section, we present results for the transport of arbitrary shaped particles arising from a cilium patch. However, in this section, all our results are presented by matching the ARD with the circular particle, and as such, we expect to see less difference between shapes as compared to matching the CPD. However, as we be shown, particle shape, regardless of matching ARD, affects transport in a non-trivial fashion. Beginning with what we have established as a fair baseline for comparison, changes to the frequency again show no change to the transport. However, we do note that in comparison to the single cilium scenario particle shape does affect the total arc length trajectories as evidenced by Figure 5.10a.

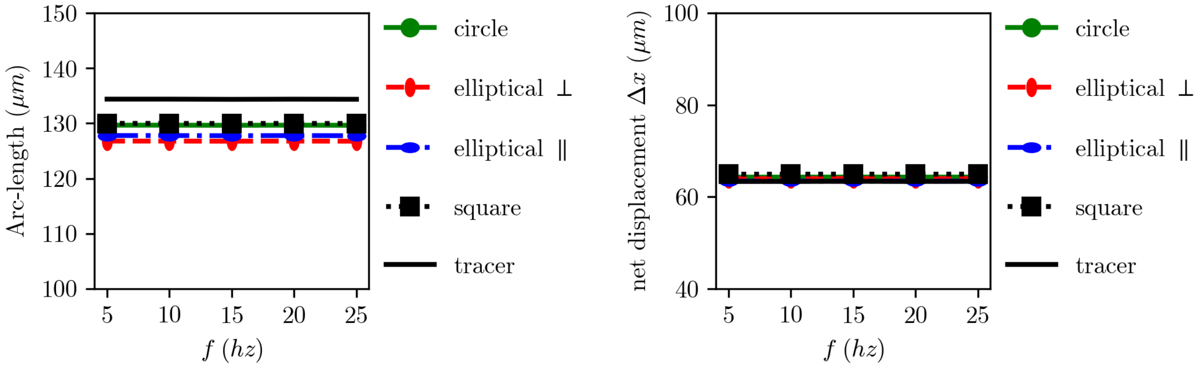

(a) Arc-length trajectory

(b) Displacement

Figure 5.10: Total arc length (left) and net displacements (right) for frequency range $f = 5 - 25$ hz

In analyzing changes to periciliary height, in Figure 5.11a, we see fairly consistent trends among different particle shapes when we increase periciliary height, but most notable is the difference between a tracer particle and all finite-shaped particles. Conversely, the net displacements are monotonically increasing as shown in 5.11b. Additionally, we see a minor difference at higher periciliary height among particles, and additionally, tracer particles have lower net displacements.

In exploring variation to the metachronal wavelength, we begin to see some of the more complex behavior around particle transport. This is expected since changing the metachronal wavelength offers particles a wider *spatial* beat orientation. More specifically, we see in Figure 5.12a, that lower wavelengths produce less arc-length trajectories across particles. However, for the first time, we see in our results largerlear evidence of divergent behavior among an equivalent shaped particle (the elliptical cross-section), purely due to the seed orientation. Nonetheless, the clearance of all these particle shapes, via measurement of the

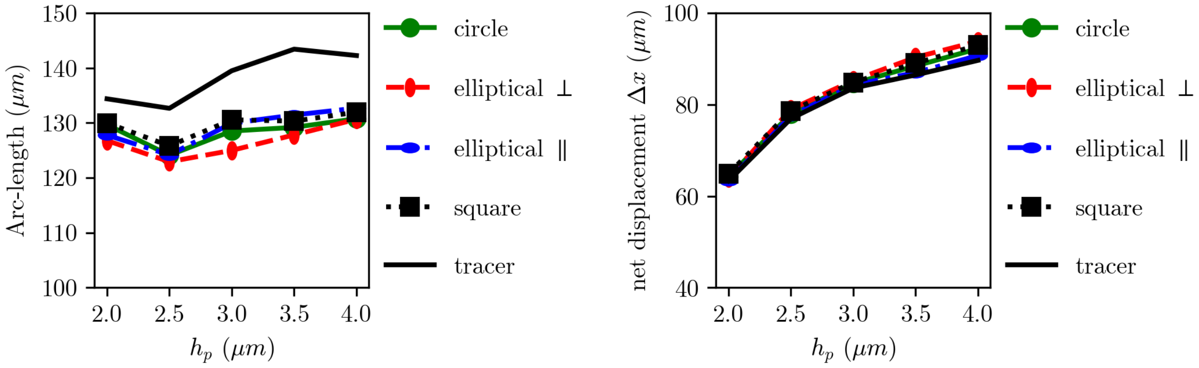

(a) Arc-length trajectory (b) Displacement

Figure 5.11: Total arc length (left) and net displacements (right) for periciliary height range $h_p = 20 - 40$ μm

net displacement in Figure 5.12b, show that longer wavelengths (or more in sync cilia) are less efficient.

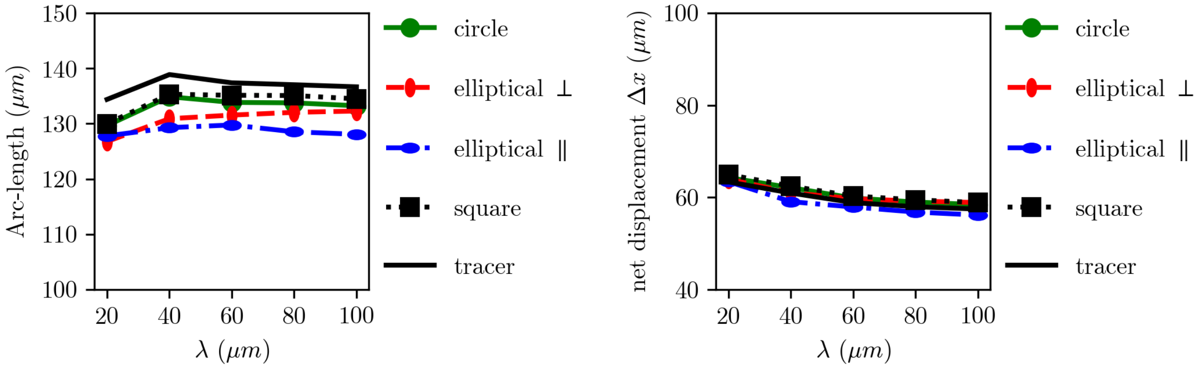

(a) Arc-length trajectory (b) Displacement

Figure 5.12: Total arc length (left) and net displacements (right) for metachronal wavelength range $\lambda = 200 - 1000$ μm

We complete our analysis of finite-sized arbitrary particle shape transport by describing changes as a function of the cilium patch density. Our results are similar to those described in Section 4.2.2, but note some interesting differences. First, in response to changes in domain length (Figure 5.13), we see that particle shape is more important at larger domain lengths. More specifically, we see that in Figure 5.13a, the elliptical particles diverge from circular and square-like particles after 35μm. This indicates that isometry affects transport at larger domain lengths. However, the net transport remains relatively unchanged as is seen in Figure 5.9a.

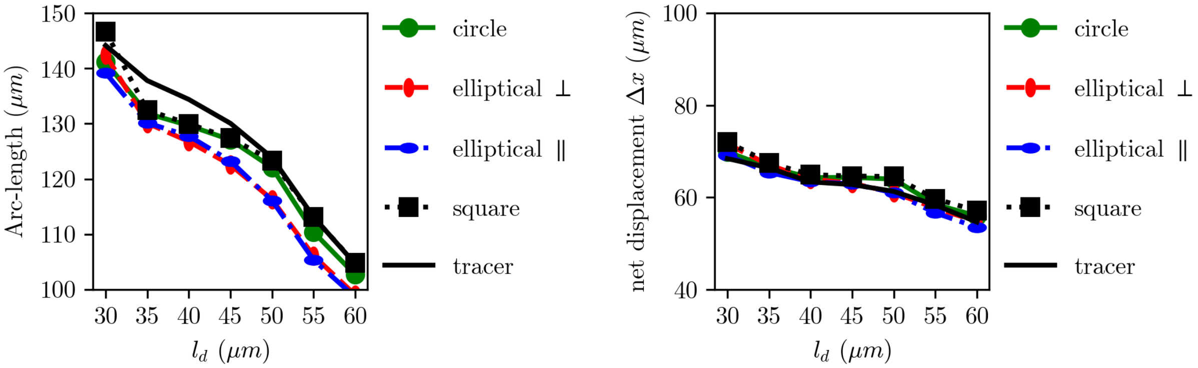

(a) Arc-length trajectory

(b) Displacement

Figure 5.13: Total arc length (left) and net displacements (right) domain length range $l_d = 30 - 60$ μm

When we analyze differences among shapes, arc-length trajectories are sensitive to changes, but for the most part, particle clearance via net displacement is unchanged. However, when looking at changes to inter-cilium spacing (Figure 5.14), we see evidence of particle shape affect *both* the arc length trajectories and net-displacements. In Figure 5.14a, we see the a clear divergence of the elliptical particle seeded in a perpendicular orientation from all the rest of the particles. We remind the reader that all particles are matched via the ARD. Additionally, if we consider the net-displacement (Figure 5.14b), higher transport of an elliptical particle, purely on the orientation of seeding, behavior is conserved. This result shows that finite-sized particles, even when having identical shapes, can be greatly influenced by their orientation in the fluid while being transported by beating cilia.

5.2.2 Translation and Rotation

In this section, we are looking to describe more carefully the effect that individual particle orientation in the fluid can have on their trajectories. Up until now, we have analyzed individual particle trajectories, their arc length and net displacement. However, as we previously

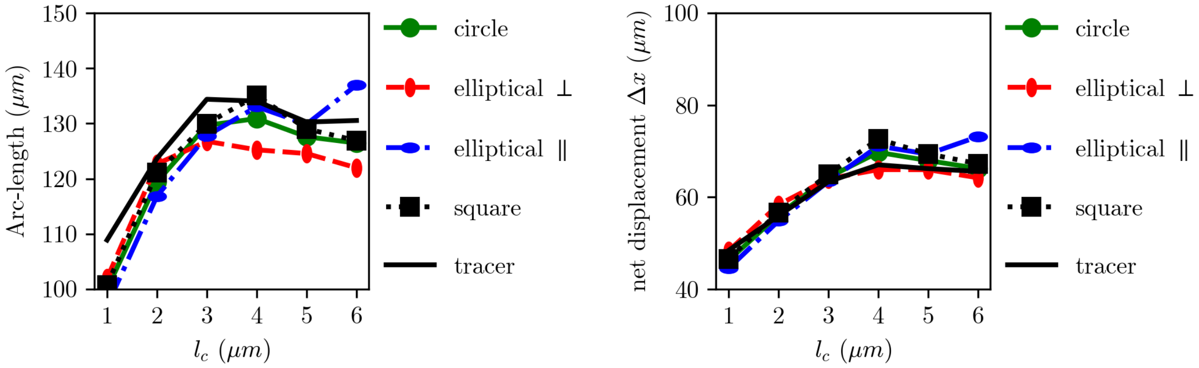

(a) Arc-length trajectory (b) Displacement

Figure 5.14: Total arc length (left) and net displacements (right) inter-cilium spacing $l_c = 1 - 6\ \mu$m

showed an equivalent particle shape that is not isometric can have differences in these measures. Thus, we begin our discussion by showing the *orientation* that a particle may have in relation to its starting configuration. To that end, in Figure 5.15, we show a comparison between a single cilium, and a cilium patch. The addition of multiple cilia in the domain changes the net transport as is evident by how far the particles travel in the $x-$direction. However, it is the orientation that we are interested in exploring more in detail.

In Figure 5.16, we plot the time course of the orientation, beginning at an angle that is 0 degrees relative to the x-axis. We are comparing the differences between particles in each figure, and the baseline configurations between figures. What is most apparent at first is the degree of transient behavior of each individual particle, as well as the magnitude of the behavior. For example, within the first 3 periods, for the single cilium configuration (Figure 5.16a), we see that a particle makes a quarter turn during the forward beat cycle, and then almost a quarter turn back into the original configuration. As the beat cycle progresses, however, this effect is diminished, as the particle has now moved into a dynamic that is more translation than rotation. This is indicated by the plateau in rotation angle at around the 8th beat cycle. When considering the cilium patch model in Figure 5.16b, we see the emergence of more dynamic rotation, with an increase to the rate as which rotation occurs. Additionally, because we are concerned with a patch of cilia instead of a single cilium, the plateau in

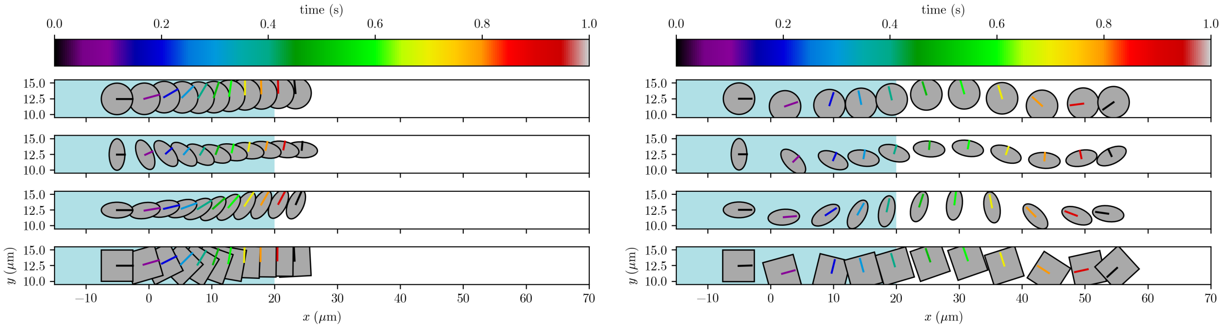

(a) Single cilium unit

(b) Cilium patch

Figure 5.15: Comparison between baseline configuration for the single cilium unit (left) and cilium patch (right). Each figure, shows the orientations of the individual particles, where the top panel in each figure, corresponds to the circular particle, the second panel corresponds to the elliptical particle oriented initially perpendicular to the x-axis, the third panel show the same elliptical particle oriented initially parallel to the x-axis, and the bottom fourth panel shows the square-like particle. The blue shaded domain is the length of the domain. The orientation is depicted by showing a horizontal line that is black at the start of the first beat cycle. As time evolves, this horizontal line rotates and is colored by its respective time as indicated in the color-bar above the image.

rotation is shorter than in the case of a single cilium. However, it is here that we see better insight into distinct particle shapes, and more specifically, how they change orientation. In the single cilium case, the elliptical shapes have different magnitudes of rotation, where the perpendicular ellipse follows closely the other isometric shapes. Similarly, in the the cilium patch case, we see that the rotation of an perpendicular ellipse follows closely that of an isometric shape, but after 5-6 beat cycle, the orientation now is reversed, and thus the parallel ellipse now follows closely the isometric shapes.

We now look to analyze the extreme cases as we vary each parameter individually for both a single cilium and a cilium patch. We begin by considering changes in the periciliary height, since our baseline case is the bottom extreme of our parameter range ($h_p = 20\mu$m), thus we only consider the highest deviation at $h_p = 40\mu$m. In relation to our baseline case, the behavior is subdued, that is to say, the the angular velocity is reduced, and there is a longer plateau where rotation does not occur. Additionally, having a higher periciliary height reduces the *orientation switch* that was seen in the baseline case, which in this case

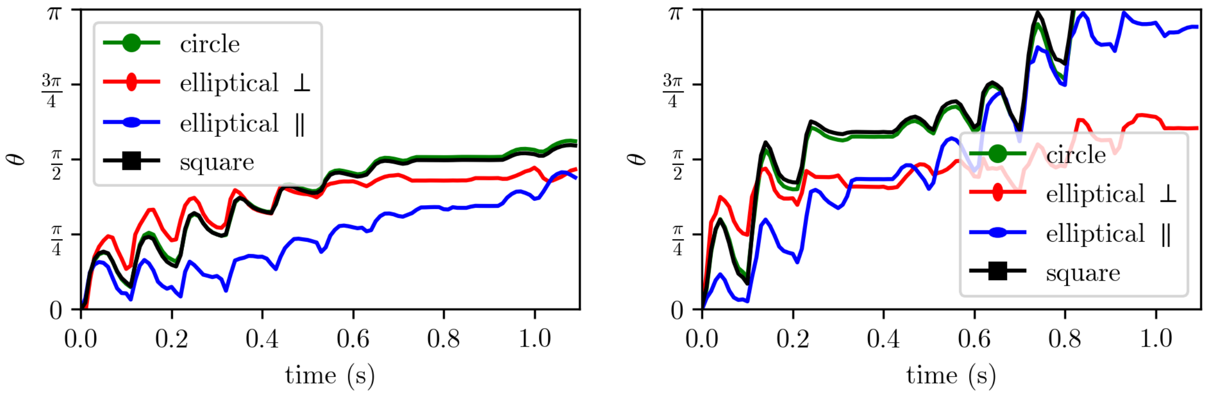

(a) Single cilium unit (b) Cilium patch

Figure 5.16: Comparison of rotation angle between baseline configuration for the single cilium unit (left) and cilium patch (right), for all particle types considered. In each Figure, we plot the rotation in degrees from the initial orientation as a function of time. At an angle of $\pi/2$, the particle has made a quarter turn rotation, switch, and at an angle of π, the particle has now reversed its orientation. Of course, making a full complete rotation would be indicated by an angle of 2π.

means neither the parallel ellipse nor the perpendicular ellipse make a full rotation.

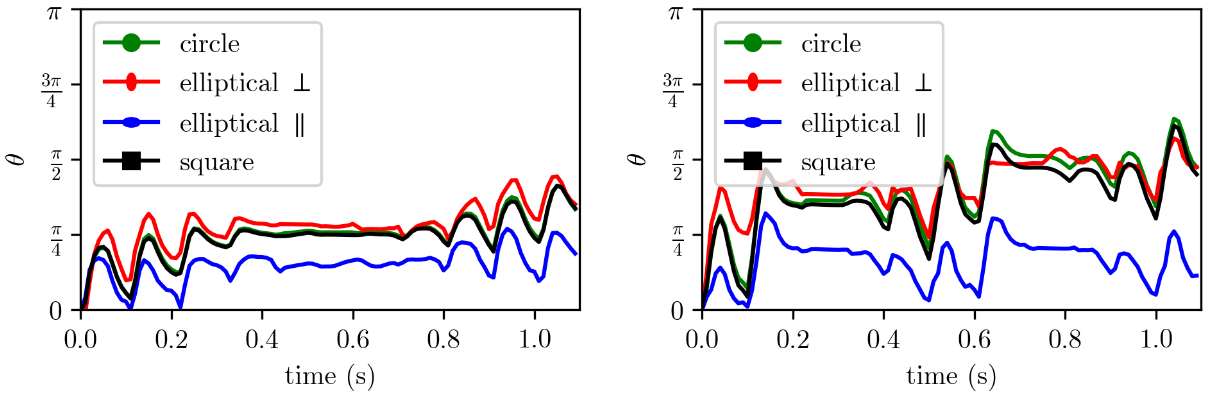

(a) Largest periciliary height for single cilium (b) Largest periciliary height for cilium patch

Figure 5.17: Comparison of rotation angle between the single cilium unit (left) and cilium patch (right), for all particle types, at a fix periciliary height, $h_p = 40\mu$m.

Next, in Figure 5.18a, we show that for a single cilium, as the domain length decreases, we see a decreased in the magnitude of rotation, compared to the longer domain. In Figure 5.18b, this is clearly the case as the particles tend to oscillate in each beat cycle, as time progresses. However, when considering the cilium patch configuration (bottom panels of

Figure 5.18), the magnitude of rotation is markedly increased, where the isometric particles have made a full half rotation by the end of the simulation time frame. Additionally, when the longer domain is longer (Figure 5.18d), the perpendicular elliptical particle shape has plateaued and remains in the orientation switch, whereas the parallel elliptical particle has almost returned to its original (although rotated by 180 degrees) orientation.

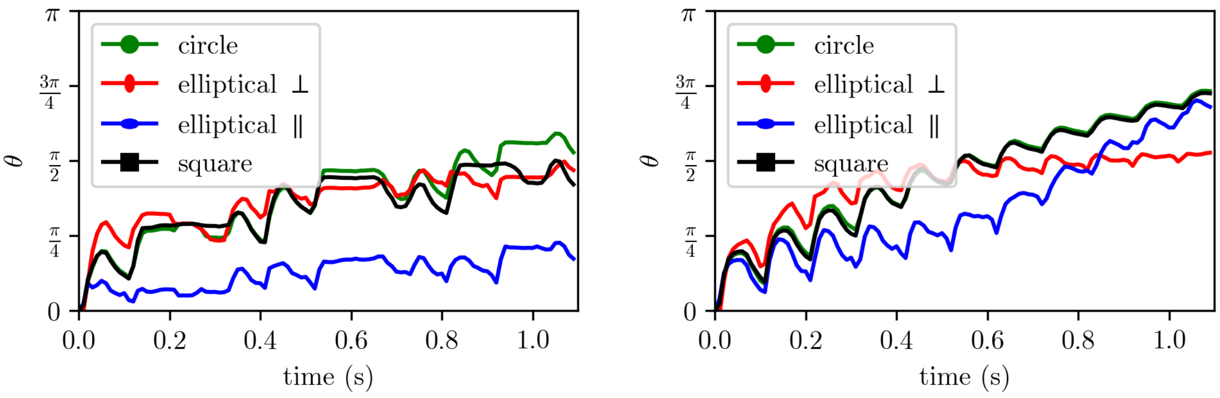

(a) Single cilium, $l_d = 16\mu$m

(b) Singe cilium, $l_d = 80\mu$m

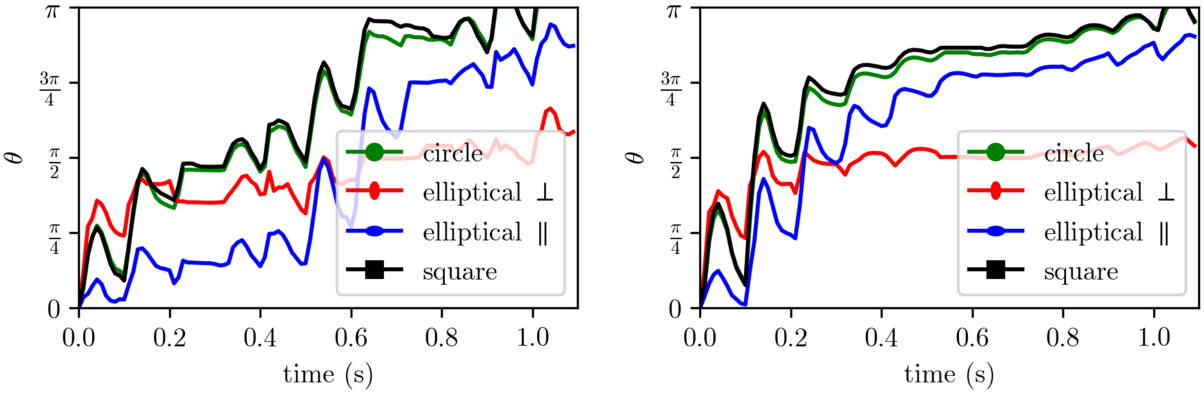

(c) Cilium patch, $l_d = 30\mu$m

(d) Ciliu patch $l_d = 60\mu$m

Figure 5.18: Comparison of rotation angle between the single cilium unit (top panels) and cilium patch (bottom panels), for all particle types. The left hand side images are the closer in domain length, while the right hand side images are shorter in domain length

We now consider parameters for the cilium patch, which are not relevant for the single cilium configuration. First, we analyze the changes in inter-cilium spacing, and plot the two extremes at a length of $l_c = 1 - 6\mu$m in Figure 5.19. These result reveal that the wider spread cilium impact cilium rotation at a greater rate, as most particles have made a full

180 degree rotation by the end of the simulation time, compared with the closer cilium, which have not. Again, we see that the orientation for the perpendicular versus parallel ellipse has switched. Finally, when considering the wavelength, we see that less cooperative cilia (larger wavelength in Figure 5.20a) lead to a smaller rate of rotation, as the particle traverses through the domain, it encounters cilia beating all in phase. However, at the smaller wavelength, which imply the metachronal wave moves faster and therefore neighboring cilia are more out of phase, the rotation rate increases.

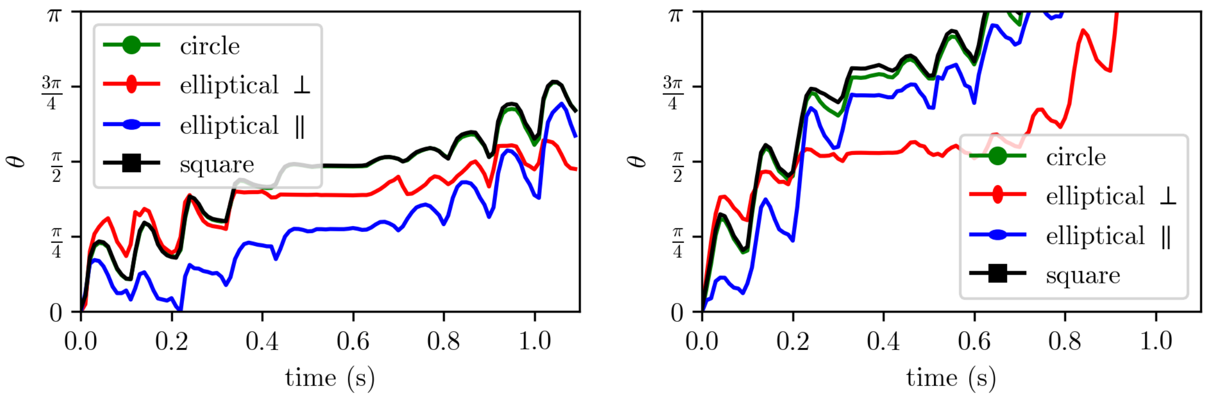

(a) Smallest inter-cilium spacing for cilium patch, $l_c = 1\mu$m.

(b) Largest inter-cilium spacing for cilium patch, $l_c = 6\mu$m

Figure 5.19: Comparison of rotation angle between the extremes of inter-cilium spacing.

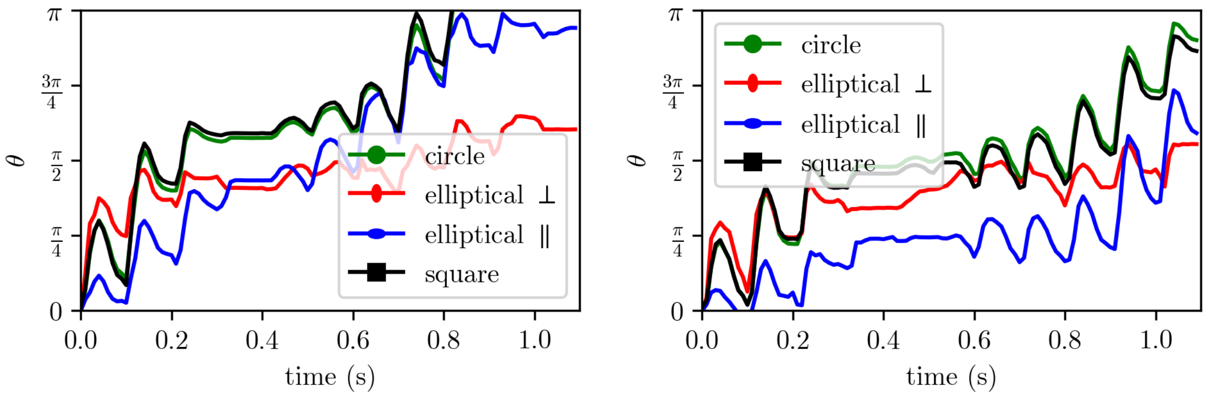

(a) Smallest wavelength for cilium patch, $\lambda = 200\mu$m.

(b) Largest wavelength for cilium patch, $\lambda = 1000\mu$m

Figure 5.20: Comparison of rotation angle between the extremes of metachronal wavelength.

5.3 Discussion and Conclusions

In exposures to asbestos, fiber-glass, or wild-fire smoke, particle shape is of the utmost importance, as these realistic scenarios lead to detrimental health effects. Most work on clearance in the mucosal layer makes an assumption about transport, and in particular, that tracer particles are sufficient to track and model clearance. Of course, when considering flows at such a small scale, the Stokes number is much less than 1 and the Reynolds number is closer to zero, which makes using infinitely small particles a fair assumption. However, at these scales, understanding the effect by which finite-size particles have on transport, would be useful in better understanding clearance of different inhaled aerosols. In this work, we have showed, for the first time, how particles of arbitrary shape are transported in the periciliary layer.

Our research shows several primary conclusions with relation to particle shape. We find that while the shape does not affect the net trajectory, individual particle arc lengths and shapes of trajectories greatly vary. Additionally, when considering the effect that only one single parameter change from our baseline configuration, the trajectories themselves are tremendously different, even if the change is as simple as a small increase in fluid layer height. Perhaps that most striking result is that of the dynamics from non-isometric shapes, as it is closest to reality. In our results, we find that the seed orientation, from the beginning of the simulation, affects particle trajectories. This implies that certain particles could traverse further when deposited in orientations that minimize the drag in the direction parallel to the direction of mucosal clearance. Such results at this microscale have not been reported previously, and we are the first to describe this phenomenon.

Nonetheless, the mucociliary escalator is extremely efficient. When considering particles of equal cross-sectional diameter, differences are not significant. Further, we see that this efficiency is still preserved with a larger domain. Specifically, we see that the net displacement varies linearly with domain length, with a slope of approximately 2μm net displacement per cilium separation, indicating preserved clearance even in the absence of a dense ciliary brush as is experienced *in-vivo*. Thus, in the case of decreased ciliary density as is the case when of patients that are regular smokers [117], the ciliary clearance is still active. However, this is not the only physiological change that occurs, as mucus production is increased and there is "more" to clear. Our investigation of periciliary height changes also confirms this observation, as a lower periciliary height indicates a smaller lubrication region in the realistic scenario. And we indeed see reduced particle transport when decreasing the periciliary height.

Taking these results together with how our daily bodily functions change, we show that the cilia escalator is incredibly resilient to exposures with particle clearance still being effective with smaller cilium patches, but further work is necessary to mimic the *in-vivo* process more accurately. Our key assumptions revolve around working with a uniform Newtonian fluid, which of course is not the case. Additionally, our 2-dimension simulation does not allow to fully explore 3-dimensional metachronal behavior, when in reality, the almost planar beating of individual cilia do not impose these limits. Finally, the most important assumption is regularity of the simulation domain, where our numerical model imposes a periodic flow domain with regularly spaced cilium (or cilium patches). With the exception of only one research study to our knowledge [118], most simulation work takes advantage of the regular repeating behavior of cilium units, as we have done in our study as well. The natural next steps would be to introduce more variability in the numerical modeling approach to study how preserved cooperation is in the absence of repeating units of cilium or patches of cilia. We are actively exploring these areas of research as we attempt to capture more realistic particle clearance and microscale flow characterization.

Chapter 6

Mixing in the periciliary layer

6.1 Introduction

The preceding chapters are primarily interested with clearance of a particle that has deposited in the periciliary layer of the mucosal layer, and is directly above of the cilium or cilium patches. Now, we turn our attention to the flow field characteristics that generate this transport or lack thereof. Specifically, we look to describe mixing in the periciliary layer flow field by visualizing its dynamics in more detail.

The most common description of mixing has been the folding and stretching of fluid parcels as time marches that reduces the diffusion time scale to homogenize the fluid. In realistic scenarios, the process can be very complex and occur at extremely short time scales, such as turbulent mixing from high Reynolds number flows. When working with liquids of similar to water with approximately equal densities, agitation from an external process (such as a spoon stirring morning coffee), is relatively quick. However, in the absence of turbulence, and at very small scales, achieving a well mixed state can be very challenging. Further, for our area of interest, we ask several questions regarding mixing that require more in-depth analysis: Does the periciliary layer fluid achieve a mixed state? If so, at what rate does this occur? Does the description of mixing qualify as chaotic? Without proper analysis tools, and proper mathematical theory, these questions are not easily answerable from traditional flow visualization techniques. The associated mixing process without the aid of turbulence was first termed by Aref [119] as *chaotic advection.* The associated body of research has been successful in helping answering these questions. It is not possible to survey the entire field of literature here, however, for the interested reader an excellent review that captures the earlier methodologies spanning turbulent to microfluidic mixing is given by Ottino [120], and more recently an updated review on the original *chaotic advection* field is given by Aref et al. [121].

This Chapter begins with an introduction to mixing by chaotic advection, which is intended to give the reader a grasp of the complexity of the field by outlining some application areas that help us define more thoroughly some concepts in the area of mixing. Then, we give an outline of the methodologies used to quantify mixing, with special attention to those that will be used in this chapter, specifically in Section 6.1.2. Finally, we close with the importance of mixing in human biological flows and its relevance to human airway particle deposition. In our results, we present several qualitative and quantitative metrics for mixing, but also include an evaluation of numerical methodology since it varies slightly, from that described in preceding chapters. We present differences in periciliary layer mixing for our two main configurations: the single cilium and the single patch configurations. Finally, we conclude this chapter with a discussion of the implication of our results.

6.1.1 Mixing by Chaotic Advection

Whether one considers the transport of the earth's mantle or the chemical reactions occurring at the surface of the human lung epithelium, these fluid dynamical processes all can generate some form of mixing. However, for certain applications, the physical processes involved rid the problem of turbulence due to the extremely slow convection relative to the long length scales. In the case of mixing in the earth's mantle, the length scales associated are in the order of kilometers, but time scales are in the order of thousands of years, and Reynolds number is on the order of 10^{-20}. In the polymer and food production industries, highly viscous fluids tend to dominate, and these macrofluidic applications still have Reynolds number than fall well below the inertial limit ($10^{-10} - 10^{-15}$) [122]. Additionally, fluid rheology adds the energy expenditure to not only move, but also mix the substances [123], making some of these processes very expensive to maintain.

In line with our focus, the communities that study biological fluids and chemical production industries are concerned with length scales that render fluid inertia negligible, or somewhat negligible depending on the specific application. When considering a mixing process, given the variety of problem types, there is considerable impetus for having standard metrics and tools to assess how well a fluid is mixed that are rooted in sound theoretical foundations.

6.1.2 Quantifying Mixing

Despite these complex applications of mixing, one can come up with a simplified description of the mixing process. The simplest description of fluid mixing can be realized by considering mixing two separate fluids dyed with different colors. This process could be pouring one fluid from a container into the other, removing a membrane separating the two fluids, or heating the container of these two fluids. In any case, different dynamics govern the selected process but, nonetheless, the mathematical description can be formulated by considering that we can measure some finite amount of one fluid, and track this finite amount during some characteristic time of the process, and then calculate a quantity the describes how much of each fluid has combined (or remained separate). For fluid dynamicists, the mathematical description of the evolution of this fluid subset (the dye) borrows heavily from dynamical systems theory and, more specifically, we can describe this using the following formulation:

$$\frac{\partial \vec{x}}{\partial t} = v(\vec{x}, t), \quad x \in \mathcal{S}, \quad t \in [t_-, t_+] \tag{6.1}$$

where v is the smooth velocity vector field on a spatial domain $\mathcal{S}$, over some finite time interval $[t_-, t_+]$. In the context of fluid dynamics, this is the equation for the evolution of Lagrangian particle trajectories, that we've called tracers, which have zero inertia and are infinitely small. Then, the flow of "dye" or fluid particles from some time t_0 to t in $[t_-, t_+]$ is defined by the *flow map*,

$$F_{t_0}^{t} =: x(t; t_0, x_0) \tag{6.2}$$

where $x(t; t_0, x_0)$ is the solution of the Lagrangian particle differential equations. Practically speaking, this map defines the position of each Lagrangian particle at the time t at its initial position, which is the subset of fluid dye that we are tracking. At the core, this description utilizes the flow map $F_{t_0}^{t}$ to describe the mixing process both visually and mathematically. From a continuum mechanics perspective, this mathematical description of the flow is akin to following material lines in the continuum and, as such, the deformation tensor is an important quantity that we will see is central to the quantification of mixing. In Figure 6.1, we show two instances in time of one particular flow map from our single cilium simulations. In the following sections, we describe the methods we use to characterize mixing the periciliary layer, and their relevant utilization of this flow map.

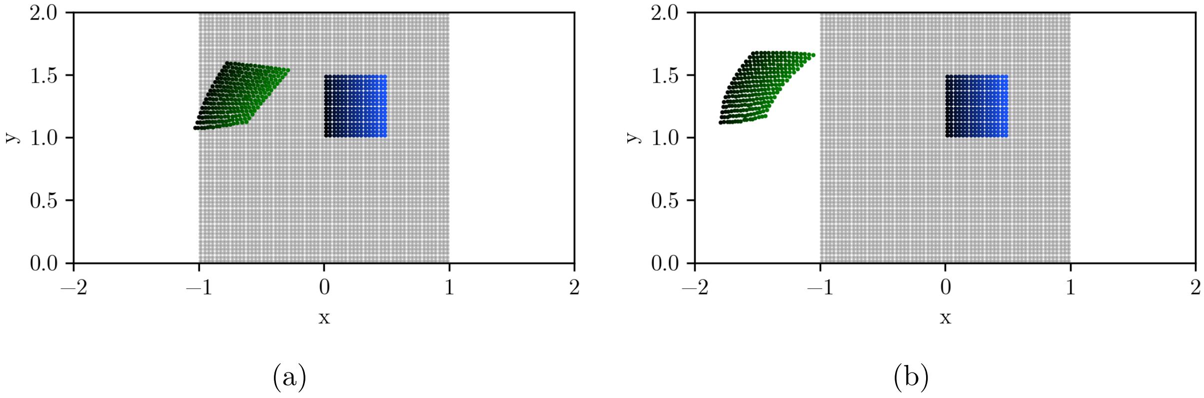

(a) (b)

Figure 6.1: Initial ($t = 12T$) and final particle ($t = 12T - t_0$) positions used in the calculation of the flow map for backward time integration. In 6.1a, the particles are advected backward in time, by two beat periods ($t_0 = 2T$), while in Figure 6.1b, they are advected by four beat periods ($t_0 = 4T$). The gradient colored particles are highlighted only to show a subset of the entire flow domain seeded with grey particles from $x \in [-1, 1]$ and $y \in [0, 2]$, although the entire set of seeded particles are advected.

One of the goals of tracking the fluid with the Lagrangian particle trajectories has been visualization of such processes and extraction of important information regarding the state of the mixed fluid. In this section we present three different metrics, that all utilized the flow map (Eqn. 6.2), and additionally, all give separate but useful information about the state of mixing. In order to gain an understanding of how the flow field changes over time, material lines and their evolution over time can be visualized by calculating the Finite-time Lyapunov exponents of the flow field. The utilization of FTLEs can then be used to precisely extract certain flow structures, but our use is heuristic and provides a useful tool for comparison between other visualization techniques. Another powerful visualization tool developed by Stone and Stone [124] additionally introduces the mixing number used by Ding et al. [109], and its variants more recently by Chateau et al. [110] to quantify the rate of mixing in ciliary flows. However, as we show in Section 6.1.2, the multiscale norm developed in the work of Mathew et al. [125] and examined more recently by Thiffeault [126], allows for metric that reduces its dependence on the resolving the smallest spatial scales. While these three metrics are chosen due to their benefits in extracting information about the flow field, others of course exist that could be utilized which are more common in experimental flows due to the finite resolution of the systems used to capture Lagrangian dyes. In our tests, these three prove sufficient to quantify the state of mixing in the periciliary layer.

Finite-time Lyapunov Exponents

The goal of determining FTLE fields is to identify Lagrangian Coherent Structures, LCS. These LCSs, first defined by Haller and Yuan [127], provide a way to visualize material lines in the flow that *attract*, *repel*, or *shear* particle trajectories (see [128] for an excellent review on LCSs). These material lines correspond to areas of the flow where folding (attracting LCSs), stretching (repelling LCSs), or swirling (shearing LCS). Identification of these LCSs and their time evolution can elucidate complex flow phenomena by their direct visualization and provide more precise quantification of particle transport. We chose to utilize the definition of Shadden et al. [129], however, note that in certain cases this definition can lead to incorrectly defining Lagrangian Coherent Structures [130], even for incompressible flows, where the volume preserving mapping due to divergence free velocity fields exists. Thus our utilization of the FTLE field serves as a tool to qualitatively describe the patterns observed by our other quantification methods.

Following [127] and [129], and utilizing our previous definition of the flow map in Equation 6.2, we describe the growth of a perturbation along a particle trajectory starting at $\vec{x} = \vec{x}_0$ after some time $\Delta t = t_0 + T$, which in time periodic flows can be the characteristic period. The initial perturbation is defined as the distance between the two particles, and for t_0 is, $\Delta\vec{x}(t_0) = \vec{x}_0 + \delta\vec{x}(t_0)$. After time T, the growth in perturbation, $\Delta\vec{x}(\Delta t) = \vec{x}_0 + \delta\vec{x}(\Delta t)$, can be defined in terms of the flow map, $\Delta\vec{x}(\Delta t) = F_{t_0}^{t_0+T}(\vec{x}(\Delta t)) = F_{t_0}^{t_0}(\vec{x}(t_0)) + \delta\vec{x}(\Delta t)$. Solving for the perturbation, we arrive at:

$$\delta\vec{x}(\Delta t) = F_{t_0}^{t_0+T}(\vec{x}(\Delta t)) - F_{t_0}^{t_0}(\vec{x}(t_0)) \tag{6.3}$$

To calculate the magnitude, and therefore growth, of this perturbation, one can linearize and ignore the higher order terms in Equation 6.3, and then calculate the Euclidean norm,

$$\delta\vec{x}(\Delta t) = \delta\vec{x}(t_0)\frac{dF_{t_0}^{t_0+T}(\vec{x}(\Delta t))}{d\vec{x}} + \mathcal{O}(\delta^2\vec{x}(t_0)) \tag{6.4}$$

$$||\delta\vec{x}(\Delta t)|| = \left\langle \delta\vec{x}(t_0), \frac{dF_{t_0}^{t_0+T\,*}}{d\vec{x}}\frac{dF_{t_0}^{t_0+T}}{d\vec{x}}\delta\vec{x}(t_0) \right\rangle^{1/2} = \langle \delta\vec{x}(t_0), C(\vec{x})\delta\vec{x}(t_0)\rangle^{1/2} \tag{6.5}$$

where right Cauchy-Green deformation tensor, $C(\vec{x})$, is positive and definite with real eigenvalues λ_i, where $i = 1...n$ where n is 2 or 3 dimensions. We note that the linearized magnitude of the growth of the initial perturbation, $\Delta\vec{x}(t_0)$, is the Euclidean norm between the initial position of each particle and right Cauchy-Green deformation tensor times at that initial point, which gives a local magnitude of the deformation. To arrive at the FTLE field, we find the maximal stretching that occurs by calculating the eigenvalues and eigenvectors, noting that the determinant of right Cauchy-Green deformation tensor for incompressible flows is 1, with $0 < \lambda_1 < 1 < \lambda_i$. Finally, the FTLE field is:

$$\Lambda_{t_0}^{t}(\vec{x}) = \frac{1}{|T|} \ln \sqrt{\lambda_{\max}(C(\vec{x}))} \tag{6.6}$$

In practice, the FTLE is a scalar field defined on the fluid domain $\mathcal{S}$ formed by calculating the right Cauchy-Green deformation, $C(\vec{x})$, on the flow map, $F_{t_0}^{t}$, finding the eigenvectors of 2×2 matrix $C(\vec{x})$ at each (x, y) point, taking the maximum eigenvalue, and finally using Equation 6.6 at every point in the fluid domain. This simplicity in calculating the FTLE field has lead to its ubiquitous use. The next step in identifying the LCSs using the FTLE field has been disputed, and more recently, Haller [130] have made a distinction between simply using the maximal eigenvalues used here, and instead tracking the rate of *evolution* of the material lines and the material line deformation [131]. While our goal here is to investigate the properties that cilium configuration have on mixing, we can still use the FTLE to heuristically analyze barriers to transport, which is evident with our other two metrics.

The Mixing Number

As we described earlier, the flow map defined in Equation 6.2 requires seeding a relatively dense array of particles in the field of view, and evolve the trajectories over your time of interest. This could lead to conflicting priorities when attempting a design optimization problem. At one end, seeding "just enough" particles in the flow field would lead to faster computation times, on the other, resolving the fine-scale resolution dynamics could exponential increase memory usage and computational times. When considering flow fields from experimental or numerical results, there is an inherent discrete velocity field scale which must be adhered to from limitations to the computational resources or the measuring acquisition hardware. Nevertheless, when working on an optimization problem that seeks to answer how well certain parameters affect the mixed state of a fluid, faster computation times are preferred with insensitivity to spatial and temporal resolutions of computations.

In Stone and Stone [124]'s work on mixing in microfluids, the authors were concerned with efficient computation of the mixing properties that a particular configuration of their micromixer had. Once a method was determined to be viable, with an appropriate metric, the parametric study would be performed, and the state of mixing could be evaluated across configurations. Their method, frames this problem ingeniously by considering the time duality of the forward- and backward-time flow map. Put simply, we summarize the question they posed as follows: if we look at a uniform set of particles at some time $t = T$ seeded in our flow domain $\mathcal{S}$, where must they have originally been in order to arrive at this current location. This framing allowed the authors to conduct an extremely extensive parametric study of many design parameters of a serpentine channel, and gave rise to stunning images of mixing inside of a droplet as it traversed the flow path.

This specific method, and its simplicity, has also been fairly popular in the microfluids community. However, we will note that the authors considered analytical velocity fields, where the position of each seed particle is explicitly given by direct (albeit numerical) integration of the ordinary different equation of the map. This small, but important distinction means that the velocity field introduces no error into the numerical computation of the flow map. In discrete velocity fields from experimental observations, or solutions to the Navier-Stokes equations, there are sources of error from the temporal and spatial resolution of acquiring these solutions. Nonetheless, due to its simplicity, we still view it as a valuable tool, and additionally, we address the differences in error when acquiring the velocity field numerical, as we have done.

To begin, we describe more formally the method used in [124], and its main benefit to the rapid imaging of mixing in time and the calculation of the mixing number. If we take the flow map defined in Equation 6.2, the positions of each individual particle is defined on the original resolution's seed density, (x_i, y_i), and time span ranging from $[t_-, t+]$. Since we are concerned with the initial position at $t = 0$ (and therefore initial dye coloring), Equation 6.2

maps the final positions when integrating backward in time from $t_0 = T$ to $t = 0$, F_T^0. From here, we can subset the the entire flow domain, at $t = 0$, into, for example, two distinct colors of fluids stacked next to each other (center inset in Figure 6.2). Once you have the positions from the flow map at $t = 0$, and have defined the boundaries of the initial coloring, you map that specific coloring to the regularly spaced original resolution for each point, x_i, y_i. This mapping, called by the authors the backward image trace, gives you a regularly spaced resolution image of the coloring distribution, at your integration time mapping, $t = T$ (left inset in Figure 6.2).

From here, one can calculate a type of norm on the distance separating the two subsets of the mapping. We define all the particles belonging to one dye as set $\mathcal{A}$, and all the particles belonging to the other dye as set $\mathcal{B}$. Then, for the distinct colored particles in Figure 6.2, we can define every particle position in each of two sets, as $x_i \in \mathcal{A}$, for $i = 1, .., N$ and $x_j \in \mathcal{B}$, for $j = 1, .., M$, for N particles in set $\mathcal{A}$ and M particles in set $\mathcal{B}$, where $\mathcal{A} \cup \mathcal{B}$ are the total number of particles, $M + N$, in the fluid domain, $\mathcal{F}$. Additionally, we define the operator, $d(x_i, x_j)$, as the distance between a single particle in set $\mathcal{A}$ and a single particle in set $\mathcal{B}$. Finally, we can assemble the mixing number, Equation 6.7, by taking minimum distance between a single particle in set $\mathcal{A}$ and all of the particles in set $\mathcal{B}$, squaring those distances, and averaging over the number of particles in set $\mathcal{A}$

$$m(t) = \sum_{i=1}^{N} \frac{\left(\min_{j \in M}\{d(x_i, x_j)\}\right)^2}{N} \tag{6.7}$$

Conversely, one can do the forward integration problem, and subset the entire flow domain at the initial time. However, as time elapses forward, the material lines that can be identified by LCSs in the flow field will drive particles to be either attracted or repelled from these material lines, diluting the overall image and creating non-uniformed particle locations. Additionally, calculation of a proper mixing rate metric would be polluted by these diluted images. Thus, by using the backwards image trace you can get a non-spatial resolution dependent metric of mixing. In the center inset of Figure 6.2, we show the initial seeding

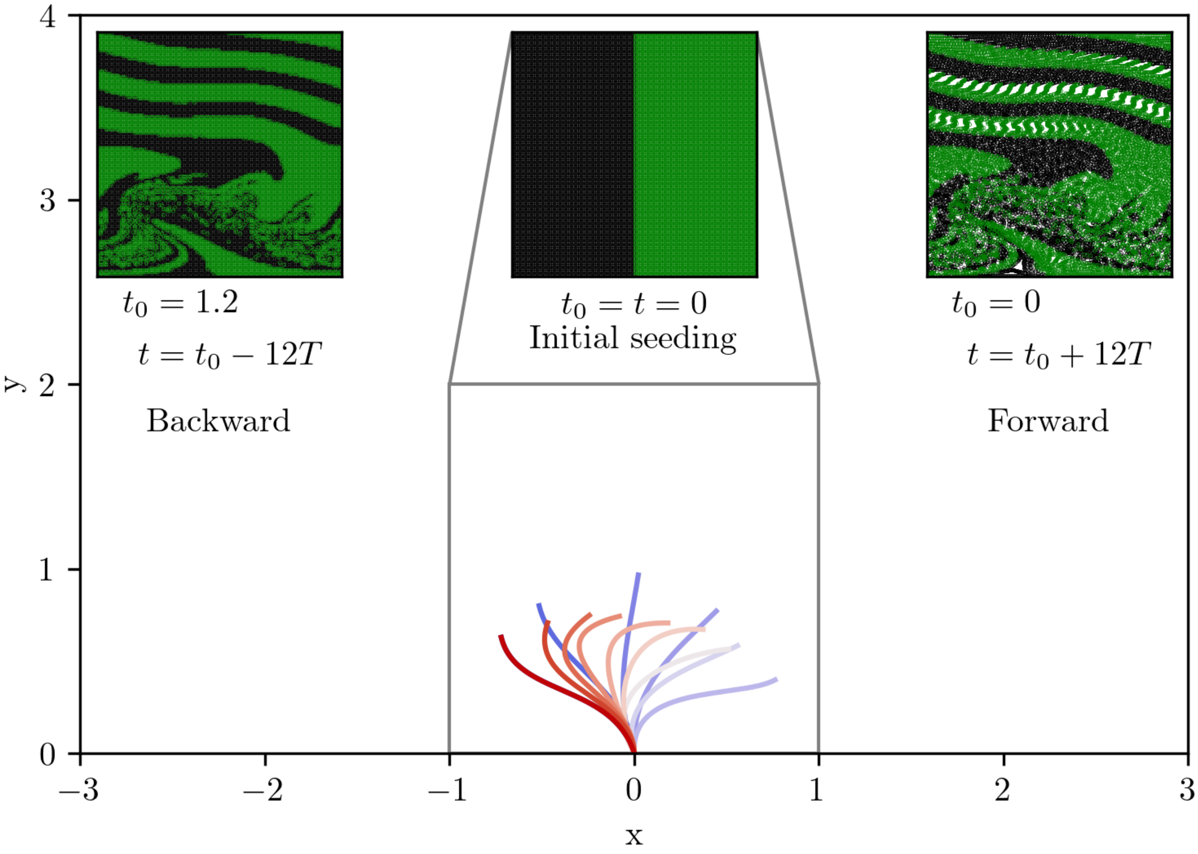

Figure 6.2: Visual representation of the initial locations of particles at $t = 0$ (center inset), the labeling from the backwards in time flow map $F^{t=0}_{t_0=12T}$ (left inset), and the labeling from the forwards in time flow map $F^{t=12T}_{t_0=0}$ (right inset). Single cilium shape shown for one full beat cycle, with forward stroke shown in red, and backward stroke shown in blue.

locations for our single cilium test problem described in Section 3.1. When integrating the Lagrangian velocities for each particle forward in time, and keeping their initial coloring, we would see a disparate image (right inset of Figure 6.2), which shows clearly the benefit of using the backwards image trace. We remark that the seed density here is relatively high, and is limited by the background velocity field, as we will now describe.

However, we pause here to describe the differences between having an analytical description of the velocity field, and a discrete (whether numerical or experimental) one. In their paper, Stone and Stone [124] did successfully showed an independence on the *number* of seeded particles. As they increased their particle density, their calculation of the mixing number converged to a single value. However, the background mesh resolution is infinite, as they had an analytical form for the velocity field. Additionally, their comparisons to other metrics, such as the classical *intensity of segregation*, does show a dependence on the chosen resolution, thus justifying the usage of the backward image trace and subsequent mixing number calculations. Since we do not have an analytical flow field defined at every point, our numerical simulation results depends highly on our choice of Δx and Δt as described in Section 2.3. So, we set out to show that the inclusion of more fine scale dynamics by increasing our time scale undoubtedly affects our mixing number calculations, and subsequent extraction of the rates.

Our goal here is to show the effect that differences in the background velocity mesh resolution as well as the number of particles seeded in the domain have on our resulting mixing number calculations. In Figure 6.3, we set out to show the variation in snapshots that occur when simply increasing the resolution of the background mesh, while keeping the seeded particle density constant (seeded particles match the finest background mesh at a ratio of one particle per mesh point). As is seen from the distinct snapshots, lower resolutions do not fully capture the particle dynamics, and suggests that increased particle density for a fixed mesh size simply does not add any additional information. In Figure 6.4, we perform a thorough evaluation of the mixing number calculations at different seed resolutions and background velocity resolutions from the results of our numerical simulation. As we clearly see, as we increase the number of seeded particles (from left to right), the rate and absolute value of the mixing number decreases by several orders of magnitude, but appears to converge. This is in line with what is reported in [124], since they they performed a convergence study by increasing number of tracers on an infinite resolved background velocity field. Additionally, for a fixed seed tracer resolution, increasing the background mesh resolution has diminishing returns, but is necessary, since an increased mesh resolution reveals more fine scale dynamics as evident from the snapshots in Figure 6.3.

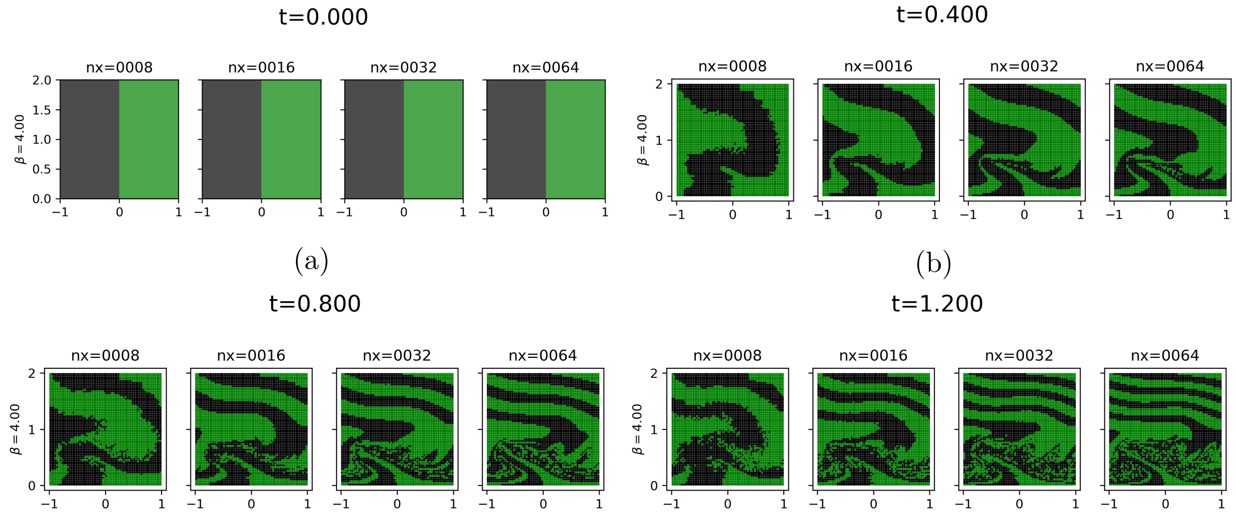

(a) (b) (c) (d)

Figure 6.3: Mixing number snapshots across 12 cilium beat cycles at 4 distinct times. In each panel, we show an increase in background velocity resolution from $\Delta x = \frac{1}{nx}$ for $nx = 8$ to 64. All initial seeding locations are the same, and all numerical simulations are performed at a constant value of viscous CFL $\beta = 0.4096$.

Multiscale Mixing Norm

As we have clearly shown in the previous section, having to resolve such fine scale dynamics to capture the mixing process, and subsequently quantifying can be in some case numerically expensive, and experimentally infeasible. In the work by Mathew et al. [125], a new approach to quantify the mixed state was prompted by reducing the fine scale resolution requirements

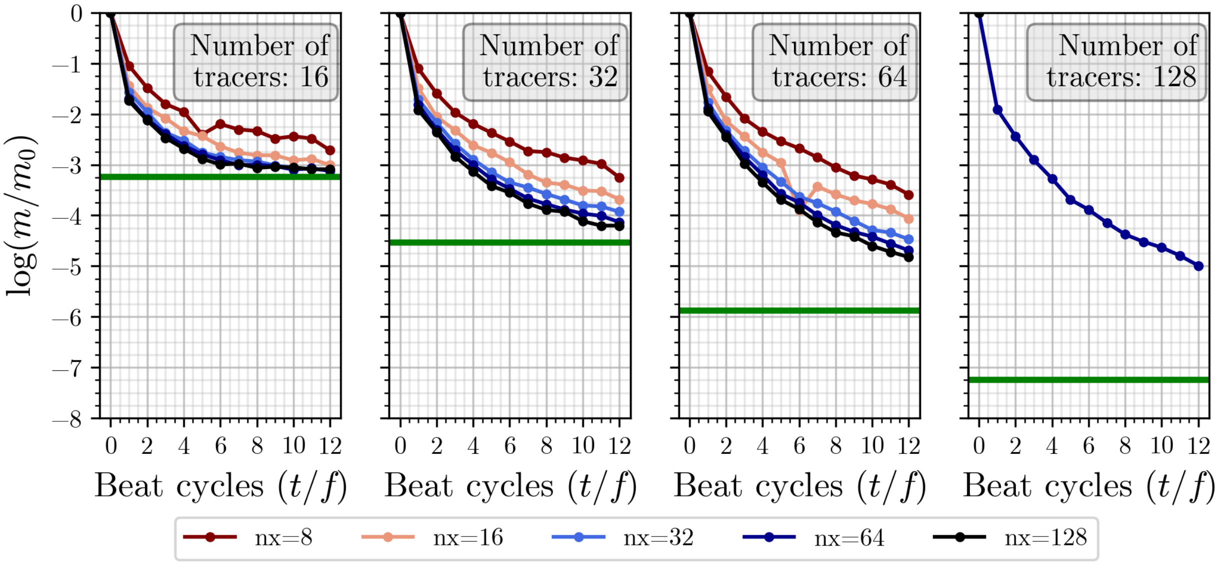

Figure 6.4: Mixing number dependence on initial tracer seed density, and spatial mesh resolution. Each graph, from left to right, shows an increase in the seed density (lower number of tracers, from 16 to 128). Within each graph, the background velocity field spatial mesh resolution is increased, from $\Delta x = \frac{1}{nx} = \frac{1}{8}$ to $\frac{1}{128}$. depicted by the different line colors. Note, we plot the mixing number normalized by the initial value at t_0, namely m/m_0.

which can be resolved but requires long compute times, such as the one presented in the previous section. The method uses many of the same assumptions regarding the evolution of the flow map, but frames the problem using the classical notion of a passively diffusing tracer (and subsequent elimination) to present a novel metric that can be used to smooth out the fine scale dynamics.

We begin this discussion by presenting the classical convective-diffusion equation of some scalar quantity, θ.

$$\frac{\partial \theta}{\partial t} + \vec{u} \cdot \nabla \theta = \kappa \nabla^2 \theta \tag{6.8}$$

This quantity can be thought of as the concentration of some scalar quantity, (dye or chemical) that is advected through the domain by diffusion and convection. $\theta(t)$, in the domain, can be measured and quantified to extract a state of the mixing process. This is analogous to our description of the flow map, with the added complexity of diffusion. In the calculation of the flow map, we assume that the passive tracers are not diffusing. Nonetheless, this description will be revisited when presenting the mix-norm.

In measuring the state of mixing, the variance of concentration could be quantified by evaluating

$$\mathrm{Var}\theta = ||\theta||^2 - \langle\theta\rangle^2 \tag{6.9}$$

where

$$||\theta||^2 = \frac{1}{|\mathcal{F}|}\int_{\mathcal{F}} \theta^2 d\mathcal{F}, \qquad \langle\theta\rangle = \frac{1}{|\mathcal{F}|}\int_{\mathcal{F}} \theta d\mathcal{F} \tag{6.10}$$

This description is the classical *intensity of segregation* described in the previous section, which as was shown in [124], for example, to be scale dependent. This known fact has made quantification of mixing challenging for those practically trying to design optimization processes around mixing. Nonetheless, this metric is useful and has sound theoretical basis for the trend of the variance of θ. For incompressible flows, $\nabla \cdot \vec{u} = 0$, in the absence of concentration sources or sinks (as in our case), it can be showed that the variance, $\mathrm{Var}\theta$, is monotonically decreasing and the first and second moments follow

$$\frac{d}{dt}\langle\theta\rangle = 0, \qquad \frac{d}{dt}||\theta||^2 = -2\kappa||\nabla\theta||^2 \tag{6.11}$$

resulting in the following rate of decay of the variance of the concentration over time

$$\frac{d}{dt}\mathrm{Var}\theta = -2\kappa||\nabla\theta||^2 \tag{6.12}$$

There is a considerable amount of literature on studying the rate of scalar decay, and in particular, we see in Equation 6.12, velocity does not make an appearance directly. This makes tracking the variance a relatively easy task, track a passive diffusing tracer and measure its decay over time to measure mixing. However, this can be difficult when the mixing process occurs rapidly or at such small scales that tracking the rate of decay of variance becomes infeasible. The rate dependence on κ dictates what scales must be resolved in order to track the mixing rate, and for even small scales, the diffusion of this passive scalar can be much much smaller spatially or temporally than those that one wishes or can resolve. Thus we wish to have a scenario that allows us to quantify mixing independently of the diffusion.

We start considering the pure advection equation, by ignoring the effect of the diffusion component, and effectively setting $\kappa = 0$. This is the exact equation describing the *concentration* evolution of our flow map defined in 6.2, only that we had no interest in the concentration gradient, but the deformation gradient instead. Regardless, with this description of passive advection of a scalar, we can continue our measurement of the variance by doing the same process as before.

$$\frac{\partial \theta}{\partial t} + \vec{u} \cdot \nabla \theta = 0 \tag{6.13}$$

This seems problematic at first, since now that means that our decay of variance, Equation 6.12, now equals zero, implying that there is never a mixed state, and the purely advecting concentration field cannot longer be used as to measure of mixing. However, a particular Sobolev norm on the concentration field as proposed by Mathew et al. [125] does allow quantification of mixing. Additionally, using only the advection equation to define mixing is closer to mixing property in ergodic theory. While the mathematical derivation of mixing in the sense of ergodic theory is outside the scope of this dissertation, we point the more mathematically inclined reader to read the review by Thiffeault [126] for a comprehensive derivation, the generalization of the original mix-norm, and its application to flows in the presence of sources and sinks. Finally, we define the multiscale mix norm on a concentration field θ,

$$||\theta||_{\dot{H}^{-1/2}} := ||\nabla^{-1/2}\theta||_2 \tag{6.14}$$

$$||\theta||_{\dot{H}^{-1/2}} = \left(\int_{\mathcal{F}} |(-\nabla^2)^{1/2}\theta|^2 d\mathcal{F} \right)^{1/2} \tag{6.15}$$

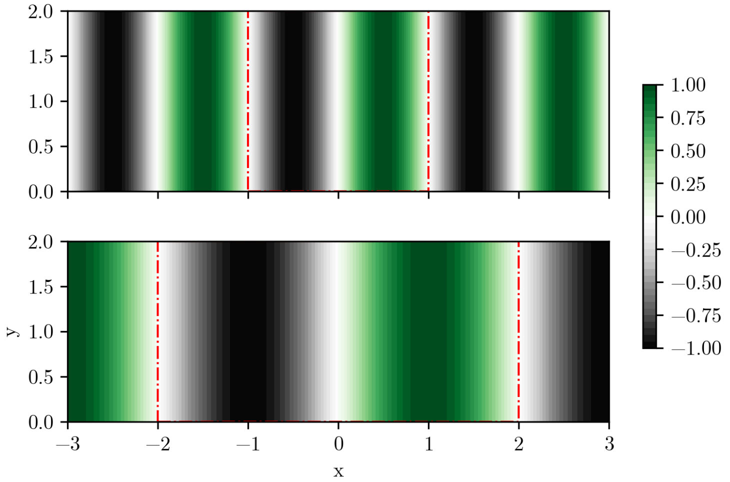

Figure 6.5: Initial concentrations for two separate domain length cases. The top panel shows the domain for 2×2 repeating square with, while the bottom panel shows an increased domain of length 4.

where Equation 6.15 is the homogeneous Sobolev norm on space $\dot{H}^{-1/2}$. We can view this in terms of the Fourier transform of θ, and recast this norm as

$$||\theta||_{\dot{H}^{-1/2}} := \left[\sum_{k} \frac{|\hat{c}_{\mathbf{k}}|}{(1+\pi||\mathbf{k}||^2)^{1/2}}\right]^{1/2} \tag{6.16}$$

where $\mathbf{k}$ corresponds to the wave vectors of the Fourier transform of θ, $c_{\mathbf{k}}$. We note that the initial concentration field must have mean zero for this definition of the norm. In the case of our initial seeding "dyes" from our previous mixing number calculation, the mean of the concentration is indeed zero. However, for calculation of the mixing norm, we adopt the following initial concentration gradient equation

$$\theta(x,y) = \sin\left(\frac{2\pi}{l_d}\right) \tag{6.17}$$

with concentration values of theta ranging from -1 to 1. We can see this visually represented in Figure 6.5. We note that for our calculations, our domain is not square for all cases, but is indeed periodic in the x direction. We mark the domain limits, and the repeating concentrations that are used for calculation of the mix-norm.

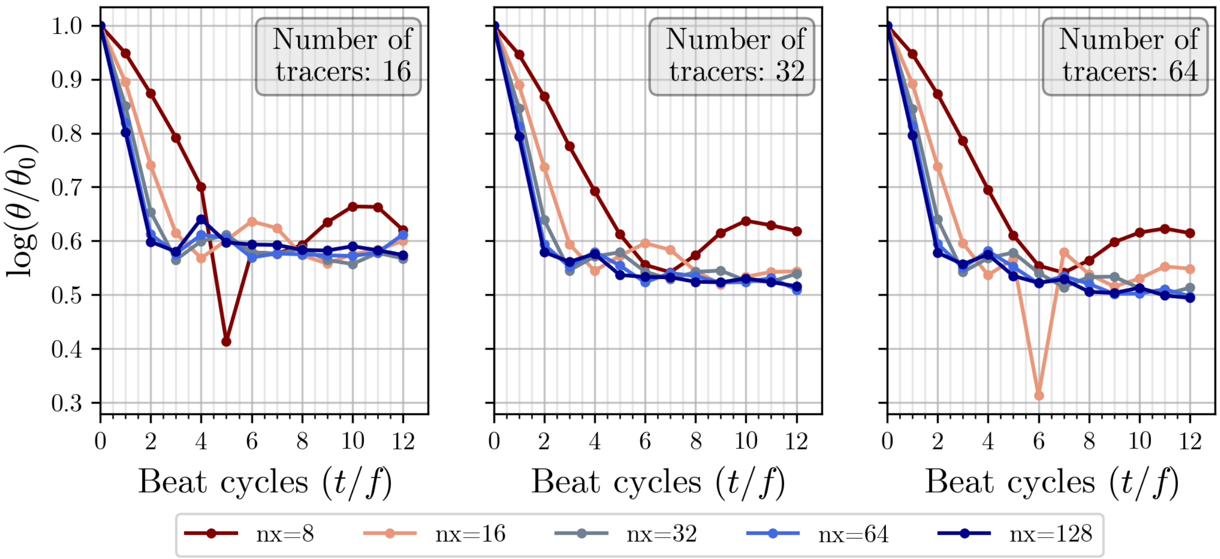

Figure 6.6: Mix-norm dependence on initial tracer seed density, and spatial mesh resolution. Each graph, from left to right, shows an increase in the seed density (lower number of tracers, from 16 to 64). Within each graph, the background velocity field spatial mesh resolution is increased, from $\Delta x = \frac{1}{nx} = \frac{1}{8}$ to $\frac{1}{128}$. depicted by the different line colors. Note, we plot the mix-norm normalized by the initial value at t_0, namely θ/θ_0.

We can now use our test problem to compare the mix-norm to the mixing number from before. In Figure 6.4, we showed that in the absence of the infinitely resolved velocity field, our mixing number calculations are mesh resolution dependent. Now we calculate the mix-norm on those same cases, and as we can see in Figure 6.6, there is significant improvement from the mixing number.

6.2 Methods

Having defined the various measures for mixing, and their corresponding strengths, we now seek to employ these methodologies to analyze more carefully the flow field that is generated by both a single cilium and a patch of cilia. Up until now, we have been utilizing an adaptive mesh refinement strategy in IBAMR to capture the dynamics of particle transport. We now are interested in simultaneously seeding densely infinitely small particles in the flow field. As we showed in Section 6.1.2, visual representations and their corresponding metrics can be dependent on the scale at which the flow map is calculated. Thus, for all calculations presented herein, we make use of the finest mesh found in our verification work that provided reasonable convergence without excessive use of computational time. Our choice for viscous CFL continues to be $\beta = 0.4096$, with a mesh resolution of $\Delta x = \frac{1}{nx} = \frac{1}{64}$, and a time step of $\Delta t = 1 \times 10^{-5}$.

Additionally, we present all visualizations on the 2×2 window which is a subset of the whole periodic domain, centered at the $x = 0$ plane. In the case of our test problem, this corresponded to the center of the domain, and encapsulated the entire flow field. However, for our parametric variations in configuration geometry, the domain need not remain equal along the $x-$ and $y-$directions. Thus in order to compare between an increase in geometric domains, we keep the window constant, and report parameters for that window. This can be visually extract from the Figure 6.2, where the grey box indicates the visualization window, and the whole flow domain be interpreted as being of length l_d and height h_p within the entire domain. In some cases, this window corresponds to the entire flow domain height and length.

6.3 Results

Our goal is to visualize the mixing process over time and quantity the effect that selected parameters (beat frequency, domain length and height, metachronal wavelength, and intercilium spacing) have on the flow field. We seek to answer the following questions:

- How do configuration parameters affect the mixing process over time?
- Is there clear evidence of transport barriers in the flow?
- Does there appear to be chaotic advection in the flow? If so, what parameters promote or prevent this mixing?

In order to answer these questions, we organize our results by first presenting direct visualization of the mixing process via the backward image trace presented in section 6.1.2. These compelling images are then analyzed more carefully heuristically by calculating the FTLE field of the flow. Then, we discuss our findings on chaotic advection by calculating both the mixing number, and the multiscale mix-norm of the passive advection of a scalar. Finally, we present differences in the mixed state for various configuration parameters between a single cilium and a cilium patch.

6.3.1 Transport Barriers in the Periciliary Layer

The results of the mixing process can lead to beautiful captivating images. We present one set of images to show the richness of the mixing process and highlight a few key observations. In Figure 6.7, we show a comparison between the baseline configuration for a single cilium (right panels) and the changes to the periciliary height (left panels). These panels show the time evolution of the mixing process, beginning at the first quarter beat period (first row, leftmost column), and ending at the last period (last row, rightmost column). Since these result depict only a single cilium in a periodic domain, the simple change from increasing the domain height, drastically changes the mixing snapshots, and subsequently the rates. Nonetheless, our goal here is to qualitatively describe this process, and then by use of the FTLE field, gain more insight into the time evolution of this process.

By utilizing the FTLE field, we can heuristically determine transport barriers by extracting information about the Lagrangian Coherent Structures. In Figure 6.8, we see the ridges of the *forward* (or repelling material) FTLE field (denoted by the color bar as green) grow over time and indeed also showcase the areas of highest mixing that are present in the time sequence snapshots in Figure 6.7. When comparing these images to the *backward* (or attracting material lines) FTLE field in Figure 6.9, we see that the there are filaments that emanating from the core mixing region. Taken together, these FTLE fields showcase what happens in the mixing snapshot. Near the base of cilium, fluid is stretching and folding, where the material lines are crossing. However, as time evolves, the magnitude of the FTLE decreases, and the sharpness of the ridges becomes more convoluted, which is why this particular analysis method could lead to incorrectly identifying these ridges. Nevertheless, these can be useful in analyzing the mixing characteristics of the flow field.

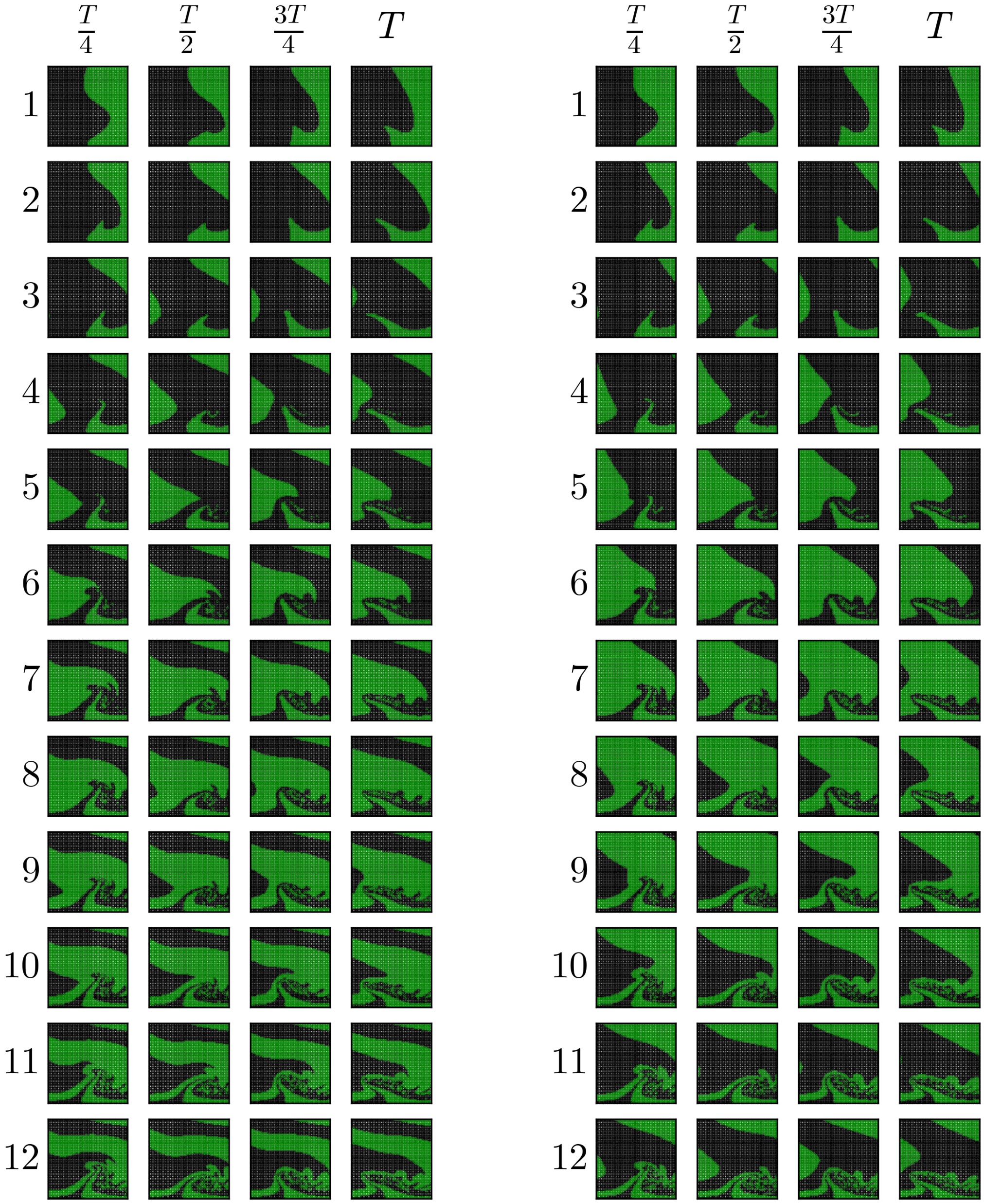

(a) Frequency $f = 10$hz (b) Height $h_p = 40\mu$m

Figure 6.7: Time sequence of two parameters. The left panel set corresponds to the baseline configuration for a single cilium, and the right panel set corresponds to the case when increasing the periciliary layer height h_p.

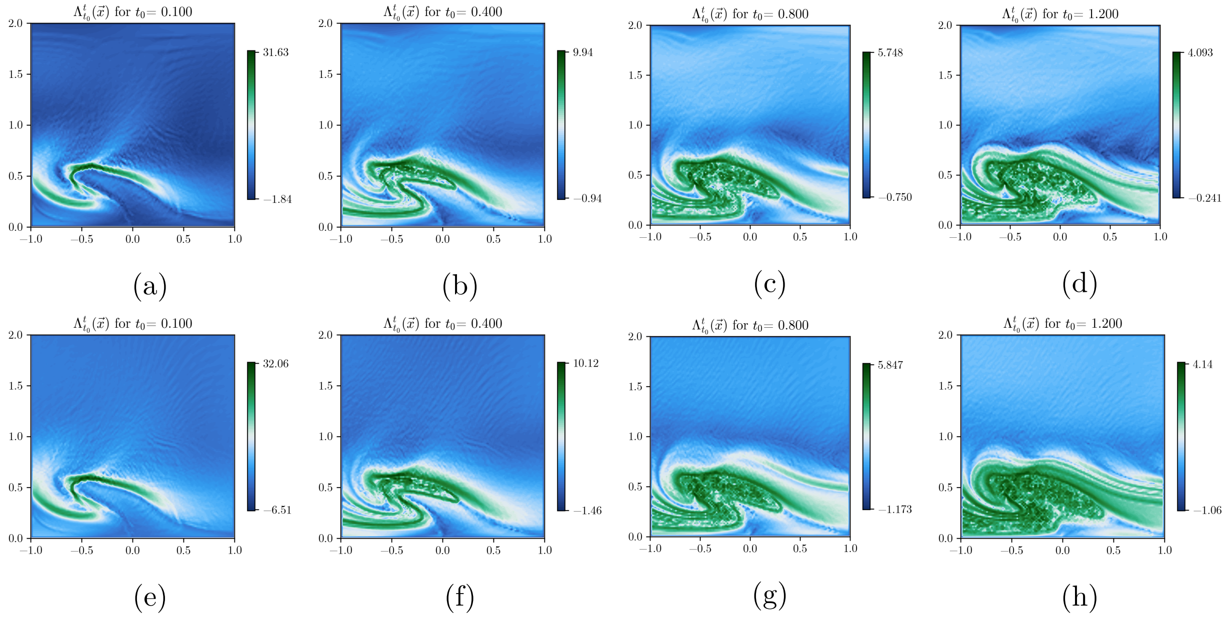

(a) (b) (c) (d)

(e) (f) (g) (h)

Figure 6.8: Forward FTLE field for a single cilium case with the baseline configuration on the top panels, and periciliary height change to $h_p = 40\mu$m on the bottom panels. FTLE is evolved over one beat period, from left starting at $t = T, 4T, 8T$ to $12T$.

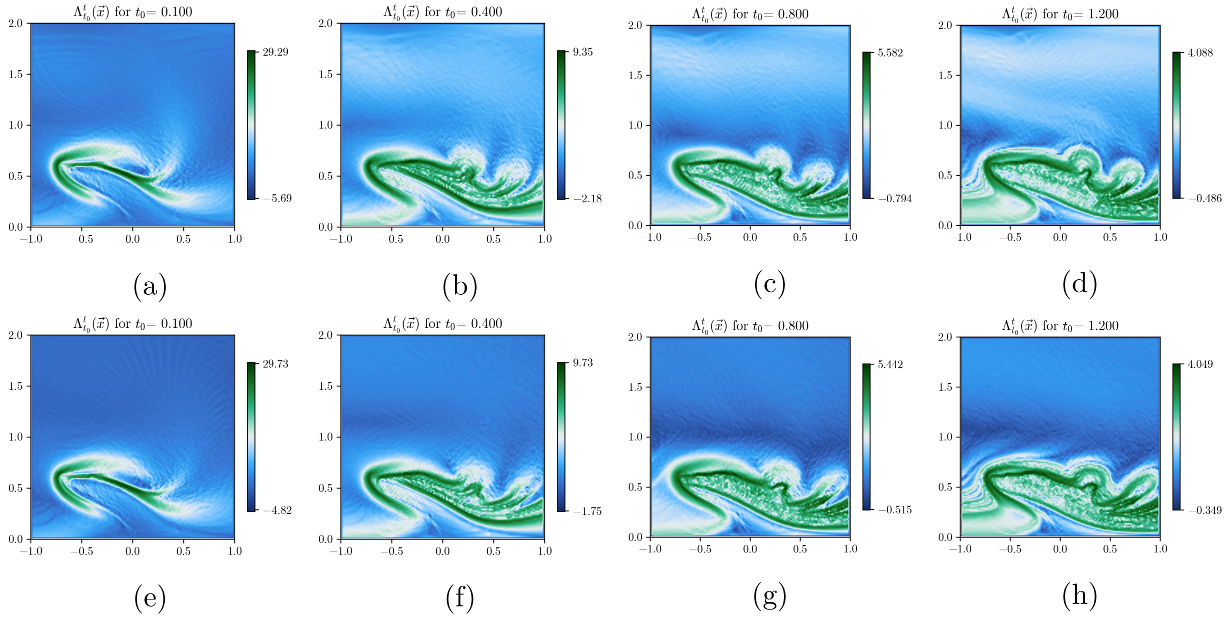

(a) (b) (c) (d)

(e) (f) (g) (h)

Figure 6.9: Backward FTLE field for a single cilium case with the baseline configuration on the top panels, and periciliary height change to $h_p = 40\mu$m on the bottom panels. FTLE is evolved over one beat period, from left starting at $t = T, 4T, 8T$ to $12T$.

One prominent feature that is missing from the FTLE fields, is the filamentous components that arise towards the end of the beat cycle. We reproduce a more pronounced case in

Figure 6.10, which is the equivalent to the test case we used in Section 6.1.2 to explore the fine-scale dependence on mixing number. What is missing in the description of the FTLE field is the emergence and stretching of these areas. However, we point out that we can visualize these areas due to the periodic nature of the problem set up. That is to say, we have an infinitely repeating sequence of black and green dyes, and as such, it is replenished as time moves forward. However, in the calculation of the FTLE field, we do not reintroduce particles in the domain as, technically speaking, the deformation gradient would dramatically increase due to the particle instantly traveling to another point in the domain. Artificially, we could reintroduce these into the domain, and these features would indeed appear, (since the deformation gradient calculates the separation between a point at the right hand side of the domain and one on the left hand side that was just reintroduced) but this change in magnitude would overshadow the core mixing ridges that we see are prominent near the base of the cilium at the domain's center. Nonetheless, taking the forward and back FTLE fields, the appearance of maximal ridges that intersect, along with the images created with the backward image trace method, we can say almost, conclusively say that chaotic mixing occurs in the periciliary layer. In the following section, we are concerned with quantitatively showing this.

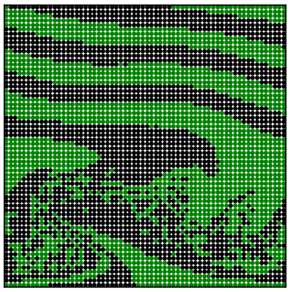

Figure 6.10: Frequency $f = 10$hz, height $h_p = 20\mu$m, domain length $l_d = 20\mu$m

6.3.2 Chaotic Advection

The principal question that we aim to answer in this section is "Is there chaotic advection in the periciliary layer?". While few have attempted to confidently say that chaotic advection occurs [48, 110], others have alluded to the potential existence of chaos [49, 56, 109, 132]. In this section, we aim to show that chaotic advection does exist to a certain degree in this system and, more importantly, only in the vicinity of the cilia.

We first aim compare the difference between the mixing number and the mixing norm, and in particular, we show that the mixing number, while an effective measure in certain scenarios, can lead to over predicting the rate of mixing due to the fine scale resolution requirements of the velocity field. For all the results presented in this section, we present the mixing number or mix-norm, normalized by the initial values at t_0, that is, we plot m/m_0 and θ/θ_0. As a sample case comparison, we first present results for a single cilium over across a range of frequencies which correspond to the top panel in Figure 6.18. From visual inspection, we can see that all three images produce the same results, and thus the mixing number and mixing norm produce the following graphs,

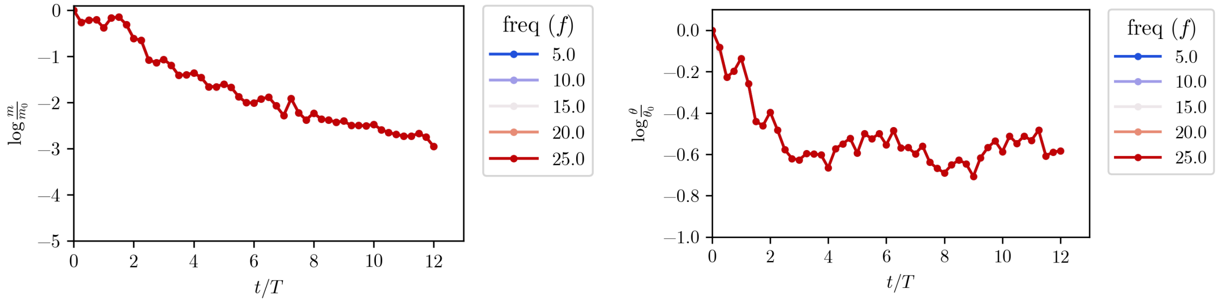

(a) Mixing number

(b) Mixing norm

Figure 6.11: Comparison between the mixing number and mixing norm for a single cilium repeating unit.

which are all unchanging as a function of period.

In this comparison 6.11, we notice that magnitude of the metric is different, but more importantly, the rates behave differently. Although the magnitudes are different, what we are interested in is the estimation of the rate which corresponds to the slope of these lines in comparison another case, not between the mixing number and the mix-norm. The mixing number has a steady decrease is and almost linear, a hallmark of chaotic mixing. On the other hand, we see that the mix-norm has a sharp linear decrease within the first 3-4 periods, followed by what appears to be steady-state condition. When evaluating these results with the mixing time sequence, we can arrive at the following conclusions: 1) the mixing number weighs the fine scale mixing process more heavily than the mix-norm which is evident from the regularity in the rate decrease, and 2) the mix-norm shows the existence of two time scales, the core is mixed rapidly at the beginning, and the stretching but not folding filaments are mixed at a slower time scale.

We further explore this effect by comparing the bottom panel in Figure 6.18, which now show differences in the domain length. In this case, the domain in increased from $l_d = 20 - 100\mu$m. As we can see in the panels, the smaller the domain, the more filaments we see, and the longer the domain, the less filaments emerge. We compare the mixing number to the mixing norm in Figure 6.12. One prominent feature of the mixing number time course is the regularity in the decrease. Additionally, the mixing number for the highest separations are reversed, that is mixing is less effective at a domain length of 60 compared to 80, and then there is a transition at around 6 periods. When inspecting the time course snapshots, this is the point where dye from the periodic domain has been introduced into the measuring window, and thus calculation of the mixing number can underestimated. However, when comparing these results to those of the mix-norm (6.12a), such an effect is non-existent, and in fact, the time at which this occurs corresponds to the beginning of including filaments in the domain, which are quantitatively mixed at a slower rate since there is no folding in that region of the domain (as evidence by the FTLE fields). Additionally, we can see across all 5 domain lengths, that the rapid initial decrease of the mix-norm corresponds to fluid being drawn into the flow domain and subsequent mixing at the cilia core. The much smaller decrease in the mix-norm corresponds to the rate of inclusion of the filaments in the mixing snapshot, which by the time that this occurs, the core mixing region is essentially homogeneous.

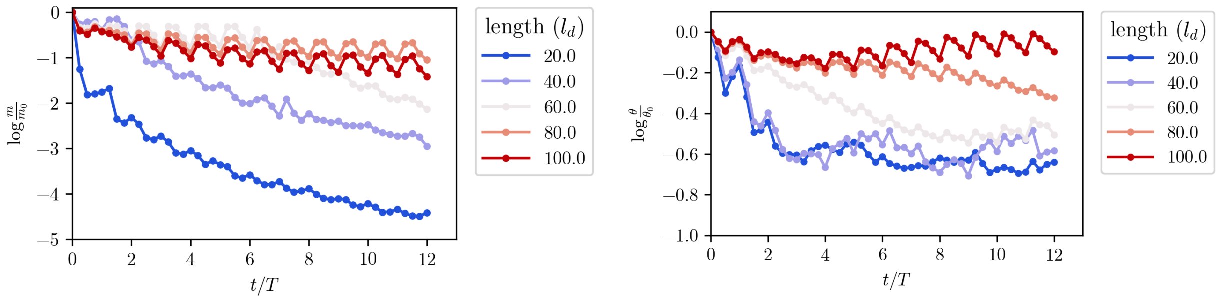

(a) Mixing number

(b) Mixing norm

Figure 6.12: Comparison between the mixing number and mixing norm for a single cilium repeating unit.

Finally, we now can conclusively answer our initial question posed, and with more quantitative evidence, that does not over- or under-estimate the mixing rates. In Figure 6.13, we plot the mixing number and the mix-norm for our final case of comparison, changes in periciliary height, h_p. Inspecting the mixing number, shows a clear picture of chaotic mixing, albeit stratified by less mixing corresponding to higher domain heights. When inspecting the mix-norm, we can see the transient behavior exists again at the beginning with the core homogenization occurring rapidly. We also see the transient inclusion of filament region, being weighed more heavily compared to the mixing number, which are indicated by the large fluctuations in the mix-norm. These mix-norm trends, along with the trends for frequency (Fig. 6.11), and domain length (Fig. 6.12), show the existence of two regions in the periciliary layer, one that is mixed rapidly (the cilium core) and one that is mixed more slowly (filament region above the cilium tip). In our calculation of the FTLE field, the cilium core was clearly delineated. In our calculation of the mixing number, the fine scale mixing rate was overestimated by inclusion of the filamentous region, and in essence averaged upward. In our calculation of the mix-norm, we see the rates of mixing delineated by the first rapid mixing in the core, and then following a longer slower filaments that are stretching in above the cilia tips. Is there chaotic advection? Yes, at the cilium core. Is there chaotic advection across the entire domain? Not always, since the the rate of folding for the filamentous region might not be chaotic.

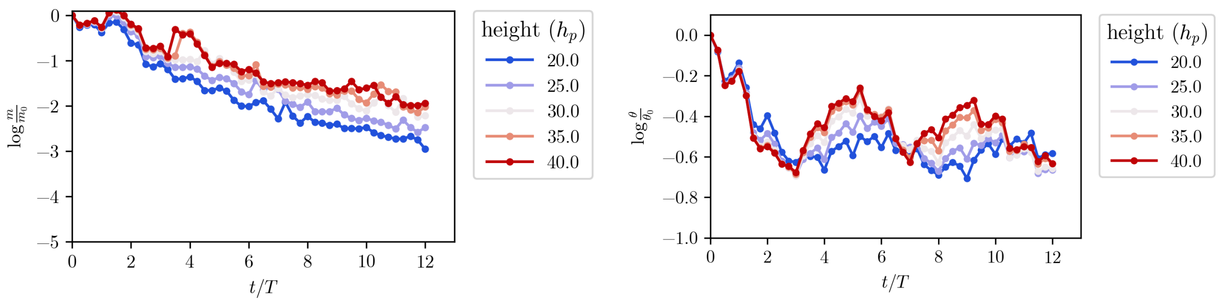

(a) Mixing number

(b) Mixing norm

Figure 6.13: Comparison between the mixing number and mixing norm for a single cilium repeating unit.

6.3.3 Cilium versus Cilia Patch Mixing

In this section, we compare the features of mixing when comparing a single cilium to a cilium patch. We note that in this section, due to the higher number of cilia in the domain for a cilium patch, oscillations during a single beat period are larger in magnitude. Thus we report the mix-norm on a per period basis, instead of the finer resolutions we have been reviewing before. We begin by discussing frequency changes which are plotted in Figure 6.14. The magnitude of the mix-norm decreases very similarly, however in the case of a cilium patch, there is an increase in the rate in the first few beat cycles when compared to a single cilium. This is attributed to the increase in inclusion of filaments in the region above the cilium tips. As was described in Chapter 3.2, the flow rates increased when compared to a single cilium, so there is a net increase of the rate by which fluid is reintroduced into the region above the cilium tips. Additionally, this is seen as a leveling off of the mix-norm after the initial decline.

Next we compare the differences when increasing the domain length. In both the single cilium and the cilium patch configuration, the mixing is increased with a smaller domain. When considering a single cilium, the mixing rate is much faster for when the domain length

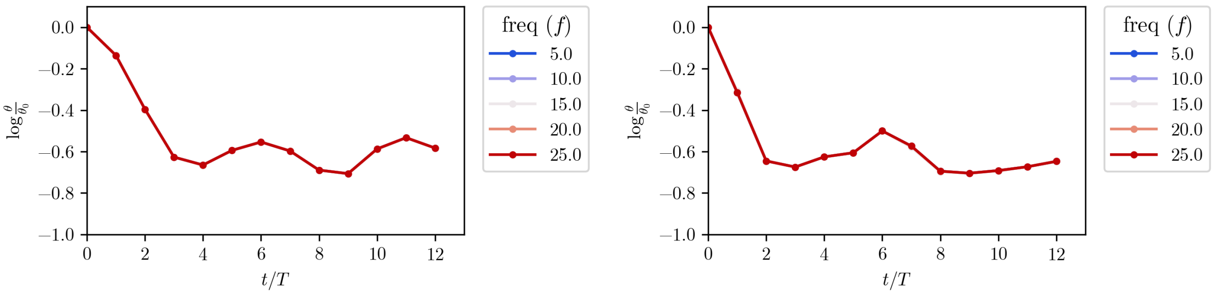

(a) Single cilium (b) Cilium Patch

Figure 6.14: Comparison between of the mix-norm for a single cilium repeating unit and a cilium patch for variation in frequency f.

is decreased, which is attributed to the increase in fluid into the mixing zone. However, as domain length is increased, the mix-norm decreases slower, since all the fluid that has been introduced into the domain has been properly mixed in the core cilium region, and the filament region has not been replenish. We see this process show a smoother transition in the mix-norm rates for a length of $l_d = 60$ μm and higher, as the filament region is slowly replenished, and the initial rapid transients have already mixed the cilium core region, thus only the filament region now contributes to the mix-norm. In the cilium patch configuration, these transition are seen at a finer domain length resolution. In the case of the smaller domain lengths, the transient region occurs very rapidly, whereas in at the higher domain lengths, the filament region dominates the magnitude of the mix-norm as is evidenced by the sharp decrease, and subsequent increase.

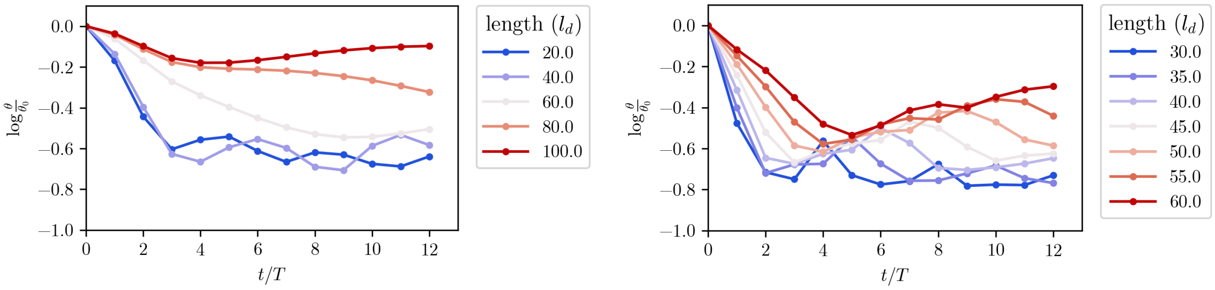

(a) Single cilium (b) Cilium Patch

Figure 6.15: Comparison between of the mix-norm for a single cilium repeating unit and a cilium patch for variation in domain length l_d.

Moving on to our last comparison between between a single cilium and a cilium patch, we present results when periciliary height is varied. In all cases, both the single cilium and cilium patch, we see the initial transient dominating the mix-norm. Later in the process, the observed oscillations are attributed to replenished fluid into the filament region. However, since the cilium patch clears fluid at a faster rate compared to the single cilium, the magnitude of the last peak in the last 4 beat cycles in Figure 6.16 is much lower as seen when comparing the last two snapshots in Figure 6.18 and Figure 6.19, corresponding to a periciliary height of $h_p = 40\mu$m. Additionally, the initial mixing transient is much faster in the case of a cilium patch compared to the single cilium, which is expected. However, it is important to note that again, in all cases, the height does not play a prominent role in affecting the mix-norm, as indicated by the periodic collapse of the mix-norm as time evolves.

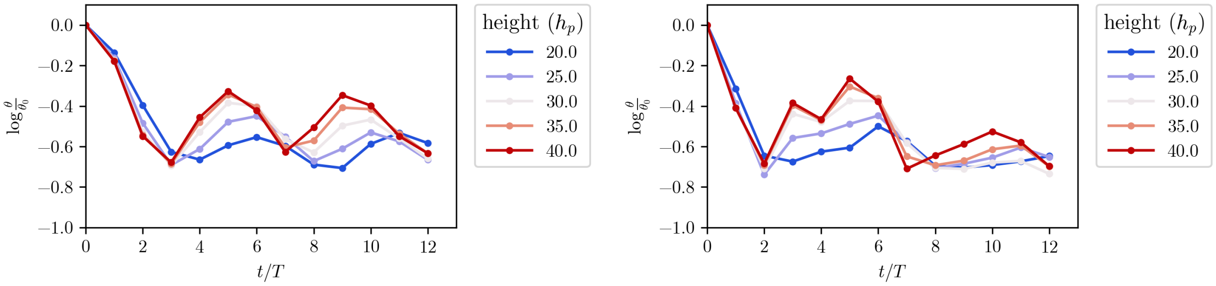

(a) Single cilium

(b) Cilium Patch

Figure 6.16: Comparison between of the mix-norm for a single cilium repeating unit and a cilium patch for variation in periciliary layer height h_p.

In our final analysis of the mixing in periciliary layer, we present changes to wavelength and inter-cilium spacing. The metachronal wave regime is in the higher end of the spectrum thus we expected to find little changes to the mix-norm. Unlike in the case of finite-sized particle clearance, the mix-norm metric does capture the temporal shift of reintroduction of fluid to the filament region, albeit by a spatial shift in the metachronal wave. As is clearly seen in Figure 6.17a, the second peaks from the filament region stretching is only temporal shifted. Interestingly, the core mixing region near the cilium patch seems unaffected by the wavelength. When considering the inter-cilium spacing in a patch, however, we see this same temporal shift once again. This is of course due to the dependence of phase lag between cilia on wavelength and spacing. Nonetheless, this effect is accentuated at smaller spacing, since the phase lag is smaller. As we increase the cilium spacing and effectively increase the phase lag, the effect of the filament region is attenuated, which is indicated by a reduction in the peaks in Figure 6.17b for $l_d > 4.0\mu$m. In fact, when considering the panels in Figure 6.19 for inter-cilium collectively, the difference in the core mixing region is when there is a higher inter-cilium spacing begins to ‘bleed’ into the filament region.

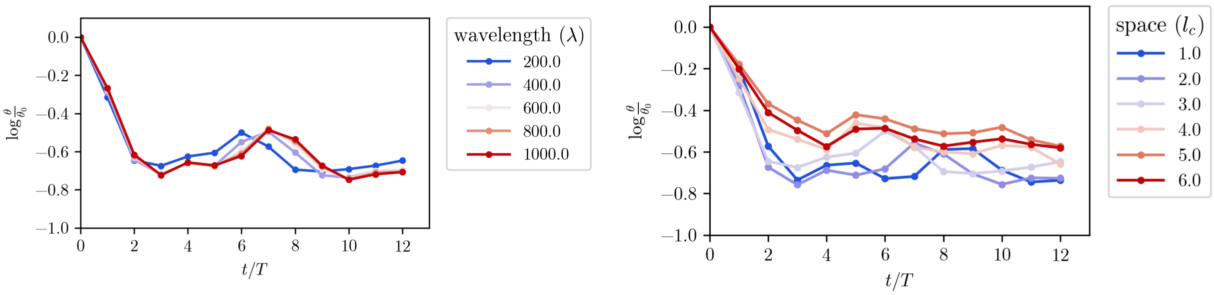

(a) Metachronal wavelength λ

(b) Inter-cilium spacing

Figure 6.17: The mix-norm for a cilium patch for variation in metachronal wavelength λ and inter-cilium spacing l_c.

6.4 Discussion and Conclusions

Mixing in the periciliary layer contributes to several important physiological functions. Particles with sizes that are in the nanoscale range and are potentially harmful must be absorbed by the immunological defense mechanism at the lumen of the tracheal wall. Additionally, cells that secrete important biological markers that communicate with neighboring cells must be transported (by diffusion or with chaotic advection) over several cell-width lengths. It is still an open question as to whether cilia communicate through hydrodynamic interactions or whether there are chemical markers that help them coordinating across distances that are orders of magnitude larger than their length. Thus, it was the aim of this chapter to give a

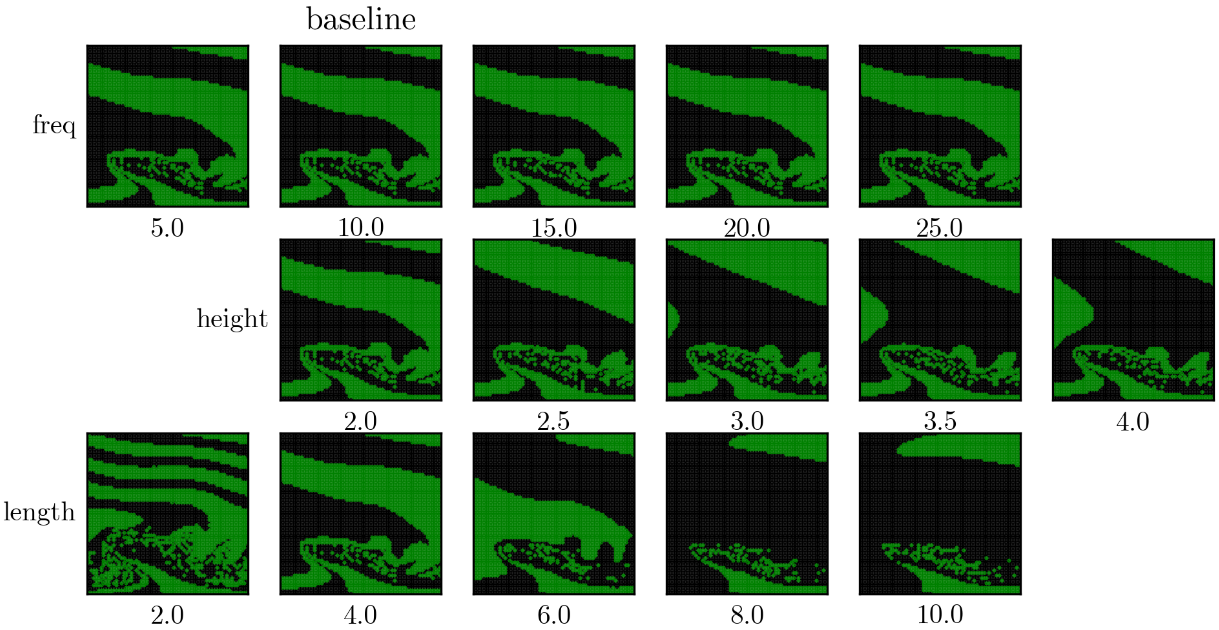

Figure 6.18: Mixing state for all parameters considered in the single cilium configuration after 12 beat periods ($t = 12T$). Each row is ordered by increasing parameter value, indicated by the number below the image. Top row corresponds to changes in frequency (f), middle row corresponds to changes in periciliary height (h_p), and bottom row corresponds to changes in domain length (l_d). Baseline configuration is indicated by the label "baseline" and corresponds to that particular column.

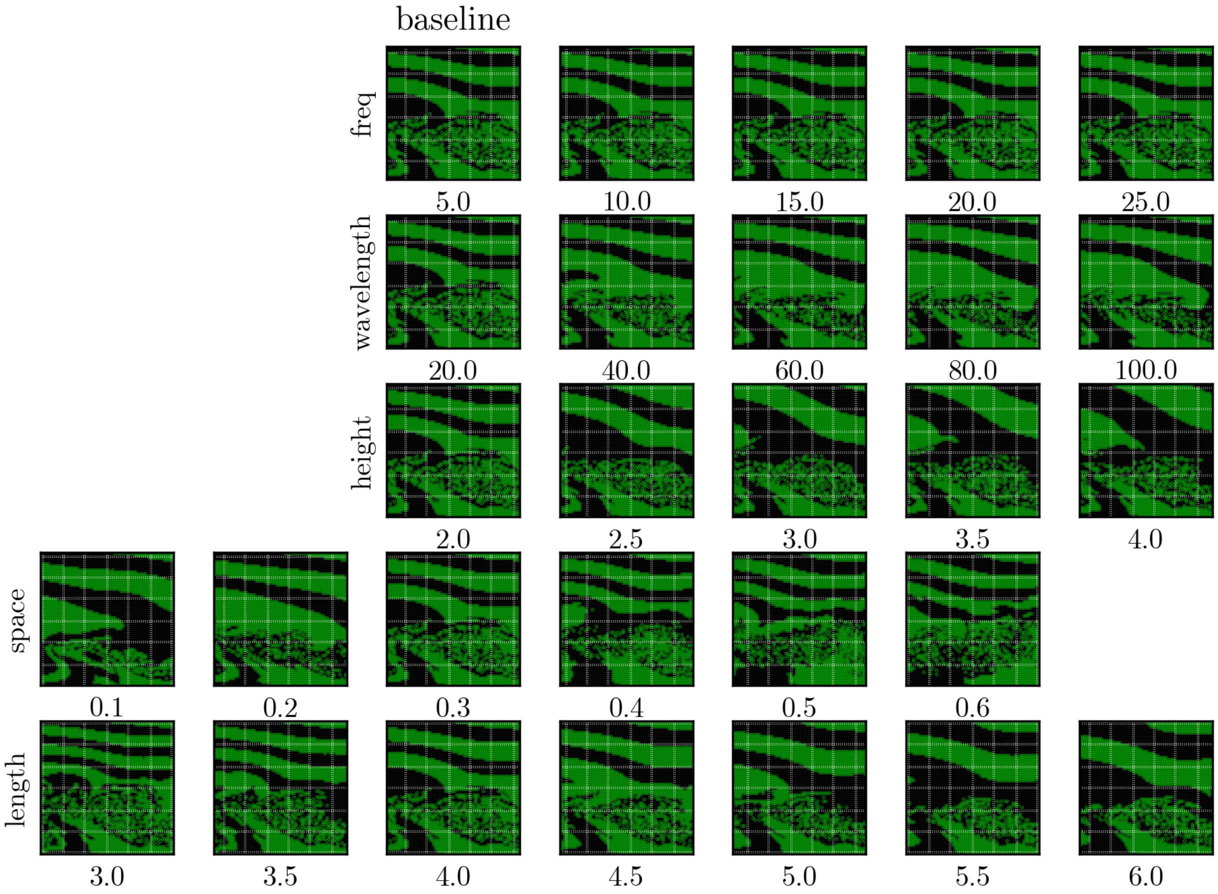

Figure 6.19: Mixing state for all parameters considered in the cilium patch configuration after 12 beat periods ($t = 12T$). Each row is ordered by increasing parameter value, indicated by the number below the image. First row corresponds to changes in frequency (f), second row corresponds to changes in wavelength (λ), third row corresponds to changes in periciliary height (h_p), fourth row corresponds to changes in neighboring cilia spacing height (l_c), and fifth row corresponds to changes in domain length (l_d). Baseline configuration is indicated by the label "baseline" and corresponds to that particular column.

more quantitative description of mixing in the periciliary layer in response to changes that may occur in the presence of disease or acute exposures to inhaled aerosols.

In this chapter, we have systematically varied a series of physical and geometric parameters affecting the rates at which transport occurs in the periciliary layer, and quantified the effects that these changes have on mixing. In our model, we considered the mucus layer an immovable wall at a distance above the beating cilia, and carefully analyzed the whole flow field dynamics. We have conclusively shown that mixing in the periciliary layer is indeed chaotic, and the influence of chaotic advection appears to be segregated into two distinct regions, the core mixing region near the cilium base, and a stratified filament region above the cilium tips. By use of the finite-time Lyapunov exponents field and visualization using the backward image tracing method, we were able to distinguish between these two layers. With the calculation of the multiscale mixing norm, we were able to distinguish how each of these layers affects mixing. More specifically, these two delineated rates are apparent when viewing the mix-norm and the backward image traces together.

The largest effect on mixing came from having cilia closely packed together. This is no surprise, since it has long been known that ciliary function requires densely packed cilia that all coordinately beat in synchrony to propel a mucus layer towards the throat. However, we defined "closely packed" in two different manners, inter-cilium spacing, and domain length. Using both definitions, mixing was improved, however, their effects on mixing in the filaments region was different. When considering domain length, the filament region was less disturbed, whereas when considering cilia that were more spread apart, the mixing core area's influence extended further into the filament region. These results together could be of importance in the case of sparse cilia distributions, such as in reduced cilia density due to smoking, where communication between cilia via the periciliary chemical concentrations would be affected.

It is our hope that this research contributes to producing a clearer picture of mixing in the periciliary layer. Although some, but very few, studies have considered mixing at this scale in this biological system, none have explore the parametric range in such detail as has been done here. Additionally, the use of the multiscale mix-norm provides a much needed update to the mixing rate quantification, since numerical simulations are not of infinite resolution and precision. Although some mixing rates have been quantified as a result of changes in cilia phase lag, we provide a more comprehensive evaluation of the rest of the cilium configuration parameters, including the geometric considerations. Finally, our research conclusively shows that mixing in the periciliary layer is chaotic, and indeed much faster in the region closer to the cilia epithelium.

Chapter 7

Conclusions and Future Work

7.1 Conclusions and Contributions

Throughout this body of work, several important contributions have been made to the field of cilia-particle interactions in the upper airway. We summarize these contributions in order of they were discussed in this dissertation.

—Particle clearance by a single cilium: The effect that a single repeating cilium unit has on the clearance was studied in detail. In our numerical simulation model, the existence of a no-slip wall boundary condition significantly changes the flow reversal characteristics during a single beat cycle. In most published work, boundaries are viewed as infinite, due to the underlying methodologies. Additionally, it has been previously shown that the metachronal wave is primarily responsible for breaking the flow reversal. To our knowledge, this is the first time that this same effect has been shown by the inclusion of this boundary condition. The inclusion of this type of boundary condition is important in cases where mucosal transport has been essentially halted due to underlying disease conditions.

Additionally, we showed that there exists a difference in transport when modeling finite-sized circular particles as tracer particles. Most notable was the complex trajectories that lead to increased arc-lengths measurements. However, the net displacement remains effectively unchanged when comparing both tracers and circular finite-sized particles. This finding reinforces our current knowledge of the cilia beat shape's effective clearance in the mucosal layer. In this simulation model, each cilium is beating in sync, and at the same frequency as its neighbor. This provides the least amount of cooperation, and indeed, the particle clearance mechanism still functions with great efficiency.

—*Particle clearance by cilium patches:* We increased the complexity of our model by defining a subset of cilia within a simulation domain that allows to mimic the "patchiness" that is observed *in-vivo*. This parameter, cilium patch fraction was varied between 10% and 60% in order to capture the realistic ranges in the tracheobronchial tree. We showed that when controlling the patch fraction with increased cilia spacing, the arc-length increased faster than when simply decreasing the domain to space cilia more closely. This effect however, did not carry on to net-displacement, as the effect of varying cilium spacing and domain length were essentially equivalent. Additionally, of interest was the different paths that particles travel through when increasing periciliary height. Particles traveled further with periciliary height increases, almost as if they were skipping above the cilia in the larger domain instead of being confined within a narrower flow domain.

—*Arbitrary particle shape clearance:* The consideration of the influence of particle shape on clearance had some of the most interesting results when considering non-isometric particle shapes. To our knowledge, we are the first to document numerical simulations that considers particle shape differences in their clearance. We made a sizeable contribution to this area of research given the variety of particle shapes that are potentially inhaled. We find that matching the aerodynamic resistance diameter via an area per unit length scale, removes variability between only isometric particles. This finding becomes less important when considering non-isometric particles, as is the case with an elliptical cross-section. By analyzing the rotation rate over the translation path, we see that particles tumble throughout the domain in a non-intuitive fashion. While the matched square and circle particles tend to behave similarly, the elliptical particles rotate and align their minor axis with the flow for longer duration in some cases. In other cases, the particle becomes rotationally stagnant for the duration of the path. These effects ultimately show divergent differences in particle trajectories *and* net displacements, none of which were previously shown with isometric particles.

—Chaotic advection in the periciliary layer: Probably the most visually stunning findings are included in the exploration of mixing by beating cilia. We aimed to show that mixing in the periciliary layer was chaotic, and indeed, we show that there are two regions of chaotic mixing, one above the cilia tips, and one spanning individual cilium bases. We utilized 3 metrics that aid in the identification of mixing, and one that aids in its visualization. The use of the Finite-time Lyapunov Exponent identifies Lagrangian Coherent structures in the flow. With the aid of the backward image trace, we show the emergence of a filament region, and a core mixing region. By using the mixing number and the multiscale mix-norm, we distinguish the rates of mixing in these two areas, and show that the flow is chaotic indeed.

7.2 Future Work

In our work, we have made a number of assumptions that were appropriate for our model development, however the model itself leaves much that can be done to improve and expand our understanding of the conclusions we have provided. First, and foremost, a non-Newtonian model would be the natural next step. In fact, very few studies have considered mixing in the presence of non-Newtonian fluids. Even more challenging is the interaction that particles and non-Newtonian fluids have. There is much left to be explore in the area of building a more relevant fluid model for human airway clearance. This endeavor, however, is not only relevant for our numerical methodology since experimental quantification of mucus is also a vibrant area of research. Building a fluid model that incorporates experimental results from mucus would be a much needed research need.

In this dissertation, we restricted the flow domain to 2-dimensions and, as such, the model problem can be viewed as an infinite array of cilia packed closely enough together that they form a sheet. Additionally, this simplification implies the infinite cylindrical nature of particles seeded in the flow domain, regardless of whether they are elliptical in cross section or square-like. This simplification introduces finite inertia, and potentially over-predicts effects seen with finite-sized particle transport. In many of the studies that consider 3-dimensional domains, additional assumptions are made, and increases in inertial effects are included to speed up computation times (as we have done here to a small degree). Research improvements to the numerical modeling techniques are ever advancing, and could significantly aid in the development of more realistic 3-dimensional models. In our modeling framework, it would be certainly possible to include 3-dimensional affects, albeit for sizeable increase in computational effort. Additionally, particles of equal aerodynamic resistance diameter using the volume equivalent, instead of an area equivalent per unit length would be definitely more realistic.

On the subject of particle transport the particles considered had regular shapes. This of course was a first step to modeling the clearance of finite-sized particles. Nonetheless, our modeling framework is shape independent, which was the primary benefit of using the immersed boundary method, and more specifically, the constraint-based version in IBAMR. In our work, it would be a simple exercise to create a new particle shape, say a long slender rod with rounded corners or the same shape but with sharp corners, in order to get a first estimate of the differences between the dynamics of these two shapes. However, particulate matter also tends to form aggregates or chains that span longer lengths. Considering these morphologies would be more challenging. Additionally, we did not prescribe a cilia-particle interaction model specifically. That is, no cilia came in contact with a seeded particle. This would be necessary in order to include larger and more complex particle shapes. Since the current model does not have any bending rigidity, a new model would relax the fully rigid cilium beat shape, and include a particle-cilium contact model. However, we note that the underlying cilia beat shape mechanics is one of the major challenges still giving rise to controversy. Several hypotheses have been put forth and a number of models have been developed. The question: “How do cilia know how to beat?” stands to be one of the most promising research directions in not only the respiratory field but in all of biological fluids.

Finally, our identification of Lagrangian Coherent Structures by use of the FTLE field is heuristic at best. Although our results show indeed the existence of attracting and repelling material lines, explicit calculation of these was not performed. While the FTLE field use is ubiquitous, and our calculations follow one of the most popular methodologies, it stands to say that new, more rigorous methods exist, such as the minimal stretching of geodesics developed by Haller and Beron-Vera [131], to extract more precisely and mathematically the material lines. With the current implementation of the flow map, calculating these more accurate material lines would be a question of time and patience.

References

[1] Walter F. Boron and Emile L. Boulpaep. *Medical Physiology, 2e Updated Edition*. Elsevier Health Sciences, 2012. ISBN 1455711810.

[2] Robert F. Phalen and Otto G. Raabe. The evolution of inhaled particle dose modeling: A review. *Journal of Aerosol Science*, 99:7–13, September 2016.

[3] Robert Esworthy. Air quality: EPA's 2013 changes to the particulate matter (PM) standard. Technical Report R42934, Library of Congress, Congressional Research Service, 2013.

[4] Hussein Traboulsi, Necola Guerrina, Matthew Iu, Dusica Maysinger, Parisa Ariya, and Carolyn J. Baglole. Inhaled pollutants: The molecular scene behind respiratory and systemic diseases associated with ultrafine particulate matter. *International Journal of Molecular Sciences*, 18(2), 2017. ISSN 1422-0067.

[5] Federico Karagulian, Claudio A. Belis, Carlos Francisco C. Dora, Annette M. Prüss-Ustün, Sophie Bonjour, Heather Adair-Rohani, and Markus Amann. Contributions to cities' ambient particulate matter (pm): A systematic review of local source contributions at global level. *Atmospheric Environment*, 120:475–483, 2015.

[6] Ki-Hyun Kim, Ehsanul Kabir, and Shamin Kabir. A review on the human health impact of airborne particulate matter. *Environment International*, 74:136–143, 2015.

[7] Thomas Ferkol and Dean Schraufnagel. The Global Burden of Respiratory Disease. *Annals of the American Thoracic Society*, 11(3):404–406, March 2014.

[8] Estimated Prevalence and Incidence of Lung Disease. Technical report, American Lung Association, May 2014.

[9] C Kleinstreuer and Z Zhang. Laminar-to-turbulent fluid-particle flows in a human airway model. *International Journal of Multiphase Flow*, 29(2):271–289, February 2003.

[10] Zhe Zhang and Clement Kleinstreuer. Laminar-to-turbulent fluid–nanoparticle dynamics simulations: Model comparisons and nanoparticle-deposition applications. *International Journal for Numerical Methods in Biomedical Engineering*, 27(12):1930–1950, 2011.

[11] Clement Kleinstreuer and Yu Feng. Computational analysis of non-spherical particle transport and deposition in shear flow with application to lung aerosol dynamics—a review. *Journal of Biomechanical Engineering*, 135(2), 6/21/2021 2013.

[12] Jinxiang Xi, JongWon Kim, and Xiuhua April Si. Effects of nostril orientation on airflow dynamics, heat exchange, and particle depositions in human noses. *European Journal of Mechanics - B/Fluids*, 55:215–228, January 2016.

[13] Haribalan Kumar, Merryn H Tawhai, Eric A Hoffman, and Ching-Long Lin. The effects of geometry on airflow in the acinar region of the human lung. *Journal of Biomechanics*, 42(11):1635–1642, August 2009.

[14] Michael A Sleigh, John R Blake, and Nadav Liron. The Propulsion of Mucus by Cilia. *American Review of Respiratory Disease*, 137(3):726–741, March 1988.

[15] Barbara Young, Geraldine ODowd, and Phillip Woodford. *Wheater's Functional Histology - 6th Edition.* elsevier.com. ISBN 9780702047473.

[16] James D Crapo, Brenda E Barry, Peter Gehr, Marianne Bachofen, and Ewald R Weibel. Cell Number and Cell Characteristics of the Normal Human Lung1–3. *American Review of Respiratory Disease*, June 1982.

[17] Hyun-Chul Choi, Christine Seul Ki Kim, and Robert Tarran. Automated acquisition and analysis of airway surface liquid height by confocal microscopy. *AJP: Lung Cellular and Molecular Physiology*, 309(2):L109–L118, July 2015.

[18] Mark A Chilvers and Christopher O'Callaghan. Analysis of ciliary beat pattern and beat frequency using digital high speed imaging: comparison with the photomultiplier and photodiode methods. *Thorax*, 55(4):314–317, April 2000.

[19] L Gheber and Z Priel. Extraction of cilium beat parameters by the combined application of photoelectric measurements and computer simulation. *Biophysical Journal*, 72 (1):449–462, January 1997.

[20] H Matsui, S H Randell, S W Peretti, C W Davis, and R C Boucher. Coordinated clearance of periciliary liquid and mucus from airway surfaces. 102(6):1125–1131, September 1998.

[21] M J Sanderson and Michael A Sleigh. Ciliary activity of cultured rabbit tracheal epithelium: beat pattern and metachrony. *Journal of Cell Science*, 47(1):331–347, February 1981.

[22] Brian Button, Seiko F Okada, Charles Brandon Frederick, William R Thelin, and Richard C Boucher. Mechanosensitive ATP Release Maintains Proper Mucus Hydration of Airways. *Science signaling*, 6(279):ra46–ra46, June 2013.

[23] Robert Tarran, Brian Button, and Richard C Boucher. Regulation Of Normal And Cystic Fibrosis Airway Surface Liquid Volume By Phasic Shear Stress. *Annu. Rev. Physiol.*, 68(1):543–561, January 2006.

[24] Yuye Ling, Xinwen Yao, Ute A Gamm, Emilio Arteaga Solis, Charles W Emala, Michael A Choma, and Christine P Hendon. Ex vivo visualization of human ciliated epithelium and quantitative analysis of induced flow dynamics by using optical coherence tomography. *Lasers in Surgery and Medicine*, 49(3):270–279, March 2017.

[25] Duncan F. Rogers. Mucociliary dysfunction in copd: effect of current pharmacotherapeutic options. *Pulmonary Pharmacology & Therapeutics*, 18(1):1–8, 2005.

[26] Nico Derichs, Byung-Ju Jin, Yuanlin Song, Walter E Finkbeiner, and A S Verkman. Hyperviscous airway periciliary and mucous liquid layers in cystic fibrosis measured by confocal fluorescence photobleaching. *FASEB journal : official publication of the Federation of American Societies for Experimental Biology*, 25(7):2325–2332, 07 2011.

[27] Rajat Ghosh, Gavin A Buxton, O Berk Usta, Anna C Balazs, and Alexander Alexeev. Designing Oscillating Cilia That Capture or Release Microscopic Particles. *Langmuir*, 26(4):2963–2968, February 2010.

[28] Ximena M Bustamante-Marin and Lawrence E Ostrowski. Cilia and Mucociliary Clearance. *Cold Spring Harbor Perspectives in Biology*, 9(4):a028241, April 2017.

[29] David J Smith, E A Gaffney, and J R Blake. A Model of Tracer Transport in Airway Surface Liquid. *Bulletin of Mathematical Biology*, 69(3):817–836, 2007.

[30] D J Smith, E A Gaffney, and J R Blake. Modelling mucociliary clearance. *Respiratory Physiology & Neurobiology*, 163(1–3):178–188, November 2008.

[31] John Blake. A model for the micro-structure in ciliated organisms. *Journal of Fluid Mechanics*, 55(1):1–23, September 1972.

[32] John R Blake and Michael A Sleigh. Mechanics of Ciliary Locomotion. *Biological Reviews*, 49(1):85–125, February 1974.

[33] S M Ross and S Corrsin. Results of an analytical model of mucociliary pumping. *Journal of Applied Physiology*, 37(3):333–340, September 1974.

[34] G R Fulford and J R Blake. Muco-ciliary transport in the lung. *Journal of Theoretical Biology*, 121(4):381–402, August 1986.

[35] J Hussong, N Schorr, J Belardi, O Prucker, J Rühe, and J Westerweel. Experimental investigation of the flow induced by artificial cilia. *Lab on a Chip*, 11(12):2017–2022, 2011.

[36] Edgar C Kimmel, James E Reboulet, and Robert L Carpenter. A typical path model of tracheobronchial clearance of inhaled particles in rats. *Toxicology and Industrial Health*, 17(5-10):277–284, June 2001.

[37] Jessica M Oakes, Miriam Scadeng, Ellen C Breen, G Kim Prisk, and Chantal Darquenne. Regional distribution of aerosol deposition in rat lungs using magnetic resonance imaging. *Annals of biomedical engineering*, 41(5):967–978, May 2013.

[38] Jessica M Oakes, Ellen C Breen, Miriam Scadeng, Ghislain S Tchantchou, and Chantal Darquenne. MRI-based measurements of aerosol deposition in the lung of healthy and elastase-treated rats. *Journal of Applied Physiology*, 116(12):1561–1568, June 2014.

[39] Jessica M Oakes, Philipp Hofemeier, Irene E Vignon-Clementel, and Josué Sznitman. Aerosols in healthy and emphysematous in silico pulmonary acinar rat models. *Journal of Biomechanics*, 49(11):2213–2220, July 2016.

[40] Youbing Yin, Jiwoong Choi, Eric A Hoffman, Merryn H Tawhai, and Ching-Long Lin. A multiscale MDCT image-based breathing lung model with time-varying regional ventilation. *Journal of Computational Physics*, 244:168–192, July 2013.

[41] Sorin M Mitran. Metachronal wave formation in a model of pulmonary cilia. *Computers & Structures*, 85(11–14):763–774, 2007.

[42] A.M. Siddiqui, N. Manzoor, K. Maqbool, A.B. Mann, and S. Shaheen. Magnetohydrodynamic flow induced by ciliary movement: An application to lower respiratory track diseases. *Journal of Magnetism and Magnetic Materials*, 480:164 – 170, 2019. ISSN 0304-8853.

[43] D J Smith, E A Gaffney, and J R Blake. A Viscoelastic Traction Layer Model of Muco-Ciliary Transport. *Bulletin of Mathematical Biology*, 69(1):289–327, 2006.

[44] Robin Chatelin and Philippe Poncet. A Hybrid Grid-Particle Method for Moving Bodies in 3D Stokes Flow with Variable Viscosity. *SIAM Journal on Scientific Computing*, 35(4):B925–B949, 2013.

[45] Robin Chatelin and Philippe Poncet. A parametric study of mucociliary transport by numerical simulations of 3D non-homogeneous mucus. *Journal of Biomechanics*, pages –, 2016.

[46] Robin Chatelin, Dominique Anne-Archard, Marlène Murris-Espin, Marc Thiriet, and Philippe Poncet. Numerical and experimental investigation of mucociliary clearance breakdown in cystic fibrosis. *Journal of Biomechanics*, 53:56–63, February 2017.

[47] Dominique Anne-Archard, Robin Chatelin, Marlène Murris-Espin, David Sanchez, Marc Thiriet, Alain Didier, and Philippe Poncet. *Modeling Cystic Fibrosis and Mucociliary Clearance*. Academic Press, 2017. ISBN 978-0-12-804595-4.

[48] S Chateau, J Favier, U D'Ortona, and S Poncet. Transport efficiency of metachronal waves in 3D cilium arrays immersed in a two-phase flow. *Journal of Fluid Mechanics*, 824:931–961, July 2017.

[49] Hanliang Guo, Janna Nawroth, Yang Ding, and Eva Kanso. Cilia beating patterns are not hydrodynamically optimal. *Physics of Fluids*, 26(9):091901, September 2014.

[50] P G Jayathilake, Zhijun Tan, D V Le, H P Lee, and B C Khoo. Three-dimensional numerical simulations of human pulmonary cilia in the periciliary liquid layer by the immersed boundary method. *Computers & Fluids*, 67:130–137, August 2012.

[51] W L Lee, P G Jayathilake, Zhijun Tan, D V Le, H P Lee, and B C Khoo. Muco-ciliary

transport: Effect of mucus viscosity, cilia beat frequency and cilia density. *Computers & Fluids*, 49(1):214–221, October 2011.

[52] Josephine Ainley, Sandra Durkin, Rafael Embid, Priya Boindala, and Ricardo Cortez. The method of images for regularized stokeslets. *Journal of Computational Physics*, 227(9):4600–4616, 2008.

[53] Hanliang Guo and Eva Kanso. A computational study of mucociliary transport in healthy and diseased environments. *European Journal of Computational Mechanics*, July 2017.

[54] Robert H Dillon, Lisa J Fauci, Charlotte Omoto, and Xingzhou Yang. Fluid Dynamic Models of Flagellar and Ciliary Beating. *Annals of the New York Academy of Sciences*, 1101(1):494–505, April 2007.

[55] Robert H Dillon and Lisa J Fauci. An Integrative Model of Internal Axoneme Mechanics and External Fluid Dynamics in Ciliary Beating. *Journal of Theoretical Biology*, 207(3):415–430, December 2000.

[56] Sarah Lukens, Xingzhou Yang, and Lisa Fauci. Using Lagrangian coherent structures to analyze fluid mixing by cilia. *Chaos: An Interdisciplinary Journal of Nonlinear Science*, 20(1):017511, March 2010.

[57] Tony S Yu, Eric Lauga, and A E Hosoi. Experimental investigations of elastic tail propulsion at low Reynolds number. *Physics of Fluids*, 18(9):091701, September 2006.

[58] Eric Lauga. Propulsion in a viscoelastic fluid. *Physics of Fluids*, 19(8):083104, August 2007.

[59] J C Chrispell, L J Fauci, and M Shelley. An actuated elastic sheet interacting with passive and active structures in a viscoelastic fluid. *Physics of Fluids*, 25(1):013103, January 2013.

[60] A. J. T. M. Mathijssen, D. O. Pushkin, and J. M. Yeomans. Tracer trajectories and displacement due to a micro-swimmer near a surface. *Journal of Fluid Mechanics*, 773: 498–519, May 2015.

[61] David Saintillan and Michael J. Shelley. Emergence of coherent structures and large-scale flows in motile suspensions. *Journal of The Royal Society Interface*, 9(68):571–585, 2012.

[62] Srinivas Hanasoge, Peter J. Hesketh, and Alexander Alexeev. Microfluidic pumping using artificial magnetic cilia. *Microsystems & Nanoengineering*, 4(1):11, 2018.

[63] Dongeun Huh, Wei Gu, Yoko Kamotani, James B Grotberg, and Shuichi Takayama. Microfluidics for flow cytometric analysis of cells and particles. *Physiological Measurement*, 26(3):R73, 2005.

[64] H A Stone, A D Stroock, and A Ajdari. ENGINEERING FLOWS IN SMALL DEVICES. *Annual Review of Fluid Mechanics*, 36(1):381–411, January 2004.

[65] Dino Di Carlo. Inertial microfluidics. *Lab on a Chip*, 9(21):3038–3046, 2009.

[66] John Veysey and Nigel Goldenfeld. Simple viscous flows: From boundary layers to the renormalization group. *Reviews of Modern Physics*, 79(3):883–927, 07 2007.

[67] Alison L Marsden. Simulation based planning of surgical interventions in pediatric cardiology. *Physics of Fluids (1994-present)*, 25(10):–, 2013.

[68] Mathieu Bottier, Marta Peña Fernández, Gabriel Pelle, Daniel Isabey, Bruno Louis, James B Grotberg, and Marcel Filoche. A new index for characterizing micro-bead motion in a flow induced by ciliary beating: Part II, modeling. *PLoS computational biology*, 13(7):e1005552, July 2017.

[69] Mathieu Bottier, Sylvain Blanchon, Gabriel Pelle, Emilie Bequignon, Daniel Isabey, André Coste, Estelle Escudier, James B Grotberg, Jean-François Papon, Marcel

Filoche, and Bruno Louis. A new index for characterizing micro-bead motion in a flow induced by ciliary beating: Part I, experimental analysis. *PLoS computational biology*, 13(7):e1005605, July 2017.

[70] M Ryser, A Burn, Th Wessel, M Frenz, and J Rička. Functional imaging of mucociliary phenomena. *European Biophysics Journal*, 37(1):35–54, April 2007.

[71] Yuri Bazilevs, Kenji Takizawa, and Tayfun E. Tezduyar. *Computational Fluid–Structure Interaction: Methods and Applications.* John Wiley & Sons, Ltd., 2013.

[72] Rajat Mittal and Gianluca Iaccarino. Immersed Boundary Methods. *Annual Review of Fluid Mechanics*, 37(1):239–261, 2005.

[73] Ricardo Cortez. The method of regularized stokeslets. *SIAM Journal on Scientific Computing*, 23(4):1204–1225, 2001.

[74] Hanliang Guo, Hai Zhu, and Shravan Veerapaneni. Simulating cilia-driven mixing and transport in complex geometries. *Physical Review Fluids*, 5(5):053103–, 05 2020.

[75] Hassan Masoud and Alexander Alexeev. Harnessing synthetic cilia to regulate motion of microparticles. *Soft Matter*, 7(19):8702–8708, 2011.

[76] Amitabh Bhattacharya, Gavin A Buxton, O Berk Usta, and Anna C Balazs. Propulsion and Trapping of Microparticles by Active Cilia Arrays. *Langmuir*, 28(6):3217–3226, February 2012.

[77] Charles S Peskin. Flow patterns around heart valves: A numerical method. *Journal of Computational Physics*, 10(2):252–271, October 1972.

[78] Charles S Peskin. The immersed boundary method. *Acta Numerica*, 11:479–517, 2002.

[79] Amneet Pal Singh Bhalla, Boyce E Griffith, and Neelesh A Patankar. A Forced Damped Oscillation Framework for Undulatory Swimming Provides New Insights into

How Propulsion Arises in Active and Passive Swimming. *PLoS computational biology*, 9(6):e1003097, June 2013.

[80] Christina Hamlet, Lisa J. Fauci, and Eric D. Tytell. The effect of intrinsic muscular nonlinearities on the energetics of locomotion in a computational model of an anguilliform swimmer. *Journal of Theoretical Biology*, 385:119–129, 2015.

[81] Thomas Dombrowski, Shannon K. Jones, Georgios Katsikis, Amneet Pal Singh Bhalla, Boyce E. Griffith, and Daphne Klotsa. Transition in swimming direction in a model self-propelled inertial swimmer. *Physical Review Fluids*, 4(2):021101–, 02 2019.

[82] Arvind Santhanakrishnan, Shannon K. Jones, William B. Dickson, Martin Peek, Vishwa T. Kasoju, Michael H. Dickinson, and Laura A. Miller. Flow structure and force generation on flapping wings at low reynolds numbers relevant to the flight of tiny insects. *Fluids*, 3(3), 2018. ISSN 2311-5521.

[83] S. K. Jones, R. Laurenza, T. L. Hedrick, B. E. Griffith, and L. A. Miller. Lift vs. drag based mechanisms for vertical force production in the smallest flying insects. *Journal of Theoretical Biology*, 384:105–120, 2015.

[84] Amneet Pal Singh Bhalla, Rahul Bale, Boyce E Griffith, and Neelesh A Patankar. Fully resolved immersed electrohydrodynamics for particle motion, electrolocation, and self-propulsion. *Journal of Computational Physics*, 256:88–108, January 2014.

[85] Amneet Pal Singh Bhalla, Rahul Bale, Boyce E Griffith, and Neelesh A Patankar. A unified mathematical framework and an adaptive numerical method for fluid–structure interaction with rigid, deforming, and elastic bodies. *Journal of Computational Physics*, 250:446–476, October 2013.

[86] Anup A Shirgaonkar, Malcolm A MacIver, and Neelesh A Patankar. A new mathematical formulation and fast algorithm for fully resolved simulation of self-propulsion. *Journal of Computational Physics*, 228(7):2366–2390, April 2009.

[87] R Glowinski, T W Pan, T I Hesla, and D D Joseph. A distributed Lagrange multiplier/fictitious domain method for particulate flows. *International Journal of Multiphase Flow*, 25(5):755–794, August 1999.

[88] N A Patankar. A formulation for fast computations of rigid particulate flows. 2001.

[89] Boyce E Griffith. IBAMR: An adaptive and distributed-memory parallel implemntation of the immersed boundary method. `https://ibamr.github.io`.

[90] Boyce E Griffith, Richard D Hornung, David M McQueen, and Charles S Peskin. An adaptive, formally second order accurate version of the immersed boundary method. *Journal of Computational Physics*, 223(1):10–49, April 2007.

[91] Boyce E Griffith. An accurate and efficient method for the incompressible Navier–Stokes equations using the projection method as a preconditioner. *Journal of Computational Physics*, 228(20):7565–7595, November 2009.

[92] Boyce E Griffith. On the Volume Conservation of the Immersed Boundary Method. *Communications in Computational Physics*, 12(2):401–432, August 2012.

[93] William J Rider, Jeffrey A Greenough, and James R Kamm. Accurate monotonicity- and extrema-preserving methods through adaptive nonlinear hybridizations. *Journal of Computational Physics*, 225(2):1827–1848, August 2007.

[94] Phillip Colella and Paul R Woodward. The Piecewise Parabolic Method (PPM) for gas-dynamical simulations. *Journal of Computational Physics*, 54(1):174–201, April 1984.

[95] Boyce E. Griffith, Xiaoyu Luo, David M. Mcqueen, and Charles S. Peskin. Simulating the fluid dynamics of natural and prosthetic heart valves using the immersed boundary method. *International Journal of Applied Mechanics*, 01(01):137–177, 2009.

[96] Nishant Nangia, Boyce E. Griffith, Neelesh A. Patankar, and Amneet Pal Singh Bhalla. A robust incompressible navier-stokes solver for high density ratio multiphase flows. *Journal of Computational Physics*, 390:548–594, 2019.

[97] Panagiotis Dafnakis, Amneet Pal Singh Bhalla, Sergej Antonello Sirigu, Mauro Bonfanti, Giovanni Bracco, and Giuliana Mattiazzo. Comparison of wave–structure interaction dynamics of a submerged cylindrical point absorber with three degrees of freedom using potential flow and computational fluid dynamics models. *Physics of Fluids*, 32(9):093307, 2020.

[98] Kunihiko Taira and Tim Colonius. The immersed boundary method: A projection approach. *Journal of Computational Physics*, 225(2):2118–2137, August 2007.

[99] J. Blair Perot. An analysis of the fractional step method. *Journal of Computational Physics*, 108(1):51–58, 1993.

[100] J. L. Guermond and L. Quartapelle. On stability and convergence of projection methods based on pressure poisson equation. *International Journal for Numerical Methods in Fluids*, 26(9):1039–1053, 1998.

[101] Ramon Codina. Pressure stability in fractional step finite element methods for incompressible flows. *Journal of Computational Physics*, 170(1):112–140, 2001.

[102] SAMRAI: Structured Adaptive Mesh Refinement Application Infrastructure. `http://www.llnl.gov/CASC/SAMRAI`.

[103] Mustapha Chaker, Cyrus B Meher-Homji, and Thomas Mee. Inlet Fogging of Gas Turbine Engines—Part III: Fog Behavior in Inlet Ducts, Computational Fluid Dynamics Analysis, and Wind Tunnel Experiments. *Journal of Engineering for Gas Turbines and Power*, 126(3):571–580, July 2004.

[104] Arunava Ghosh, R C Boucher, and Robert Tarran. Airway hydration and COPD. *Cellular and Molecular Life Sciences*, 72(19):3637–3652, June 2015.

[105] Hanliang Guo and Eva Kanso. Mucociliary Transport in Healthy and Diseased Environments. May 2016.

[106] Mark Mitchell, Baurzhan Muftakhidinov, and Tobias Winchen. Engauge digitizer software.

[107] Sarah D Olson and Lisa J Fauci. Hydrodynamic interactions of sheets vs filaments: Synchronization, attraction, and alignment. *Physics of Fluids*, 27(12):121901, December 2015.

[108] Patrick R Sears, Kristin Thompson, Michael R Knowles, and C William Davis. Human airway ciliary dynamics. *American Journal of Physiology - Lung Cellular and Molecular Physiology*, 304(3):L170–L183, February 2013.

[109] Yang Ding, Janna C Nawroth, Margaret J McFall-Ngai, and Eva Kanso. Mixing and transport by ciliary carpets: a numerical study. *Journal of Fluid Mechanics*, 743: 124–140–140, 2014.

[110] Sylvain Chateau, Umberto D'Ortona, Sébastien Poncet, and Julien Favier. Transport and mixing induced by beating cilia in human airways. *Frontiers in Physiology*, 9:161, 2018.

[111] Matthias Mandø and Lasse Rosendahl. On the motion of non-spherical particles at high reynolds number. *Powder Technology*, 202(1):1–13, 2010.

[112] Peter F. DeCarlo, Jay G. Slowik, Douglas R. Worsnop, Paul Davidovits, and Jose L. Jimenez. Particle morphology and density characterization by combined mobility and aerodynamic diameter measurements. part 1: Theory. *Aerosol Science and Technology*, 38(12):1185–1205, 01 2004.

[113] Maziar Gholami Korzani, Sergio A. Galindo-Torres, Alexander Scheuermann, and David J. Williams. Parametric study on smoothed particle hydrodynamics for accurate determination of drag coefficient for a circular cylinder. *Water Science and Engineering*, 10(2):143–153, 2017.

[114] Arzhang Khalili and Bo Liu. Stokes'paradox: creeping flow past a two-dimensional cylinder in an infinite domain. 817:374–387, 2017.

[115] Nishant Nangia, Hans Johansen, Neelesh A. Patankar, and Amneet Pal Singh Bhalla. A moving control volume approach to computing hydrodynamic forces and torques on immersed bodies. *Journal of Computational Physics*, 347:437–462, 2017.

[116] Nikolai Albertowich Fuchs, R. E. Daisley, and Marina Fuchs. *The Mechanics of Aerosols. Translated from Russian Edition (Moscow).* 1964.

[117] Kambez Hajipouran Benam, Richard Novak, Remi Villenave, Carolina Lucchesi, Cedric Hubeau, Janna Nawroth, Mariko Hirano-Kobayashi, Thomas C Ferrante, Youngjae Choe, Rachelle Prantil-Baun, James C Weaver, Geraldine A Hamilton, Anthony Bahinski, and Donald E Ingber. Human small airway-on-a-chip: A novel microphysiological system to model lung inflammation, accelerate drug development and enable inhalational toxico-analysis. *Eur Respir J*, 48(suppl 60):OA4542, September 2016.

[118] Guillermina R. Ramirez-San Juan, Arnold J. T. M. Mathijssen, Mu He, Lily Jan, Wallace Marshall, and Manu Prakash. Multi-scale spatial heterogeneity enhances particle clearance in airway ciliary arrays. *Nature Physics*, 16(9):958–964, 2020.

[119] Hassan Aref. Stirring by chaotic advection. *Journal of Fluid Mechanics*, 143:1–21, 1984.

[120] J M Ottino. Mixing, chaotic advection, and turbulence. *Annual Review of Fluid Mechanics*, 22(1):207–254, 1990.

[121] Hassan Aref, John R. Blake, Marko Budišić, Silvana S. S. Cardoso, Julyan H. E. Cartwright, Herman J. H. Clercx, Kamal El Omari, Ulrike Feudel, Ramin Golestanian, Emmanuelle Gouillart, GertJan F. van Heijst, Tatyana S. Krasnopolskaya, Yves Le Guer, Robert S. MacKay, Vyacheslav V. Meleshko, Guy Metcalfe, Igor Mezić, Alessandro P. S. de Moura, Oreste Piro, Michel F. M. Speetjens, Rob Sturman, Jean-Luc Thiffeault, and Idan Tuval. Frontiers of chaotic advection. *Rev. Mod. Phys.*, 89: 025007, Jun 2017.

[122] Han E.H. Meijer, Mrityunjay K. Singh, and Patrick D. Anderson. On the performance of static mixers: A quantitative comparison. *Progress in Polymer Science*, 37(10): 1333–1349, 2012. ISSN 0079-6700. Topical Issue on Polymer Physics.

[123] Guy Metcalfe and Daniel Lester. Mixing and heat transfer of highly viscous food products with a continuous chaotic duct flow. *Journal of Food Engineering*, 95(1): 21–29, 2009. ISSN 0260-8774.

[124] Z. B. Stone and H. A. Stone. Imaging and quantifying mixing in a model droplet micromixer. *Physics of Fluids*, 17(6):063103, 2005.

[125] George Mathew, Igor Mezić, and Linda Petzold. A multiscale measure for mixing. *Physica D: Nonlinear Phenomena*, 211(1):23–46, 2005.

[126] Jean-Luc Thiffeault. Using multiscale norms to quantify mixing and transport. 25(2): R1–R44, 2012.

[127] G. Haller and G. Yuan. Lagrangian coherent structures and mixing in two-dimensional turbulence. *Physica D: Nonlinear Phenomena*, 147(3):352–370, 2000.

[128] George Haller. Lagrangian coherent structures. *Annual Review of Fluid Mechanics*, 47 (1):137–162, 2015.

[129] Shawn C. Shadden, Francois Lekien, and Jerrold E. Marsden. Definition and properties of lagrangian coherent structures from finite-time lyapunov exponents in two-dimensional aperiodic flows. *Physica D: Nonlinear Phenomena*, 212(3):271–304, 2005.

[130] George Haller. A variational theory of hyperbolic lagrangian coherent structures. *Physica D: Nonlinear Phenomena*, 240(7):574–598, 2011. ISSN 0167-2789.

[131] George Haller and Francisco J. Beron-Vera. Geodesic theory of transport barriers in two-dimensional flows. *Physica D: Nonlinear Phenomena*, 241(20):1680–1702, 2012.

[132] Janna C Nawroth, Hanliang Guo, Eric Koch, Elizabeth A C Heath-Heckman, John C Hermanson, Edward G Ruby, John O Dabiri, Eva Kanso, and Margaret McFall-Ngai. Motile cilia create fluid-mechanical microhabitats for the active recruitment of the host microbiome. *Proceedings of the National Academy of Sciences*, 114(36):9510–9516, September 2017.